NAVAL POSTGRADUATE SCHOOL

MONTEREY, CALIFORNIA

DISSERTATION

IMPROVED UUV POSITIONING USING ACOUSTIC COMMUNICATIONS AND A POTENTIAL FOR REAL-TIME NETWORKING AND COLLABORATION

by

Renato Peres Vio

June 2017

Dissertation Supervisors: Roberto Cristi and Kevin B. Smith

THIS PAGE INTENTIONALLY LEFT BLANK

REPORT DOCUMENTATION PAGE		*Form Approved OMB No. 0704–0188*

Public reporting burden for this collection of information is estimated to average 1 hour per response, including the time for reviewing instruction, searching existing data sources, gathering and maintaining the data needed, and completing and reviewing the collection of information. Send comments regarding this burden estimate or any other aspect of this collection of information, including suggestions for reducing this burden, to Washington headquarters Services, Directorate for Information Operations and Reports, 1215 Jefferson Davis Highway, Suite 1204, Arlington, VA 22202-4302, and to the Office of Management and Budget, Paperwork Reduction Project (0704-0188) Washington, DC 20503.

1. AGENCY USE ONLY (*Leave blank*)	2. REPORT DATE June 2017	3. REPORT TYPE AND DATES COVERED Dissertation	
4. TITLE AND SUBTITLE IMPROVED UUV POSITIONING USING ACOUSTIC COMMUNICATIONS AND A POTENTIAL FOR REAL-TIME NETWORKING AND COLLABORATION		**5. FUNDING NUMBERS**	
6. AUTHOR(S) Renato Peres Vio			
7. PERFORMING ORGANIZATION NAME(S) AND ADDRESS(ES) Naval Postgraduate School Monterey, CA 93943-5000		**8. PERFORMING ORGANIZATION REPORT NUMBER**	
9. SPONSORING /MONITORING AGENCY NAME(S) AND ADDRESS(ES) N/A		**10. SPONSORING / MONITORING AGENCY REPORT NUMBER**	

11. SUPPLEMENTARY NOTES The views expressed in this thesis are those of the author and do not reflect the official policy or position of the Department of Defense or the U.S. Government. IRB number _____N/A_____.

12a. DISTRIBUTION / AVAILABILITY STATEMENT Approved for public release. Distribution is unlimited.	12b. DISTRIBUTION CODE

13. ABSTRACT (maximum 200 words)

Due to the lack of underwater navigation aids, a system capable of helping a submersible vehicle maintain position accuracy, permitting it to stay underwater for longer periods, is extremely desirable. The accuracy and reliability of the state-of-the-art techniques are compromised in multipath environments. In this dissertation, environments where multipath represents a problem are explored. A more accurate estimate for underwater distances by using acoustic modems and an acoustic ray tracing code to model the environment is proposed for real-time applications.

To be able to establish the submersible vehicle's position, a tracking algorithm relying on Kalman filtering (KF) techniques was developed to fuse all available data. The lack of directional information from the acoustic modems employed produced nonlinearities that were treated using the extended Kalman filter (EKF) and the unscented Kalman filter (UKF).

The developed algorithms were initially tested using synthetic data, and the results showed the importance of a smoothing algorithm to produce realistic trajectories. This analysis also suggested that faster convergence and better behavior in the presence of noise was achieved by the UKF approach. Real data collected during sea trials confirmed the robustness of the UKF which, despite few and inconsistent measurements, was able to provide reliable submersible vehicle positioning. Better tracking results were also achieved when underwater distances were estimated by modelling the environment.

14. SUBJECT TERMS underwater navigation systems, acoustic modems, extended and unscented Kalman filter, acoustic ray tracing			**15. NUMBER OF PAGES** 185
			16. PRICE CODE
17. SECURITY CLASSIFICATION OF REPORT Unclassified	**18. SECURITY CLASSIFICATION OF THIS PAGE** Unclassified	**19. SECURITY CLASSIFICATION OF ABSTRACT** Unclassified	**20. LIMITATION OF ABSTRACT** UU

NSN 7540–01-280-5500

Standard Form 298 (Rev. 2–89) Prescribed by ANSI Std. 239–18

THIS PAGE INTENTIONALLY LEFT BLANK

**IMPROVED UUV POSITIONING USING ACOUSTIC COMMUNICATIONS
AND A POTENTIAL FOR REAL-TIME NETWORKING AND
COLLABORATION**

Renato Peres Vio
Lieutenant Commander, Brazilian Navy
B.S., Universidade Estadual Paulista, 2000
M.Sc., Universidade de São Paulo, 2005

Submitted in partial fulfillment of the
requirements for the degree of

DOCTOR OF PHILOSOPHY IN ENGINEERING ACOUSTICS

from the

**NAVAL POSTGRADUATE SCHOOL
June 2017**

Approved by: Roberto Cristi   Lawrence J. Ziomek
                Professor of Electrical and   Professor of Electrical and
                Computer Engineering   Computer Engineering
                Dissertation Supervisor

                                                     Daphne Kapolka
                Kevin B. Smith   Senior Lecturer
                Professor of Physics   Department of Physics
                Dissertation Supervisor

                                                     Douglas P. Horner
                                                     Professor of Mechanical and
                                                     Aerospace Engineering

Approved by: Kevin B. Smith, Chair, Department of Physics

                R. Clark Robertson, Chair, Department of Electrical and Computer Engineering

                Douglas Moses, Vice Provost of Academic Affairs

iii

THIS PAGE INTENTIONALLY LEFT BLANK

ABSTRACT

Due to the lack of underwater navigation aids, a system capable of helping a submersible vehicle maintain position accuracy, permitting it to stay underwater for longer periods, is extremely desirable. The accuracy and reliability of the state-of-the-art techniques are compromised in multipath environments. In this dissertation, environments where multipath represents a problem are explored. A more accurate estimate for underwater distances by using acoustic modems and an acoustic ray tracing code to model the environment is proposed for real-time applications.

To be able to establish the submersible vehicle's position, a tracking algorithm relying on Kalman filtering (KF) techniques was developed to fuse all available data. The lack of directional information from the acoustic modems employed produced nonlinearities that were treated using the extended Kalman filter (EKF) and the unscented Kalman filter (UKF).

The developed algorithms were initially tested using synthetic data, and the results showed the importance of a smoothing algorithm to produce realistic trajectories. This analysis also suggested that faster convergence and better behavior in the presence of noise was achieved by the UKF approach. Real data collected during sea trials confirmed the robustness of the UKF which, despite few and inconsistent measurements, was able to provide reliable submersible vehicle positioning. Better tracking results were also achieved when underwater distances were estimated by modelling the environment.

THIS PAGE INTENTIONALLY LEFT BLANK

TABLE OF CONTENTS

LIST OF FIGURES

xi

LIST OF TABLES

THIS PAGE INTENTIONALLY LEFT BLANK

LIST OF ACRONYMS AND ABBREVIATIONS

CSC	consensus sea current
CW	continuous wave
DSP	digital signal processor
EKF	extended Kalman filter
GIB	GPS intelligent buoy
GPS	global positioning system
HFM	hyperbolic frequency modulated
INS	inertial navigation system
IR	impulse response
KF	Kalman filter
LBL	long baseline
LFM	linear frequency modulated
MFSK	multiple frequency shift keying
SBL	short baseline
SNR	signal-to-noise ratio
TB	time bandwidth
TL	transmission loss
UHF	ultrahigh frequency
UKF	unscented Kalman filter
USBL	ultra-short baseline
USV	unmanned surface vehicle
UT	unscented transform
UUV	unmanned underwater vehicle
WG	wave glider

THIS PAGE INTENTIONALLY LEFT BLANK

ACKNOWLEDGMENTS

THIS PAGE INTENTIONALLY LEFT BLANK

I.   INTRODUCTION

Parts of this chapter were previously published by IEEE [1].*

There are several definitions for navigation. One of our favorites, which was translated into English, states that "navigation is the science and art of safely guiding a vehicle from the starting point until the final destination" [2]. The simplest approach to navigating at sea is based on dead reckoning, by which the current vehicle's position is estimated by integrating velocity between periodic fixes, such as a global positioning system (GPS) or similar. The inaccuracies inherent in this process can quickly multiply, however, to become significant errors.

Advances in navigational aids, in particular satellite navigation, have made course selection through the dead reckoning of human mariners obsolete for most purposes; although the prudent sea navigator still uses dead reckoning as a backup tool in case of failure of the more advanced systems.

In some systems, human dead reckoning has been replaced with automatic (without human intervention) navigational information gathered from inertial sensors (gyroscopes and accelerometers); such systems are known as inertial navigation systems (INS). There are also hybrid systems that make use of a digital magnetic compass and a fusion of different sensors, or only estimates, to supply the data necessary for navigation.

In dead reckoning systems, including the INS, errors due to sensors' bias and misalignment accumulate over time and can lead to unacceptable position errors. Therefore, it is necessary to receive, regularly, precise position updates from external reliable sources, like GPS, to keep the position errors at acceptable levels.

The most advanced INS for underwater navigation have a margin of error ranging from 0.1% to 1% of the distance travelled, without relying on external positioning sources. This is usually represented by what is called the circular error probability, a circle which is bounded by 50% probability of containing the true position [3]. From the experiments conducted during this work, it was found that systems relying only on digital magnetic compasses and speed estimates may produce errors of around 20% of circular error probability or even higher.

Successful surface navigation systems have been developed that integrate GPS with inertial sensors, but the absence of GPS signal reception underwater makes navigation for manned and unmanned underwater vehicles (UUV) a more difficult task. By surfacing, the UUV can get a position update using its GPS, but this is impossible (e.g., under ice) or undesirable in many circumstances [4]. In military applications, surfacing can increase the chance of detection or represent a delay in the mission that is unacceptable. Therefore, a technique to accurately update the position of an autonomous system while underwater is extremely desirable.

Different approaches to establish an underwater positioning system have been proposed over the years. They include short baseline (SBL), long baseline (LBL), ultra-short baseline (USBL), GPS intelligent buoys (GIB), and some hybrid systems based on the previous ideas [5], [6], and [7]. All of those systems make use of acoustic travel time measurements to estimate the distance and, in some systems, the bearing from the underwater vehicle to reference points located on the surface or the sea floor. Those systems are reliable when the depth being explored is on the order of, or larger than, the horizontal distances between the assets.

Estimation of horizontal distances in relatively shallow water is more complex, due mainly to the multipath nature of the propagation, wherein multiple arrivals reach the receiver at different times by different propagation paths. Accurately estimating the travel time—and, consequently, the distance—of these acoustic signals under such variable conditions is difficult. Some of the systems described previously are able to account for

the refraction of the sound waves when the sound speed profile is available, but none of them provides a solution to treat the distance estimation errors caused by multipath signals.

In this dissertation, the relatively shallow water environments wherein accurately estimating multipath signals represents a navigational problem are explored. A more accurate estimation for the distance, based on acoustic wave travel time measurements, an acoustic ray tracing code to model the environment, and an iterative routine to match the measurements with synthetic predictions, is proposed. The algorithm is designed to take only a few seconds to converge to a solution, making it appropriate for real-time applications [1].

To obtain a reliable estimate of the vehicle position, the information for a number of sources and mathematical models must be combined so effects due to multipath, sea currents, and simple observation noise can be mitigated. The ability to establish the UUV position via a tracking algorithm relying on Kalman filtering (KF) techniques is developed to fuse all available information (Chapters II and V).

The development of the tracking algorithm takes into account the characteristics of the measurement system. This research relies on battery-powered digital signal processor (DSP)-based acoustic modems, which make use of acoustic communication protocols to measure the acoustic wave travel time from the UUV to the reference points. The main characteristics of our acoustic modems are:

1.   Inability to take simultaneous measurements from different reference points, and

2.   No bearing (direction) is associated to the travel times measured from systems used in this work (though such systems are available for future studies).

Those characteristics produce a non-linear measurement equation that is treated using two different approaches: a Taylor series linearization as in the extended Kalman filter (EKF), and a statistical linearization based on what are called "sigma points," as in the unscented Kalman filter (UKF). Additionally, practical aspects such as smoothing and tuning are addressed.

3

As part of the UUV tracking model, the drift caused by the sea current was modeled as a random walk and is part of the state of the system. Predictions for the sea current from different UUVs may be transmitted, via the reference point at the surface, to a command ship or shore-based command center for further processing. In Chapter V, Section G, a consensus algorithm is presented to take advantage of this information.

The developed algorithms are tested initially using synthetic data (Chapter VI), and then again using real data collected during the sea trials that took place in Monterey Bay in August 2015 (Chapter VII).

This dissertation is constructed as follows. After this Introduction chapter, a statement of the problem and a model for the UUV are presented in Chapter II. Important aspects of travel time estimation are explored in Chapter III, and a technique to estimate distance based on travel time measurements, employing a ray tracing code, is presented in Chapter IV. Two tracking algorithms based on the EKF and UKF are featured in Chapter V, and simulations of the developed algorithms are discussed in Chapter VI. Results of the sea trials are provided in Chapter VII. A conclusion and recommendations for future work are given in Chapter VIII.

II. PROBLEM STATEMENT AND UUV MODEL

As was described in the previous chapter, underwater navigation is particularly challenging due to the fact that a number of navigation aids, such as GPS, are not available underwater. In view of this, to accurately estimate a UUV's position at any time during a mission, one may rely on acoustic communication between the UUV and other platforms at known locations. As addressed in later chapters, a combination of acoustic modems with or without advanced features, such as directional sensitivity, and multiple surface vehicles may provide the required tracking.

In a typical mission, a UUV is part of a network that may consist of surface platforms at known locations commonly provided by a GPS, bottom deployed modems (at known locations), and possibly other UUVs. The surface and bottom deployed assets, ultimately, represent reference points from which a UUV, using its acoustic modem, can estimate its distance and receive their coordinates (latitude, longitude, and depth), as shown in Figure 1.

Due to the limited bandwidth of the underwater channel, the typical acoustic modem is able to communicate with only one platform at a time. Thus, it is not possible to take measurements of the distance between the UUV and two or more reference points at the same time. Additionally, we are assuming that no bearing associated with the distance measurement is available.
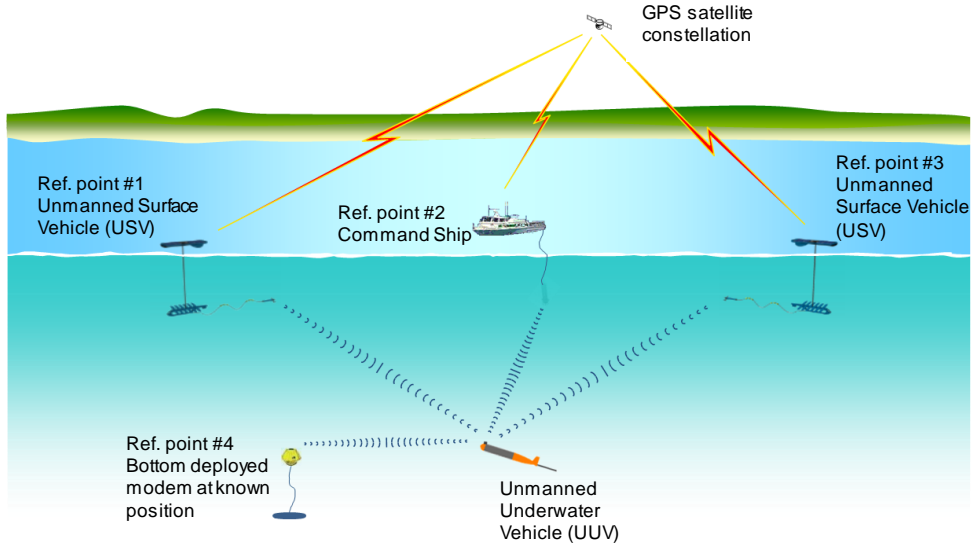
Figure 1.   Network of Reference Points

The main objective of this dissertation is to improve the positioning accuracy of the UUV using this network of reference points. The goal is to provide sufficient tracking accuracy so that the UUV can stay submerged for longer missions while still maintaining accurate track of its position.

The approach to solve this problem is to design an algorithm that combines all information available, which are the travel time measurements, the acoustic wave propagation model, the UUV navigation data in terms of its attitude in the water column (heading, pitch, depth, and speed), and the dynamic model of the UUV motion. All this information can be combined using KF techniques, in particular EKF and UKF, due to the presence of nonlinearities and non-Gaussian disturbances. The problem of modeling is based on the state space representation for dynamic systems as can be seen in the next sections.

A.   STATE SPACE REPRESENTATION OF DYNAMIC SYSTEMS

A fundamental concept to describe the behavior of a dynamic system is the state of the system. The concept of state refers to a minimum set of variables (state variables) that fully describe the system and its response to any given set of inputs while accounting

for errors due to sensor noise and model uncertainties. The set of all possible values of the state variables is the state space.

The state space representation of a dynamic system is not unique and usually involves a time variable t and three sets of variables:

- State variables: $x_1, x_2, \ldots, x_n$
- Input variables: $u_1, u_2, \ldots, u_m$
- Output variables: $z_1, z_2, \ldots, z_p$.

For a continuous-time system, the description generally takes the form, in vector notation, of [8]

$$\dot{\mathbf{x}}(t) = \mathbf{f}(\mathbf{x},\mathbf{u},t) \tag{2.1}$$

$$\mathbf{z}(t) = \mathbf{h}(\mathbf{x},\mathbf{u},t), \tag{2.2}$$

where $\mathbf{f}(\mathbf{x},\mathbf{u},t)$ and $\mathbf{h}(\mathbf{x},\mathbf{u},t)$ are vector functions with n and p components, respectively.

Equation (2.1) is called the state equation, and Equation (2.2) is called the output or measurement equation. If additive noise is present in the state and measurement equations, we have what is called a continuous-time non-linear stochastic dynamic system, and Equations (2.1) and (2.2) become

$$\dot{\mathbf{x}}(t) = \mathbf{f}(\mathbf{x},\mathbf{u},t) + \upsilon(t) \tag{2.3}$$

$$\mathbf{z}(t) = \mathbf{h}(\mathbf{x},\mathbf{u},t) + \omega(t), \tag{2.4}$$

where $\upsilon(t)$ is a n-dimensional vector representing the input disturbance or process noise, which is also called plant noise, and $\omega(t)$ is a p-dimensional vector representing the output disturbance or measurement noise.

If the system and measurements are linear, Equations (2.3) and (2.4) may be written in matrix notation as

$$\begin{bmatrix} \dot{x}_1 \\ \dot{x}_2 \\ \vdots \\ \dot{x}_n \end{bmatrix} = \begin{bmatrix} a_{11} & a_{12} & \cdots & a_{1n} \\ a_{21} & a_{22} & \cdots & a_{2n} \\ \vdots & & & \vdots \\ a_{n1} & a_{n2} & \cdots & a_{nn} \end{bmatrix} \begin{bmatrix} x_1 \\ x_2 \\ \vdots \\ x_n \end{bmatrix} + \begin{bmatrix} b_{11} & b_{12} & \cdots & b_{1m} \\ b_{21} & b_{22} & \cdots & b_{2m} \\ \vdots & & & \vdots \\ b_{n1} & b_{n2} & \cdots & b_{nm} \end{bmatrix} \begin{bmatrix} u_1 \\ u_2 \\ \vdots \\ u_m \end{bmatrix} \tag{2.5}$$

and

$$\begin{bmatrix} z_1 \\ z_2 \\ \vdots \\ z_p \end{bmatrix} = \begin{bmatrix} h_{11} & h_{12} & \cdots & h_{1n} \\ h_{21} & h_{22} & \cdots & h_{2n} \\ \vdots & & & \vdots \\ h_{p1} & h_{p2} & \cdots & h_{pn} \end{bmatrix} \begin{bmatrix} x_1 \\ x_2 \\ \vdots \\ x_n \end{bmatrix} + \begin{bmatrix} d_{11} & d_{12} & \cdots & d_{1m} \\ d_{21} & d_{22} & \cdots & d_{2m} \\ \vdots & & & \vdots \\ d_{p1} & d_{p2} & \cdots & d_{pm} \end{bmatrix} \begin{bmatrix} u_1 \\ u_2 \\ \vdots \\ u_m \end{bmatrix}. \tag{2.6}$$

In vector notation this becomes

$$\dot{\mathbf{x}}(t) = \mathbf{A}(t)\mathbf{x}(t) + \mathbf{B}(t)\mathbf{u}(t) \tag{2.7}$$

$$\mathbf{z}(t) = \mathbf{H}(t)\mathbf{x}(t) + \mathbf{D}(t)\mathbf{u}(t). \tag{2.8}$$

If additive noise is present in the state and measurement equations we have what is called a continuous-time linear stochastic dynamic system, and Equations (2.7) and (2.8) become

$$\dot{\mathbf{x}}(t) = \mathbf{A}(t)\mathbf{x}(t) + \mathbf{B}(t)\mathbf{u}(t) + \upsilon(t) \tag{2.9}$$

$$\mathbf{z}(t) = \mathbf{H}(t)\mathbf{x}(t) + \mathbf{D}(t)\mathbf{u}(t) + \omega(t). \tag{2.10}$$

For discrete-time stochastic non-linear dynamic systems, the state and measurement equations can usually be represented by first order difference equations, and take the form [8]

$$\mathbf{x}(k+1) = \mathbf{f}[\mathbf{x}(k)] + \mathbf{g}[\mathbf{u}(k)] + \upsilon(k) \tag{2.11}$$

$$\mathbf{z}(k) = \mathbf{h}[\mathbf{x}(k)] + \omega(k), \tag{2.12}$$

where the indices k and $k+1$ refer to sampling times $t_k = k\Delta t$ and $t_{k+1} = (k+1)\Delta t$, respectively.

Finally, for discrete-time stochastic linear dynamic systems, the state and measurement equations usually take the form [8]

$$\mathbf{x}(k+1) = \mathbf{F}(k)\mathbf{x}(k) + \mathbf{G}(k)\mathbf{u}(k) + \upsilon(k) \tag{2.13}$$

$$\mathbf{z}(k) = \mathbf{H}(k)\mathbf{x}(k) + \mathbf{D}(k)\mathbf{u}(k) + \omega(k). \tag{2.14}$$

B.   UUV STATE SPACE REPRESENTATION

In this section, a UUV state space representation is presented, considering its dynamics and the characteristics of the range measurement system.

1.   The State Equation

Assuming a UUV moving through the water at depth d moving with speed V, we can build a coordinate system where latitude and longitude are mapped to Cartesian

coordinates (x and y). In this case, θ represents the heading, ϕ represents the pitch, and d (z axis) represents the depth of the UUV (see Figure 2).
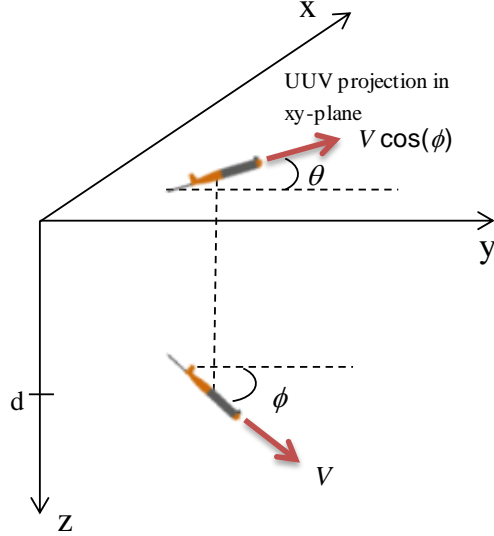
The y axis points to east and the x axis points to north.

Figure 2.   UUV Coordinate System

The motion of the UUV in the *xy*-plane can be represented by the following set of first order differential equations

$$\dot{x}(t) = V(t)\cos(\phi(t))\sin(\theta(t)) + c_x(t) \tag{2.15}$$
$$\dot{y}(t) = V(t)\cos(\phi(t))\cos(\theta(t)) + c_y(t), \tag{2.16}$$

where c_x and c_y represent the speed of the sea current in the x and y directions, respectively. Since we assume the current to be fairly constant in speed and direction and slowly varying in time and location, we have chosen to model it as a random walk [9]. Although it is assumed to be unknown a priori, any prior information, can be easily incorporated in the proposed algorithm.

When d, V, θ, and ϕ are known, the dynamic model in its simplest form becomes

$$\begin{bmatrix} \dot{x}(t) \\ \dot{y}(t) \\ \dot{c}_x(t) \\ \dot{c}_y(t) \end{bmatrix} = \underbrace{\begin{bmatrix} 0 & 0 & 1 & 0 \\ 0 & 0 & 0 & 1 \\ 0 & 0 & 0 & 0 \\ 0 & 0 & 0 & 0 \end{bmatrix}}_{\mathbf{A}} \underbrace{\begin{bmatrix} x(t) \\ y(t) \\ c_x(t) \\ c_y(t) \end{bmatrix}}_{\mathbf{x}(t)} + \underbrace{\begin{bmatrix} 1 & 0 \\ 0 & 1 \\ 0 & 0 \\ 0 & 0 \end{bmatrix}}_{\mathbf{B}} \underbrace{V(t)\cos(\phi(t)) \begin{bmatrix} \sin(\theta(t)) \\ \cos(\theta(t)) \end{bmatrix}}_{\mathbf{u}(t)} . \tag{2.17}$$

In vector notation, Equation (2.17) becomes

$$\dot{\mathbf{x}}(t) = \mathbf{A}\mathbf{x}(t) + \mathbf{B}\mathbf{u}(t). \tag{2.18}$$

As we are only interested in knowing the state of the system at a discrete set of times (sampling times), Equation (2.18) is discretized by the following procedure.

Performing a first order Taylor series expansion yields

$$\mathbf{x}(t + \Delta t) = \mathbf{x}(t) + \dot{\mathbf{x}}(t)\Delta t ; \tag{2.19}$$

substituting (2.18) into (2.19) produces

$$\mathbf{x}(t + \Delta t) = \mathbf{x}(t) + \mathbf{A}\Delta t\mathbf{x}(t) + \mathbf{B}\Delta t\mathbf{u}(t), \tag{2.20}$$

and rearranging Equation (2.20) results in

$$\mathbf{x}(t + \Delta t) = \underbrace{(\mathbf{I} + \mathbf{A}\Delta t)}_{\mathbf{F}}\mathbf{x}(t) + \underbrace{\mathbf{B}\Delta t}_{\mathbf{G}}\mathbf{u}(t). \tag{2.21}$$

Adding noise, we may write the state equation for the stochastic discrete-time linear dynamic system as

$$\mathbf{x}(k+1) = \mathbf{F}(k)\mathbf{x}(k) + \mathbf{G}(k)\mathbf{u}(k) + \upsilon(k). \tag{2.22}$$

In matrix notation, Equation (2.22) becomes

$$\begin{bmatrix} x(k+1) \\ y(k+1) \\ c_x(k+1) \\ c_y(k+1) \end{bmatrix} = \begin{bmatrix} 1 & 0 & \Delta t(k) & 0 \\ 0 & 1 & 0 & \Delta t(k) \\ 0 & 0 & 1 & 0 \\ 0 & 0 & 0 & 1 \end{bmatrix} \begin{bmatrix} x(k) \\ y(k) \\ c_x(k) \\ c_y(k) \end{bmatrix} + \begin{bmatrix} \Delta t(k) & 0 \\ 0 & \Delta t(k) \\ 0 & 0 \\ 0 & 0 \end{bmatrix} V(k)\cos(\phi(k)) \begin{bmatrix} \sin(\theta(k)) \\ \cos(\theta(k)) \end{bmatrix} + \begin{bmatrix} \upsilon_x(k) \\ \upsilon_y(k) \\ \upsilon_{c_x}(k) \\ \upsilon_{c_y}(k) \end{bmatrix}. \tag{2.23}$$

2. The Measurement Equation

In such a case that the acoustic modem does not provide bearing information, we have a range-only measurement, where each successful measurement represents, in the *xy*-plane, a circle of possible UUV positions (see Figure 3).
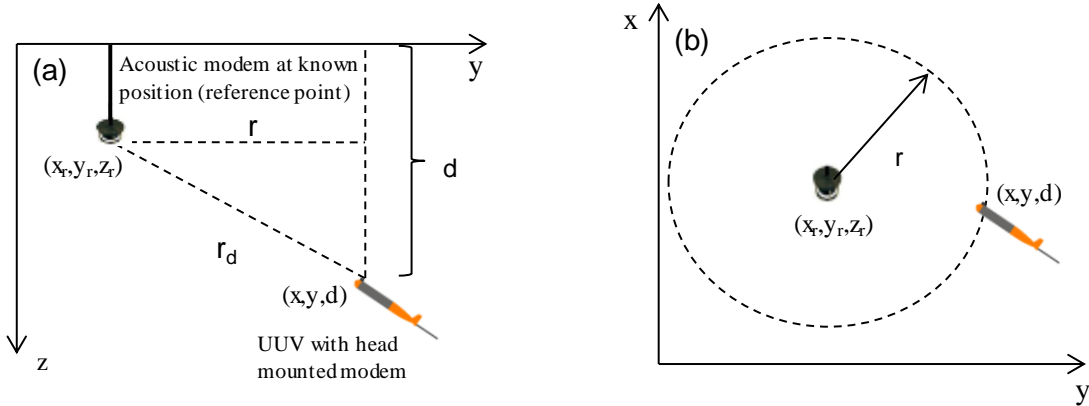
Figure 3.   Measurement Model in (a) *yz*-Plane and in (b) *xy*-Plane

In Figure 3, (x_r, y_r, z_r) are the coordinates of the reference point, (x, y, d) are the coordinates of the UUV, r is the horizontal range, r_d is the slant range, and d is the UUV depth. From Figure 3b, it is noted that

$$(x - x_r)^2 + (y - y_r)^2 = r^2, \qquad (2.24)$$

where $r = \sqrt{r_d^2 - (d - z_r)^2}$ is the distance in the horizontal plane.

Expanding and rearranging Equation (2.24) yields

$$r^2 - x_r^2 - y_r^2 = x^2 - 2xx_r - 2yy_r + y^2. \qquad (2.25)$$

Equation (2.25) may be written as

$$z(k) = h[k, \mathbf{x}(k)], \qquad (2.26)$$

where

- $z(k) = r(k)^2 - x_r(k)^2 - y_r(k)^2$ is the observation, which combines range measurements with knowledge of reference point locations;

- $h[k, \mathbf{x}(k)] = x(k)^2 - 2x(k)x_r(k) - 2y(k)y_r(k) + y(k)^2$ is a non-linear function.

With the addition of noise, the measurement equation takes its final form of

$$z(k) = h[k, \mathbf{x}(k)] + \omega(k). \qquad (2.27)$$

It is important to note that the UUV state space representation is composed of a linear state equation, Equation (2.22), and a non-linear measurement equation, Equation

(2.27). Note, too, that the measurement model needs only the reference point coordinates and horizontal distance to the UUV; this means that the reference point could be a surface asset able to access a GPS, a bottom deployed acoustic modem at a known location, or another UUV with a reliable position.

3. UUV Model

The complete model for the UUV dynamics and measurements (state space representation) is given by

$$\mathbf{x}(k+1) = \mathbf{F}(k)\mathbf{x}(k) + \mathbf{G}(k)\mathbf{u}(k) + \upsilon(k)$$
$$\mathbf{z}(k) = \mathrm{h}\big[k, \mathbf{x}(k)\big] + \omega(k),$$

(2.28)

where

- The state $\mathbf{x}(k)$ is composed of the UUV position and sea current, in the xy-plane, as shown in Equation (2.23);

- The matrices $\mathbf{F}(k)$ and $\mathbf{G}(k)$ are deterministic and known for all k,

$$\mathbf{F}(k) = \begin{bmatrix} 1 & 0 & \Delta t(k) & 0 \\ 0 & 1 & 0 & \Delta t(k) \\ 0 & 0 & 1 & 0 \\ 0 & 0 & 0 & 1 \end{bmatrix}, \quad \mathbf{G}(k) = \begin{bmatrix} \Delta t(k) & 0 \\ 0 & \Delta t(k) \\ 0 & 0 \\ 0 & 0 \end{bmatrix};$$

- The input sequence $\mathbf{u}(k)$ is deterministic and known for all k,

$$\mathbf{u}(k) = V(k)\cos\big(\phi(k)\big) \begin{bmatrix} \sin\big(\theta(k)\big) \\ \cos\big(\theta(k)\big) \end{bmatrix};$$

- $\mathrm{z}(k) = r(k)^2 - x_r(k)^2 - y_r(k)^2$ is the measurement, where $r(k)$ is the horizontal distance from the UUV to the reference point, the parameters $x_r(k)$ and $y_r(k)$ are the coordinates of the reference point (longitude and latitude mapped to Cartesian coordinates);

- $\mathrm{h}\big[k, \mathbf{x}(k)\big] = x(k)^2 - 2x(k)x_r(k) - 2y(k)y_r(k) + y(k)^2$ is a non-linear function;

- The noises $\upsilon(k)$ and $\omega(k)$ are assumed to be zero mean, white (i.e., uncorrelated) Gaussian processes

12

$$E\left[\upsilon(k)\right] = E\left[\omega(k)\right] = 0$$

$$E\left[\upsilon(k)\upsilon(j)^{\mathrm{T}}\right] = \mathbf{Q}_k \delta_{k,j}$$

$$E\left[\omega(k)\omega(j)^{\mathrm{T}}\right] = \mathrm{R}_k \delta_{k,j}$$

$$E\left[\upsilon(k)\omega(j)^{\mathrm{T}}\right] = 0 \; \forall \, k, j \, ,$$

where $\delta_{k,j} = \begin{cases} 1 \ \text{if} \ \ k = j \\ 0 \ \text{if} \ \ k \neq j \end{cases}$. The UUV model, as developed in this section, is the basis of

the tracking algorithm developed in Chapter V.

THIS PAGE INTENTIONALLY LEFT BLANK

III. ACOUSTIC WAVE TRAVEL TIME ESTIMATION

As seen in Chapter II, the measurement of distances underwater, from the UUV to the reference points, is an important part of the problem addressed in this dissertation. In this chapter and in the next, the techniques used to accomplish this task are discussed.

Distance measurement by timing an echo is the standard procedure in radar or active sonar applications. A waveform, with proper time localization characteristics, is transmitted, and the time that it takes to receive the echo of that waveform is measured (two-way travel time) to estimate the distance from source to target. The first problem to be solved is how to estimate the travel time from measurements of an acoustic echo.

A.   CROSS-CORRELATION FUNCTION

It is commonly accepted that the time of arrival of a known pulse can be determined by correlating the transmitted and received pulses [10]. This is robust in the presence of noise and distortion, especially when the disturbances are Gaussian. For two jointly wide-sense stationary random processes, the cross-correlation is defined as an ensemble average:

$$R_{xy}(\tau) = E\left[x(t)\,y^{*}(t+\tau)\right]. \tag{3.1}$$

In practice, we assume joint ergodicity so that it is computed by properly averaging in time. Considering two ergodic processes with finite duration T, the time-average cross-correlation function may be calculated as

$$R_{xy}(\tau) = \frac{1}{T}\int_{-\infty}^{\infty} x(t)\,y^{*}(t+\tau)\,dt. \tag{3.2}$$

Now let us consider that $x(t) = s(t)$ represents the transmitted signal, defined in the interval $[0, T]$, and $y(t)$ represents the received signal (single echo) defined in the interval $[\tau_{A}, \tau_{A}+T]$, where $\tau_{A} > T$.

For a stationary source and target, the received signal may be modeled as being a delayed and attenuated version of the transmitted signal (plus noise), where γ is the

attenuation factor. For simplicity, dispersion and other propagation effects in the received signal are not being considered. Then

$$y(t) = \gamma s(t - \tau_A) + n(t).$$ (3.3)

The goal here is to estimate the received signal's time of arrival τ_A. From Equations (3.2) and (3.3), the time-average cross-correlation function may be written as

$$R_{xy}(\tau) = \frac{1}{T} \int_{-\infty}^{\infty} s(t) \left[\gamma s(t - \tau_A + \tau) + n(t + \tau) \right]^* dt.$$ (3.4)

Considering that signal and noise are uncorrelated and evaluating Equation (3.4) at $\tau = \tau_A$, we obtain

$$R_{xy}(\tau_A) = \gamma \frac{1}{T} \int_{-\infty}^{\infty} |s(t)|^2 \, dt = \gamma P_{avg,s}.$$ (3.5)

Equation (3.5) shows that the time-average cross-correlation function peaks at the time of arrival τ_A and, in this ideal scenario, with a value proportional to the transmitted signal's average power [11]. Therefore, the time when the cross-correlation function peaks is the best estimate for the signal's time of arrival.

This technique is usually applied in slowly varying environments where the characteristics of the signal and noise remain stationary during the finite observation time T [12].

B.   MATCHED FILTER

The cross-correlation between received and transmitted signals may be easily implemented as a matched filter. The matched filter is an optimum filter in the sense that it can maximize the signal-to-noise ratio (SNR) at a designed time instant t_o after the signal's arrival.

The impulse response, $h(t)$, of the matched filter is defined by the waveform to which the filter is matched. Following [13], the impulse response of a filter matched to the signal $s(t)$, for the case of input white noise, is

$$h(t) = K s^*(t_o - t),$$ (3.6)

where K is a constant and t_o is the designed instant at which the filter output will give the maximum SNR. In applications that involve only detecting the arrival time of a signal immersed in noise, the choice for t_o is made only to make the matched filter causal (if necessary); that is, $h(t)$ must be zero for $t < 0$. It implies that the parameter t_o shall be greater than or equal to the duration of the transmitted signal T [14]. If causality is not a concern in the matched filter implementation, t_o can be set to zero, as in the example shown in Figure 4.

For completeness, the frequency response of the matched filter is

$$H(f) = KS^*(f)e^{-j2\pi f t_o}. \tag{3.7}$$

The matched filter output $y(t)$ may be represented by the convolution integral of the received signal (as in Equation (3.3) and the filter impulse response [14]

$$y(t) = \int_{-\infty}^{\infty} \left[\gamma s(u - \tau_A) + n(u) \right] s^*(u - t + t_o) du, \tag{3.8}$$

where K in Equation (3.6) was set to 1. Given that the signal and noise are uncorrelated, Equation (3.8) reduces to

$$y(t) = \int_{-\infty}^{\infty} \gamma s(u - \tau_A) s^*(u - t + t_o) du. \tag{3.9}$$

Equation (3.9) may be recognized as the cross-correlation of the received signal with the transmitted signal lagged by t_o-t. The peak in the matched filter output will occur when $u - \tau_A = u - t + t_o$, which means that $t_{peak} = \tau_A + t_o$ because

$$y(\tau_A + t_o) = \int_{-\infty}^{\infty} \gamma s(u - \tau_A) s^*(u - \tau_A) du = \gamma \int_{-\infty}^{\infty} |s(t)|^2 dt. \tag{3.10}$$

Comparing Equation (3.5) with Equation (3.10) we can see that both give similar results. At this point one may conclude that the matched filter and the cross-correlation function are equivalent ways to estimate a signal's time of arrival.
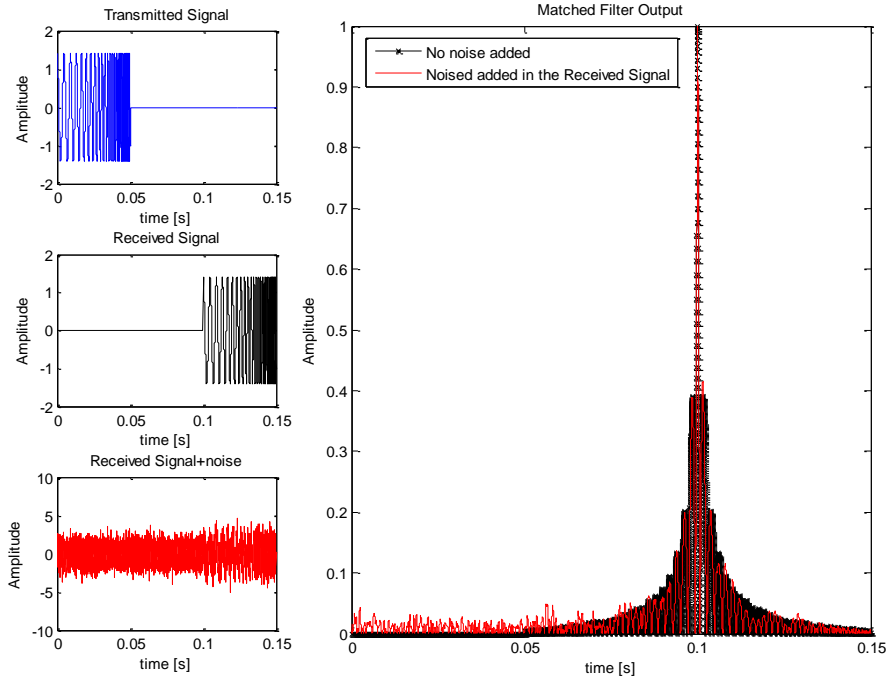
Figure 4.   Matched Filter Used to Detect Signal's Time of Arrival,
Designed with t_o=0

Figure 4 represents the output of a matched filter designed with t_o=0. In this example, a hyperbolic frequency modulated pulse is transmitted (sweeping from 200 to 2200 *Hz*, *T*=50 *ms*, *TB*=100) and a signal immersed in noise, SNR=3dB, is received (left panel, first and third plots). In an ideal no-noise scenario, the received signal arrives at *t*=0.1*s* (left panel, second plot). The matched filter peaks at *t*=0.1*s* for both signals (no noise and signal plus noise), indicating a reception at this time (right panel).

1.   The Doppler Effect

When there is relative motion between source and target, the performance of the matched filter degrades. Referring to Figure 5, consider the simple case when a source in motion at constant velocity is transmitting a continuous wave (CW) pulse during *T* seconds, and receiving an echo from a target in motion. The relative motion causes a shift in the frequency of the received signal. This effect is called the Doppler effect.
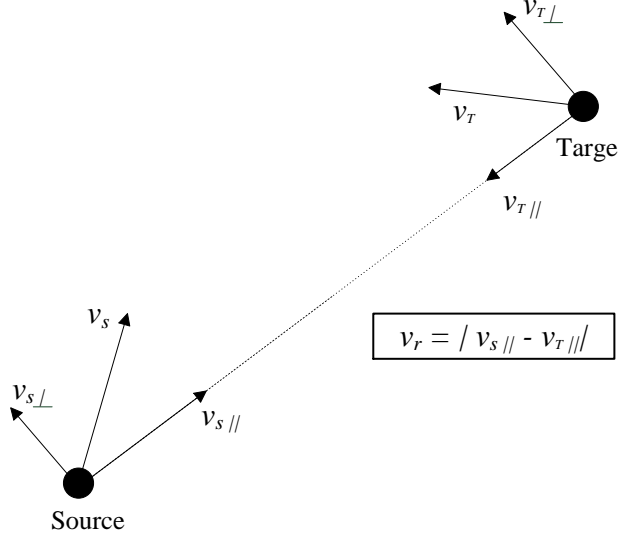
Figure 5.   Relative Radial Speed between Source and Target

Defining the Doppler shift as $f_d = f_c - f_R$ where f_c is the frequency of the transmitted signal, f_R is the frequency of the received signal, and assuming that the propagation speed in the medium (c) is much greather than the relative radial speed between source and target (v_r) yields [15]

$$f_d \approx \pm f_c \frac{2v_r}{c}.$$
(3.11)

This frequency shift may affect the system's ability to detect the incoming signal, which is why it is necessary to take it into account when designing the matched filter. Especially in underwater applications, while the relative motion might be small compared to the medium propagation speed, the carrier frequency (for modulated waveforms) might be sufficiently high so that the frequency shift becomes relevant.

2.   Received Signal Model

To understand the effect of Doppler shift in the received signal, let us consider a target moving with constant radial speed v_r away from a static source. At time t the target will be located at range $r(t)$, given by

$$r(t) = r_o + v_r t,$$
(3.12)

19

where at $t=0$ the target will be located at range r_o. Assuming that the source will start transmitting $x(t)$ at $t=0$, the received signal (echo) at time t is

$$x'(t) = x\left[t - \tau(t)\right]. \tag{3.13}$$

As the target is moving while the signal is being reflected, the two-way travel time $\tau(t)$ in Equation (3.13) is considered a function of time [16]. For simplicity, no attenuation or other propagation effects are being considered.

Assuming that the propagation speed in the medium c is constant, we can calculate $\tau(t)$ as [17]

$$\tau(t) = \frac{2}{c} r\left(t - \frac{\tau(t)}{2}\right). \tag{3.14}$$

Substituting Equation (3.12) into Equation (3.14) yields

$$\tau(t) = \frac{2}{c}\left[r_o + v_r t - \frac{v_r \tau(t)}{2}\right] = \frac{2r_o + 2v_r t}{c + v_r}. \tag{3.15}$$

Then by substituting Equation (3.15) into Equation (3.13), we obtain

$$x'(t) = x\left(t - \frac{2r_o + 2v_r t}{c + v_r}\right) = x\left(\left(1 - \frac{2v_r}{c + v_r}\right)t - \frac{2r_o}{c + v_r}\right). \tag{3.16}$$

From Equation (3.16), the received signal may be written as

$$x'(t) = x(\alpha t - \tau_o), \tag{3.17}$$

where for $c \gg v_r$, $\alpha \approx 1 - \frac{2v_r}{c}$ and $\tau_o \approx \frac{2r_o}{c}$.

As represented in Equation (3.17), the Doppler effect manifests by compressing (or expanding) the received signal, and this is mathematically described by a scale factor (α) in time. Even if the transmitted signal can be considered narrowband, the effect in the received signal is a translation in the frequency of the carrier (Doppler shift) and an increase or decerease in the signal bandwidth.

Due to the frequency mismatch between transmitted and received signals, a filter matched to $x(t)$ will no longer be matched to $x'(t)$ in Equation (3.17). This mismatch may cause a reduction in the peak at the matched filter output, and depending on the

20

severity of the mismatch, this peak can be reduced to levels that do not permit target detection.

If the relative radial speed, v_r, is known or the Doppler shift can be measured, a filter matched to $x'(t)$ may be constructed as

$$h(t) = x[\alpha(t_o - t)]. \qquad (3.18)$$

In cases where the relative radial speed is not known in advance, the classical approach is to have a multi-hypothesis detector, also called a "bank" of matched filters, tuned at different radial speeds (or Doppler shifts), where the filter that gives the highest output is selected (see Figure 6). This process is optimal under restricted circumstances, computationally intense, and time consuming.
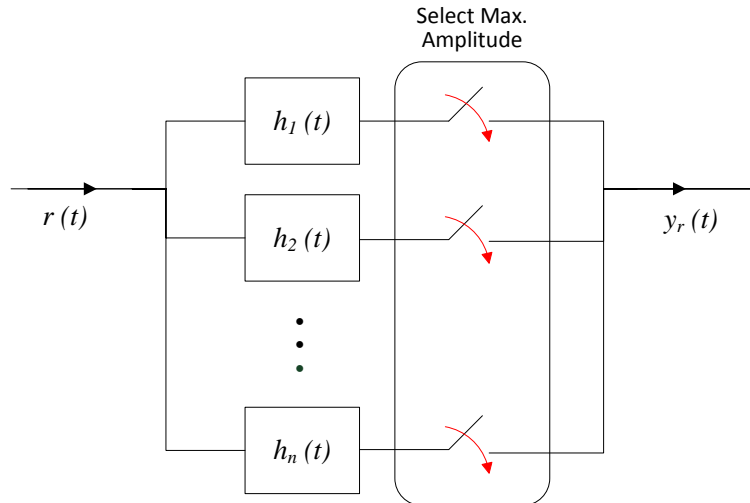
Figure 6.　Multi-hypothesis Detector or "Bank" of Matched Filters

The use of such detectors can introduce serious limitations in some real-time underwater acoustics applications that take advantage of physically small, battery powered DSP-based modems [18]. In these applications, the use of a signal with a certain tolerance for the Doppler effect is desirable to avoid the use of complicated and time consuming detectors.

C.   COMMON WAVEFORMS IN UNDERWATER ACOUSTICS

The selection of the waveform is a complex and important task, playing an important role in the overall performance of distance measurements of systems underwater. The most common waveforms used for this task are the linear frequency modulated (LFM) pulse and the hyperbolic frequency modulated (HFM) pulse.

The popularity of these signals comes from their pulse compression characteristics. Pulse compression allows achieving transmitted power of a relatively long pulse while obtaining the range resolution corresponding to a short CW pulse [19].

These two classes of signals, are defined in subsections (a) and (b).

a)   LFM pulse [20]

$$x(t) = a(t)\cos\left(2\pi f_c t + D_p t^2\right) \quad \text{for} \quad |t| \le T/2, \tag{3.19}$$

where $a(t)$ is a real amplitude modulating function, $D_p \triangleq \pm\dfrac{\pi}{T}B$ is the phase deviation constant in rad/sec^2, B is the swept bandwidth in Hz, and T is the pulse duration in seconds. The instantaneous frequency is defined as

$$\begin{aligned} f_i(t) &= \frac{1}{2\pi}\frac{d}{dt}\left(2\pi f_c t + D_p t^2\right) \\ &= f_c + \frac{1}{\pi}D_p t. \end{aligned} \tag{3.20}$$

In complex notation, Equation (3.19) then becomes

$$x(t) = a(t)e^{j\left(2\pi f_c t + D_p t^2\right)}. \tag{3.21}$$
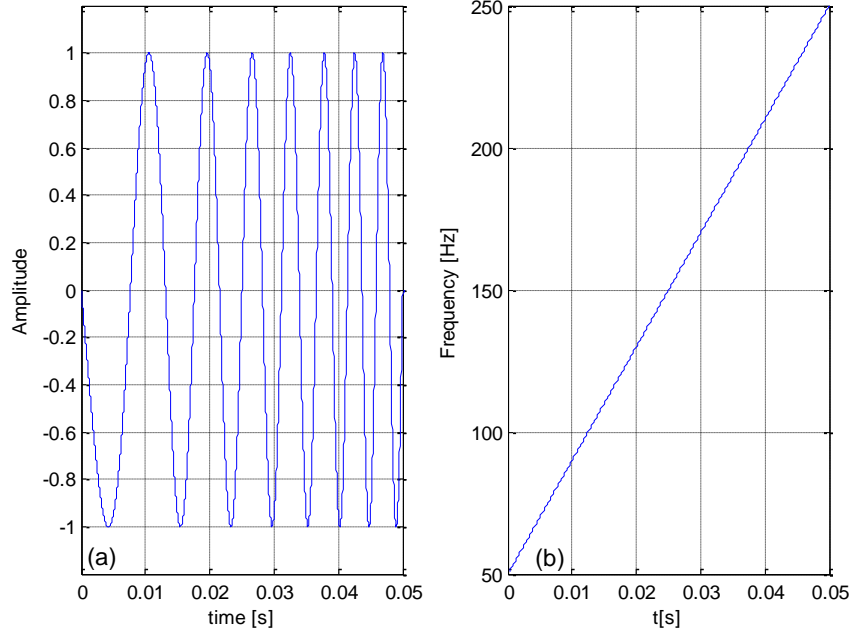
This LFM pulse is defined in the interval $0 < t < 50ms$ with $B = 200Hz$ (TB=10).

Figure 7.   Rectangular-Envelope (a) LFM Pulse and (b) Instantaneous Frequency

b)   HFM pulse [21]

$$x(t) = a(t)\cos\left[\frac{2\pi}{\kappa}\ln\left(1 + \kappa f_o t\right)\right] \quad \text{for} \quad |t| \le T/2 , \tag{3.22}$$

where $a(t)$ is a real amplitude modulating function, $\kappa = \dfrac{f_o - f_{end}}{Tf_o f_{end}}$, f_o and f_{end} are, respectively, the starting and the ending frequency in Hz, and T is the pulse duration in seconds. The HFM swept bandwidth is defined as $B = \pm\left(f_o - f_{end}\right)$ (+ for up sweep and − for down sweep). The instantaneous frequency is

$$\begin{aligned} f_i(t) &= \frac{1}{2\pi}\frac{d}{dt}\left[\frac{2\pi}{\kappa}\ln\left(1 + \kappa f_o t\right)\right] \\ &= \frac{f_o}{1 + \kappa f_o t} . \end{aligned} \tag{3.23}$$

In complex notation, Equation (3.22) then becomes

$$x(t) = a(t)e^{j\frac{2\pi}{\kappa}\ln\left(1 + \kappa f_o t\right)} . \tag{3.24}$$

23
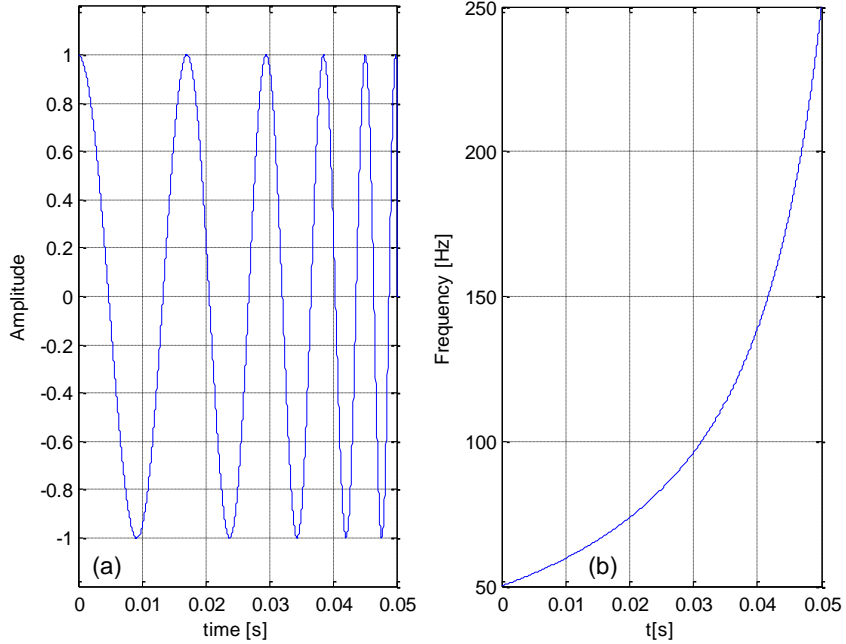
This HFM pulse is defined in the interval $0 < t < 50ms$ with $B = 200$Hz (TB=10).

Figure 8.   Rectangular-Envelope (a) HFM Pulse and (b) Instantaneous Frequency

The behavior of LFM pulses in the presence of Doppler will depend on the signal time-bandwidth (*TB*) product, source-target relative radial speed (v_r), and the characteristic medium propagation speed (c). In a stationary source and target scenario, the nominal half-width of the main lobe in the matched filter output is *1/B* [17]. The Doppler will cause a widening in the main lobe that is accompanied by a reduction in amplitude (due to conservation of energy) of the matched filter output's peak. Depending on how severe the widening effect is, it will be necessary to use a "bank" of matched filters to permit target detection.

The matched filter output is shown in Figure 9 for three scenarios of source-target relative motion: stationary, relative radial speed of 7.5 knots, and relative radial speed of 15 knots. The transmitted waveform is a rectangular-envelope LFM pulse of 50 ms duration, sweeping from 9 kHz to 14 kHz (*TB*=250). As shown in Figure 9, when there is no motion, the pulse arrives at 0.1s.
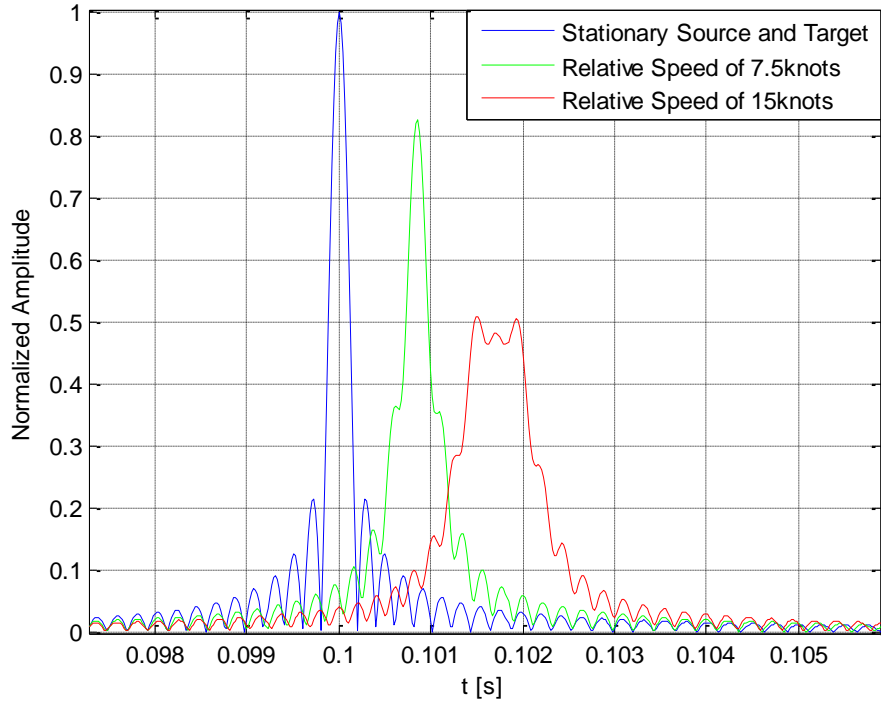
The characteristics of the LFM pulse are: T=50ms, B=5 kHz sweeping from 9 kHz to 14 kHz (TB=250).

Figure 9.   Matched Filter Output Having as Input a Rectangular-Envelope LFM Pulse for Different Source-Target Relative Radial Speeds

Note that the width of the main lobe increases with the increase of the radial speed, and the peak amplitude decreases. Note, too, that there is a temporal offset in the matched filter's output peak when relative motion between source and target is present. Figure 9 illustrates a negative Doppler shift (source and target are receding) so the relative speed increases the round trip time delay estimated at the receiver.

As demonstrated in the Appendix, the widening in the main lobe of the matched filter output is given by the factor $1+\left(4v_r/c\right)TB$. If $\left(4v_r/c\right)TB$ can be considered much smaller than unity, the widening and, consequently, the amplitude reduction in the matched filter output peak may be neglected, which implies

$$TB \ll \frac{c}{4v_r}\,. \tag{3.25}$$

25

Equation (3.25) states that if the signal's time bandwidth product is small in comparison with the ratio of medium sound speed over the maximum source-target relative radial speed, the widening effect in the matched filter output may be neglected. In radar and laser applications, due to the large difference between c and v_r, LFM pulses can be used without issues, even for relatively large *TB*. However, in underwater acoustics, due to the relative lower sound speed propagation, the use of this signal can introduce limitations in the system's ability to detect a target.

For HFM pulses (as demonstrated in the Appendix), the main lobe in the matched filter output, in the presence of Doppler, is slightly different from *1/B* and independent of $(4v_r/c)TB$. Thus, the widening and, consequently, the reduction in the matched filter output's peak will not be as severe as in the LFM case, and may permit target detection without the use of a multi-hypothesis detector.

The matched filter output is shown in Figure 10 for three scenarios of source-target relative motion: stationary, relative radial speed of 7.5 knots, and relative radial speed of 15 knots. The transmitted waveform is a rectangular-envelope HFM pulse of 50 ms duration, sweeping from 9 kHz to 14 kHz (*TB*=250), and a single echo is considered to be received at *t=0.1s*. Note that the width of the main lobe barely changes with the increase of the radial speed, and the peak amplitude slightly decreases. Note, too, that as in the LFM case, there is a temporal offset in the matched filter's output peak when relative motion between source and target is present.
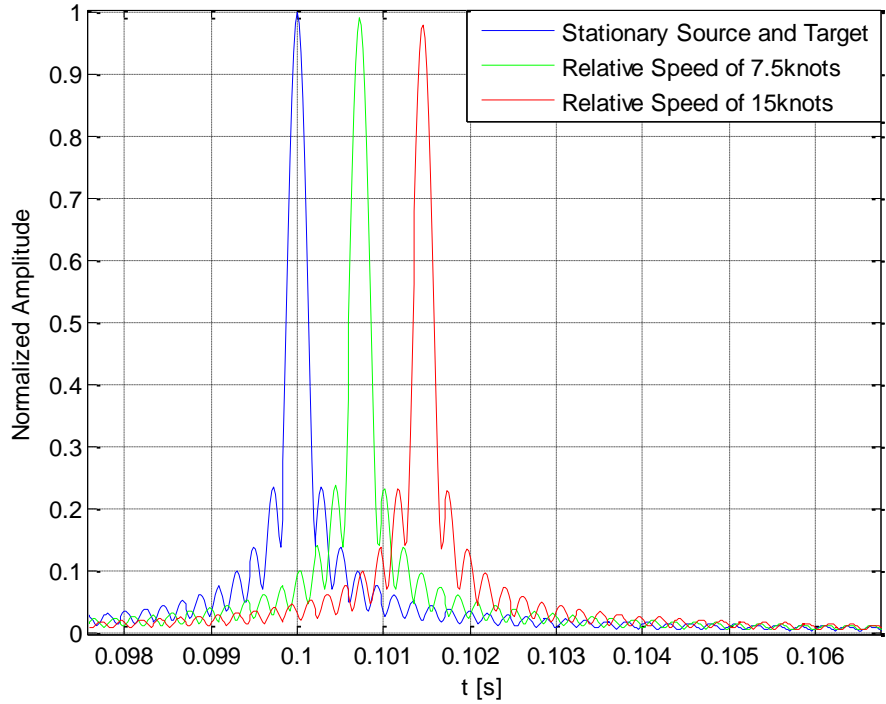
The characteristics of the HFM pulse are: T=50ms, B=5 kHz sweeping from 9 kHz to 14 kHz (TB=250).

Figure 10. Matched Filter Output Having as Input a Rectangular-Envelope HFM Pulse for Different Source-Target Relative Radial Speeds

As seen in Figures 9 and 10, with the use of both waveforms, the relative speed between source and target causes a temporal offset in the matched filter output's peak. Compensation for this temporal offset should be applied to obtain a precise travel time measurement.

The use of HFM pulses permits a direct compensation for this time offset by using a closed form expression (Appendix, Equation A.61) when the Doppler shift is known. Unfortunately, there is no closed form for LFM pulses.

Due to these effects, most ranging applications in underwater acoustics use HFM pulses and, as will be seen in the next chapter, HFM pulses are employed in the acoustic modems used in this work.

27

THIS PAGE INTENTIONALLY LEFT BLANK

IV. RANGE ESTIMATION

Parts of this chapter were previously published by IEEE [1].[*]

As seen in Chapter III, the standard technique to estimate the distance to a target in radar or active sonar applications begins with the determination of the travel time. It can be done by cross-correlating the received signal (the backscattered echo) with a replica of the transmitted signal (or match filtering the received signal). The two-way travel time can then be estimated from the time lag where the peak in the cross-correlation occurs.

In this chapter, a technique to estimate the distance using the measured travel time and a ray tracing code to model the acoustic channel is addressed. To start this discussion, the next section provides a basic description of the ranging routine used by the Teledyne-Benthos acoustic modems.

A. ACOUSTIC MODEM RANGING ROUTINE

In this dissertation, Teledyne-Benthos ATM-900 series acoustic modems have been used. The modems installed in the different assets have a built-in ranging routine that makes use of HFM pulses to estimate the two-way travel time between modems. The HFM pulse used by the acoustic modems has a 50 ms duration and 5 kHz bandwidth (sweeping from 9 to 14 kHz). The basics of the Teledyne-Benthos built-in ranging routine can be described in the following manner.

Consider a situation where two modems are separated by some distance R and modem-1 requests a range to modem-2, as indicated in Figure 11.
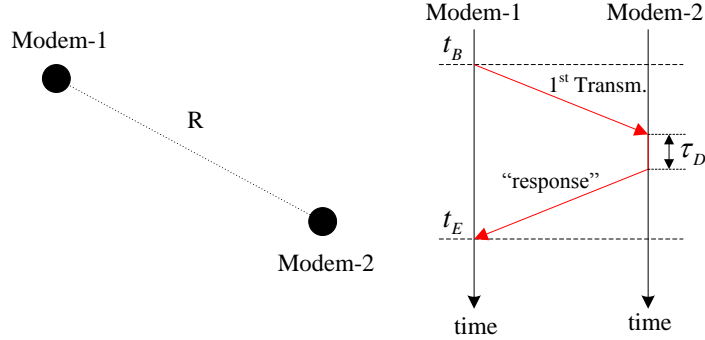
Figure 11.   Teledyne-Benthos Ranging Routine. Adapted from [22].

Initially, modem-1 transmits via MFSK (multiple frequency shift keying) a utility package to modem-2 preceded by an HFM pulse, recording the time when the routine starts (t_B). The HFM pulse can be considered as a probe signal that, after matched filtering, provides an estimate of the channel impulse response (Section B.2.b). With the help of a matched filter in modem-2, the incoming signal is detected and an estimate for the time of arrival is made based on the highest peak in the matched filter output. Modem-2 then replies to the range request after a known time delay τ_D, sending an MFSK message ("response") containing the time delay (and other information unrelated to range estimation) preceded by an HFM pulse. Modem-1 now estimates the time of arrival (t_E) from the highest peak in the matched filter output. From the time difference between t_E and t_B (minus τ_D), the two-way travel time (τ_{2way}) is estimated by modem-1 according [22], [23]

$$\tau_{2way} = (t_E - t_B) - \tau_D. \tag{4.1}$$

At this point, modem-1 provides a rough estimate of the slant range R by multiplying the one-way travel time $t_m = \tau_{2way}/2$, by the characteristic sound speed of the medium. A more accurate technique to estimate the distance using a ray tracing code to model the environment is addressed in Section B.2.

For completeness, it is worth noting the capability of the modems to compensate for the Doppler effect. The ability of HFM pulses to enhance target detection in the presence of Doppler shift was discussed in Chapter III and is demonstrated in the

Appendix. In addition, a closed expression for the temporal offset in the matched filter output due to source-target relative motion is provided.

By measuring the Doppler shift, the temporal offset in the matched filter output can be compensated using a variation of Equation (A.61) of the Appendix. Teledyne-Benthos acoustic modems have a patented algorithm that makes use of single frequency tonals to measure the Doppler shift and then compensate for the temporal offset in the matched filter output [18] without relying on a new matched filter.

B.   DISTANCE MEASUREMENT

In an environment where the speed of propagation is approximately constant, the distance between source and target may be estimated by a simple multiplication between the characteristic propagation speed of the medium and the estimated one-way travel time. This is generally not the case in underwater acoustics, however, where the sound speed varies spatially. Even in a benign, range-independent environment, the sound speed is generally observed to vary with depth (see Figure 12).
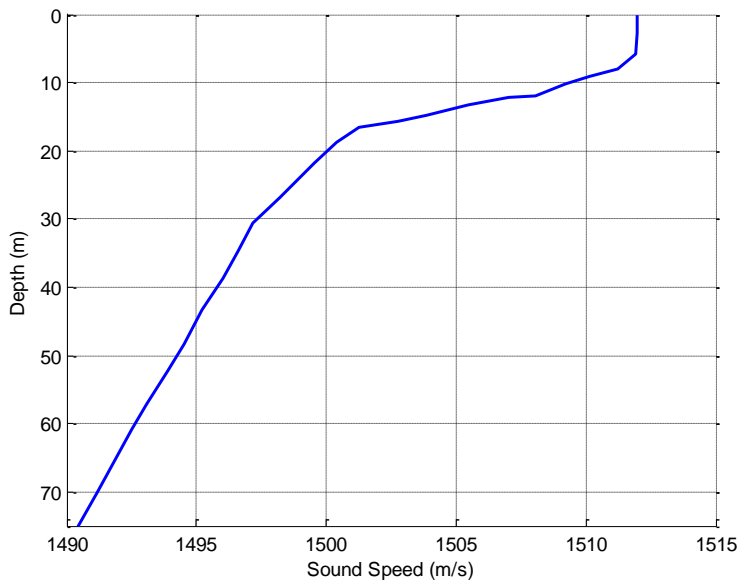
Figure 12.   Sound Speed Profile Measured in Monterey Bay on August 12, 2015

Another important characteristic in underwater acoustics is the multipath nature of the propagation. In a multipath environment, multiple arrivals reach the receiving transducer at different times by different propagation paths, causing several peaks in the matched filter output. A common approach is to estimate the travel time by the time of the highest peak, which considers that the highest peak represents the arrival with higher energy and, therefore, the direct path between source and target (see Section A).

Occasionally, in a multipath environment where the horizontal distance between source and target is much larger than the depth of the water, the highest peak in the matched filter output (representing the arrival with higher energy) does not represent a wave traveling along the direct path. For example, the highest peak could be due to an arrival taking the bottom/surface bounce path, as depicted in Figure 13. An attempt to use the measured travel time to estimate a distance between source and target, assuming that it is representative of the direct path, will cause errors in the final distance estimation.
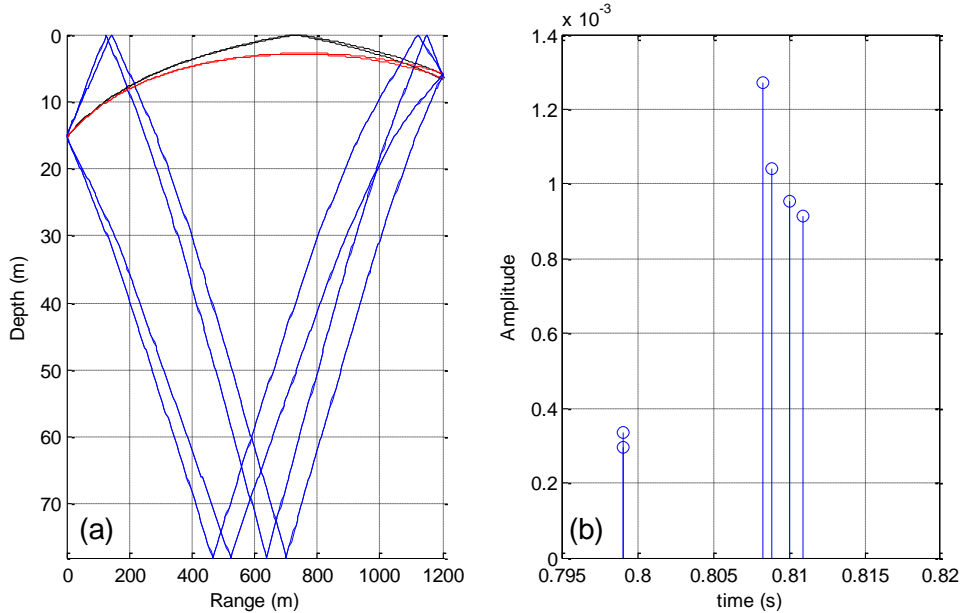
In ray tracing, eigenrays are defined as rays that connect the source to a particular receiver location. Note that, in this example, the first group of arrivals has smaller amplitude than the second group.

Figure 13.   Example Calculation of (a) Eigenray Paths and
(b) Eigenray Times of Arrival for Omnidirectional
Source and Receiver Using BELLHOP [24]

32

In this dissertation, an approach is developed that utilizes an efficient ray tracing code [24], in situ sound speed measurements, sea floor modeling, and the measured acoustic wave travel time to estimate the distance between the UUV and the reference points. The ray tracing code can then distinguish cases in which the strongest arrival is not representative of the direct path (or first arrival). Additionally, with information of the sound speed profile, the refraction of the sound waves is accounted for in the distance estimation.

1. Acoustic Ray Paths

Initial attempts at modeling sound propagation underwater were motivated by problems in predicting sonar performance during World War II in support of anti-submarine warfare operations. These first models used ray tracing techniques derived from the wave equation [25].

From a historical point of view, the behavior of ray paths was studied long before acoustic ray theory was mathematically formalized. Ray theory originally emerged from optics, where it was used to understand propagation of light even before the Maxwell equations were known. In fact, ray paths were originally studied by Euclid (around 300 BC) [26] and complemented by the Arabic scientist Alhazen in the tenth century, while Snell's law only dates back to 1626 [27].

Nowadays, the research community has lost, in part, some interest in ray tracing codes mainly due to their inherent high frequency approximation, which in certain cases can lead to coarse accuracy in the results. In high frequency applications, however, ray tracing algorithms are very popular due to their accuracy and high processing speeds. A brief discussion about the high frequency approximation can be found in Section B.1.b.

a. The Acoustic Wave Equation

The linearized wave equation can be derived from the equation of continuity, the Euler equation, and the equation of state [28]. In the absence of density discontinuities, it takes the form

$$\nabla^2 p - \frac{1}{c^2}\frac{\partial^2 p}{\partial t^2} = 0. \tag{4.2}$$

Density discontinuities at interfaces can be treated separately within the context of reflection and transmission coefficients at boundaries.

To obtain a time-independent wave equation (Helmholtz equation), a time harmonic solution for the acoustic pressure p is assumed at the form

$$p = p(\vec{r})e^{j\omega t}, \tag{4.3}$$

where the position vector $\vec{r}$ extends from the reference point to a certain point in the field. Substituting Equation (4.3) into Equation (4.2), the wave equation reduces to the Helmholtz equation

$$\nabla^2 p(\vec{r}) + k(\vec{r})^2 \, p(\vec{r}) = 0, \tag{4.4}$$

where $k(\vec{r}) = \omega/c(\vec{r})$. In this form, all of the spatially varying environmental factors that affect the propagation are incorporated into $k(\vec{r})$.

b.   *Mathematical Derivation*

Assuming a solution in the format of the product of an amplitude function $A(\vec{r})$ and a phase function $\omega\tau(\vec{r})$, we may define

$$p(\vec{r}) = A(\vec{r})e^{j\omega\tau(\vec{r})}. \tag{4.5}$$

Substituting this into the wave equation and equating the real and imaginary parts, yields

$$\left|\nabla\tau(\vec{r})\right|^2 = \frac{1}{c(\vec{r})^2} + \frac{\nabla^2 A(\vec{r})}{A(\vec{r})\omega^2}, \tag{4.6}$$

and

$$2\nabla A(\vec{r})\cdot\nabla\tau(\vec{r}) + A(\vec{r})\nabla^2\tau(\vec{r}) = 0. \tag{4.7}$$

Taking the asymptotic limit $\omega \to \infty$ in Equation (4.6), we obtain

$$\left|\nabla\tau(\vec{r})\right|^2 = \frac{1}{c(\vec{r})^2} \tag{4.8}$$

Equation (4.8) is referred as the Eikonal equation and describes the evolution of the phase front in space or the ray paths (see Figure 14). Equation (4.7) is called the Transport equation and describes the evolution of the amplitude along the ray paths.
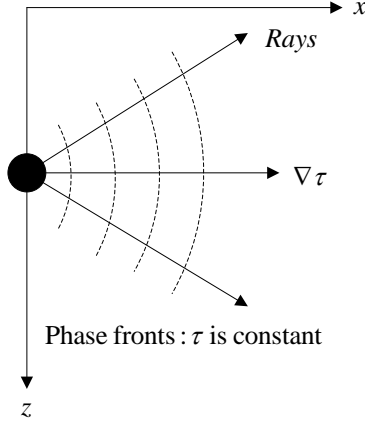
Figure 14.   Rays and Phase Fronts. Adapted from [26].

Instead of assuming the asymptotic limit $\omega \to \infty$ in Equation (4.6), a different argument can be made. For frequencies such that $\dfrac{\nabla^2 A(\vec{r})}{A(\vec{r})\omega^2} \ll \dfrac{1}{c(\vec{r})^2}$, the Eikonal equation is achieved.

Other authors propose a similar argument as in [28], requiring that $\left| \dfrac{\nabla^2 A(\vec{r})}{A(\vec{r})} \right| \ll \dfrac{\omega^2}{c(\vec{r})^2}$. According to this argument, the sufficient condition to be satisfied is that the amplitude of the wave and the speed of sound must not change significantly over distances comparable to a wavelength. The result of all of the previous arguments is basically the same, and at this point we can just say that a high frequency approximation is used to obtain the Eikonal equation.

c.   *Solving the Eikonal Equation*

The Eikonal equation is a first-order, nonlinear, partial differential equation that is usually solved by the method of characteristics [29]. The method of characteristics

essentially involves recognizing that $\nabla \tau$ is everywhere perpendicular to the phase front [30]. This defines the local direction of the ray trajectories, which are everywhere perpendicular to the acoustics phase fronts.

If we introduce a family of curves that describes the evolution of the phase front by defining them as perpendicular to the phase front everywhere, then the ray paths are points in space, $\vec{r}(s)$, defined by

$$\frac{d\vec{r}}{ds} = c \nabla \tau ,\tag{4.9}$$

where s is the distance along the trajectory or the arc length along the ray. The factor c is included in Equation (4.9) such that the tangent vector along the ray has unit length.

It can be shown [26] that solutions to the ray paths in two dimensions satisfy a set of coupled, first-order differential equations of the form

$$\frac{dr}{ds} = \alpha c , \quad \frac{dz}{ds} = \beta c ,\tag{4.10}$$

and

$$\frac{d\alpha}{ds} = -\frac{1}{c^2}\frac{\partial c}{\partial r}, \quad \frac{d\beta}{ds} = -\frac{1}{c^2}\frac{\partial c}{\partial z},\tag{4.11}$$

that can be numerically solved by a variety of methods. Considering a trajectory in two dimensions (r, z), we require as an initial condition that the rays start at the source position (r_o, z_o) and have a defined launch angle, θ_o (see Figure 15), where

$$tan(\theta_o) = \frac{dz}{dr} = \frac{dz/ds}{dr/ds} = \frac{sin(\theta_o)}{cos(\theta_o)}.\tag{4.12}$$

Substituting Equation (4.10) into Equation (4.12), we obtain

$$sin(\theta_o) = \frac{dz}{ds} = \beta_{ro}c(r_o, z_o) \Rightarrow \beta_{ro} = \frac{1}{c(r_o, z_o)}\frac{dz}{ds}\tag{4.13}$$

and

$$cos(\theta_o) = \frac{dr}{ds} = \alpha_{ro}c(r_o, z_o) \Rightarrow \alpha_{ro} = \frac{1}{c(r_o, z_o)}\frac{dr}{ds},\tag{4.14}$$

which provides the initial conditions for the parameters α and β in terms of the launch angle and the speed of the sound at the source position.
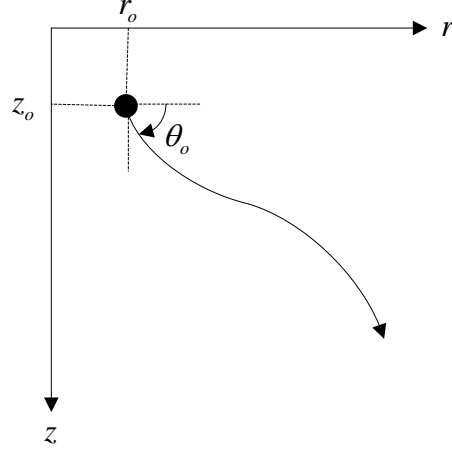
Figure 15.　Rays 2D Initial Conditions

The ray paths characterized by Equations (4.10) and (4.11), along with the initial conditions, describe the direction in which the phase front evolves spatially. But they do not describe the amplitude of the pressure field. To obtain the complete description of the pressure field, it is necessary to associate a phase and amplitude for each ray.

The phase along a ray path can be determined from the Eikonal equation,

$$\nabla \tau \cdot \nabla \tau = \frac{1}{c^2} \,. \tag{4.15}$$

Substituting Equation (4.9) into Equation (4.15), we obtain

$$\nabla \tau \cdot \frac{1}{c} \frac{d\vec{r}}{ds} = \frac{1}{c^2}, \tag{4.16}$$

and simplifying yields

$$\frac{d\tau}{ds} = \frac{1}{c} \Rightarrow \tau(s) = \int_0^s \frac{1}{c(s')} \, ds', \tag{4.17}$$

where $\tau(s)$ is the travel time along the ray and the phase is $\omega \tau(s)$. In a multipath environment, $\tau(s)$ is important to estimate the time which different arrivals reach the receiver, as depicted in Figure 13b.

37

d. Solving the Transport Equation

The amplitude along a ray path is obtained by solving the Transport equation, which may be written as

$$\nabla \cdot \left(A(\vec{r})^2 \nabla \tau(\vec{r}) \right) = 0. \tag{4.18}$$

The solution to Equation (4.18) can be developed in terms of ray-tube areas and conservation of energy flux. Consider a ray propagating in range from r_o to r, as depicted in Figure 16, a ray tube can be constructed from nearby rays passing through the small area S_o. When the ray tube reaches r, its cross sectional area will be S. Integrating Equation (4.18) over the volume of the ray tube segment, applying Gauss' theorem and recognizing that the rays are normal to the phase fronts and therefore vanish on the sides of the ray tube yields [26], [31]

$$\frac{A(r)^2}{\rho c} S = \frac{A(r_o)^2}{\rho_o c_o} S_o \tag{4.19}$$

and

$$A(r) = A(r_o)\sqrt{\frac{\rho c}{\rho_o c_o} \frac{S_o}{S}}. \tag{4.20}$$

Equation (4.20) implies a rising or falling amplitude as the ray tube shrinks and expands.
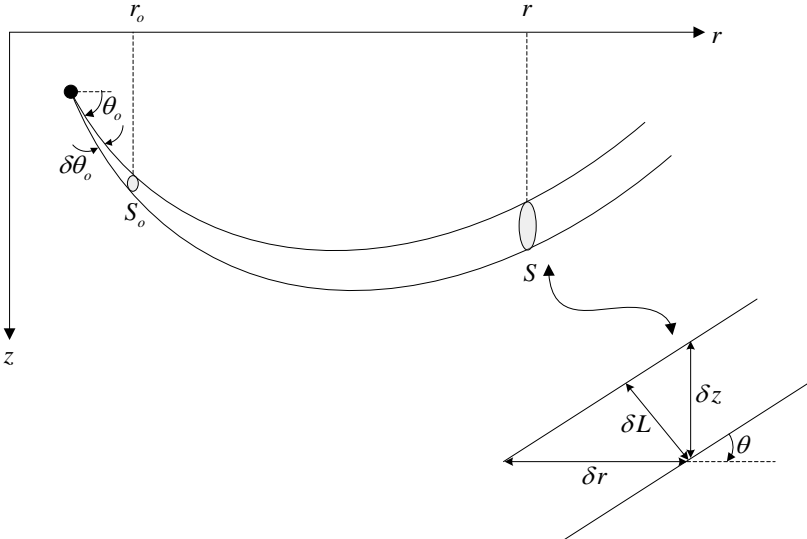
Figure 16.   Geometry of a Ray Tube

38

As shown in [30], the amplitude of the field within a ray "tube" can be expressed as

$$A(r) = A(r_o) \sqrt{\frac{r_o}{r} \frac{\rho c}{\rho_o c_o} \frac{\delta\phi_o \sin\theta_o}{\delta\phi \sin\theta} \frac{r_o \delta\theta_o}{\delta z}}$$

$$\Rightarrow \left(\frac{A(r)}{A(r_o)} \right)^2 = \frac{r_o}{r} \frac{\rho c}{\rho_o c_o} \frac{\delta\phi_o \sin\theta_o}{\delta\phi \sin\theta} \frac{r_o \delta\theta_o}{\delta z}.$$

(4.21)

In terms of transmission loss (*TL*),

$$TL = -10\log\left(\frac{|p|^2}{P_o^2} \right) dB \ \ re \ r_o,$$

(4.22)

or

$$TL(r,z) = 10\log\left(\frac{r}{r_o} \right) - 10\log\left(\frac{\rho c}{\rho_o c_o} \right) - 10\log\left(\frac{\delta\phi_o \sin\theta_o}{\delta\phi \sin\theta} \right) + 10\log\left(\frac{\delta z(r,z)}{r_o \delta\theta_o} \right).$$

(4.23)

The first term in Equation (4.23) represents cylindrical spreading, the second and third terms account for variations in the medium density and average angle of propagation of the ray tube. The last term shows the effects of ray spreading or converging, which dominates the 2D field structure.

The equation for the evolution of the ray amplitude, Equation (4.21), reveals two important features in ray propagation:

1) $\delta z \rightarrow 0$: when the vertical spread of the rays δz and, consequently, the area *S* tends to zero, a high intensity region is formed where all the rays in the tube converge to a focal point or caustic. In this region, the amplitude tends to infinity, which is a limitation of classical ray theory;

2) $\delta z < 0$: after passing through a caustic, δz changes sign and the amplitude can become complex; therefore, Equation (4.21) may be rewritten as

$$A(r) = A(r_o) \sqrt{\frac{r_o}{r} \frac{\rho c}{\rho_o c_o} \frac{\delta\phi_o \sin\theta_o}{\delta\phi \sin\theta} \frac{r_o \delta\theta_o}{\delta z}} \ e^{jN\frac{\pi}{2}}.$$

(4.24)

The exponential term in Equation (4.24) indicates a $\pi/2$ phase change at each caustic (N represents the number of caustics). Therefore, to obtain the correct phase of the

pressure field, it is necessary to keep track of the number of caustics encountered by the rays.

In addition to the phase changes that occur at caustics, rays also undergo phase changes at reflections. For reflections from the surface (which can be treated as a pressure release boundary), each ray picks up a π phase shift. Reflections at the seafloor can become more complicated because the phase change depends upon the reflection angle, which can vary considerably among all the rays contributing to the field solution at a point. Bottom reflections are generally not treated as ideal, but contribute to some loss in amplitude along the ray path. The complete description of the field at a point using a ray approach may then be defined as [30]

$$p(\vec{x}) = \sum_{m=1}^{M} |A_m(r)| \left[\prod_{n=1}^{N_{b,m}} \Re_{m,n}(r'_{m,n}) \right] e^{-i\omega \int_0^{s_m} \frac{1}{c(s'_m)} ds'_m} e^{iN_{c,m}\frac{\pi}{2}} e^{iN_{s,m}\pi} , \qquad (4.25)$$

where $m = 1,\ldots M$ are the number of eigenrays, $|A_m|$ is the amplitude of the mth eigenray, $\Re_{m,n}(r'_{m,n})$ is the reflection coefficient (which may be complex) for circumstances in which the mth eigenray encountered $N_{b,m}$ bottom reflections at points $r'_{m,n}$, $N_{c,m}$ is the number of caustics, and $N_{s,m}$ is the number of surface reflections of the mth eigenray. The actual trajectory of the eigenray is defined by the path s_m. Keeping track of all of the various factors that determine the pressure field from ray calculations can be a challenging task, and is at the root of all acoustic ray tracing models.

e. Geometric and Gaussian Beams

In addition to caustics, the standard ray tracing method produces perfect shadow zones, which represent limitations of the classical theory. One way to deal with such artifacts is the use of geometric or Gaussian beams [26], [32], and [33]. This approach permits some leakage energy in the shadow zones and smooths out the caustics, providing a good agreement with more computationally intensive full-wave models.

As described in [26], a beam is constructed around each ray where the amplitude of the beam is tapered to vary from the central ray, decaying to zero on either side. The

half-width $W(s)$ of the beam is defined by the distance from the central ray where the beam amplitude is made to vanish. This width is chosen precisely so that the beam vanishes at the location of its neighboring ray. Thus, the pressure for the beam is given by

$$P^{beam}(s,n) = A^{beam}(s)\phi(s,n)e^{j\omega\tau(s)}, \qquad (4.26)$$

where $\phi(s)$ can be the hat-shaped function (geometric beam) [32] or a Gaussian function (Gaussian beam) [34], respectively

$$\phi(s,n) = \begin{cases} \dfrac{W(s)-n}{W(s)} & \text{for } n \leq W(s) \\ 0 & \text{elsewhere} \end{cases}, \qquad (4.27)$$

or

$$\phi(s,n) = e^{-\left(\frac{n}{W(s)}\right)^2}, \qquad (4.28)$$

where $n = 0$ represents the central ray. In this approach, the ray becomes a central ray of a Gaussian varying beam, Equation (4.28), or a linear varying beam, Equation (4.27), as depicted in Figure 17.
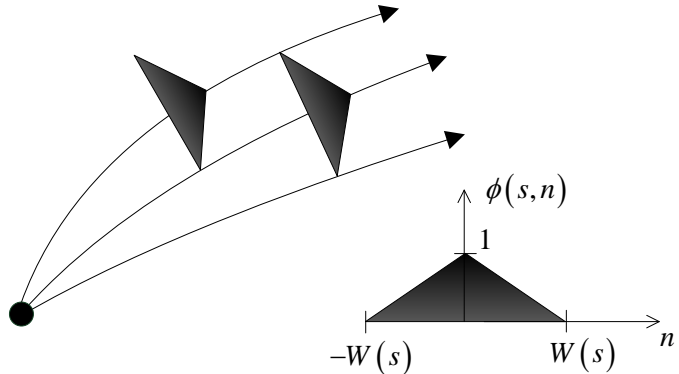
Figure 17.   Geometric Beams around Each Ray. Adapted from [32].

f.   BELLHOP Beam Tracing Model

In this dissertation, the ray tracing code used is BELLHOP, developed by Michael Porter and available under GNU public license in the Ocean Acoustic Library website. According to [24], BELLHOP is a beam tracing model for predicting acoustic pressure

fields in ocean environments where several types of beams may be implemented, including Gaussian and hat-shaped beams, with both geometric and physics-based spreading laws. BELLHOP can generate a variety of outputs including transmission loss and eigenrays. It allows for range-dependence in the top and bottom boundaries (altimetry and bathymetry), as well as in the sound speed profile. Additional input files permit the specification of directional sources as well as geoacoustic properties for the bounding media. Top and bottom reflection coefficients may also be included.

The eigenrays (amplitude and phase) represent the ideal channel impulse response (IR). This computation is done exactly the same way as is done for a regular ray trace. However, BELLHOP only saves the rays whose associated beams make a contribution to the specified receiver location.

2. Matched Peak Impulse Response Processor

In this section an algorithm that makes use of a ray tracing code to model the environment is developed to estimate the range between a UUV and a reference point. The use of a ray tracing code permits us to take into account the multipath and the refraction of the sound waves in the range estimation.

a. Motivation

Problems involving estimates of distances underwater belong to a broader class of source localization problems which have been extensively studied. The state-of-the-art approach makes use of techniques such as matched field processing [35] or matched IR processing [36] to estimate several acoustic parameters, including source position and horizontal distances from source to target.

Those techniques involve acoustic field measurements (in the case of the matched field processing) or channel IR measurements (in the case of the matched IR processing), and acoustic propagation models to generate synthetic patterns. These synthetic patterns are then, iteratively, used to match the complete measured pattern.

This approach can produce good results in estimating distances underwater but demands very high computational efforts and may take hours to converge. Therefore, it is

not suitable for use in real-time applications. In what follows, it will be shown that the acoustic modem's matched filter output may be considered for estimation of the channel IR (measured estimation). This estimation can be emulated, generating a prediction for the channel IR (synthetic prediction).

The synthetic predicted channel IR can then be used iteratively to match the measured estimated channel IR. However, instead of trying to match the entire time series, as in the traditional approach, only the arrival with the highest amplitude is utilized (see Section A). This algorithm shall run inside the UUV and is fast enough to work in real-time.

b.   *Acoustic Channel IR Estimation*

In practical applications in which a single source transmits to a receiver, an estimate of the acoustic channel IR is obtained by transmitting a broadband pulse (like a chirp) from the source, which is then match filtered (or cross-correlated) at the receiver. Assuming that the received signal $x'(t)$ is cross-correlated with a replica of the transmitted signal, $x(t)$, such that

$$\hat{h}(t) = \int_{-\infty}^{+\infty} x'(\tau)\, x^*(t+\tau)\, d\tau, \tag{4.29}$$

then $\hat{h}(t)$ may represent an estimation for the channel IR.

The received signal can be understood as being the result of the convolution between the transmitted signal and the acoustic channel complex IR plus noise (for simplicity, no attenuation or other propagation effects are being considered). Specifically,

$$x'(\tau) = \int_{-\infty}^{+\infty} h(\alpha)\, x(\tau-\alpha)\, d\alpha + n(\tau), \tag{4.30}$$

where $h(\alpha)$ is the true acoustic channel IR. Substituting Equation (4.30) into (4.29) yields

$$\hat{h}(t) = \int_{-\infty}^{+\infty} \left[\int_{-\infty}^{+\infty} h(\alpha)\, x(\tau-\alpha)\, d\alpha + n(\tau) \right] x^*(t+\tau)\, d\tau$$

$$= \int_{-\infty}^{+\infty} h(\alpha) \left[\int_{-\infty}^{+\infty} x(\tau-\alpha) x^*(t+\tau)\, d\tau \right] d\alpha + \int_{-\infty}^{+\infty} n(\tau) x^*(t+\tau)\, d\tau .$$

(4.31)

If the transmitted signal autocorrelation has an impulse-like behavior, the term in brackets in Equation (4.31) can be approximated as [36]

$$\int_{-\infty}^{+\infty} x(\tau-\alpha) x^*(t+\tau)\, d\tau \approx E_x \delta(t-\alpha),$$

(4.32)

where E_x is the energy of the signal.

Normalizing Equation (4.32) to the energy of the signal, substituting into Equation (4.31), and considering that signal and noise are uncorrelated, produces

$$\hat{h}(t) \approx \int_{-\infty}^{+\infty} h(\alpha)\, \delta(t-\alpha)\, d\alpha = h(t).$$

(4.33)

From Equations (4.32) and (4.33), we may conclude that when the transmitted signal autocorrelation approaches an impulse-like response, then the matched filter (or cross-correlation) output provides an accurate estimate of the channel IR.

As described in Chapter III, Section C, one of the most common waveforms used in underwater acoustics is the HFM pulse. The half-width of the main lobe in its autocorrelation is approximately $1/B$ (B is the swept bandwidth), which means that increasing the transmitted bandwidth improves the quality of the estimation for the channel IR. The drawback of increasing the bandwidth is that, in order to maintain the same SNR at the receiver, the power of the signal must be increased since noise power increases with bandwidth.

c. *Matched Peak IR Processor Algorithm*

Considering a single source and receiver, the formulation of the ray theory in the time domain permits a fast assessment of the ideal acoustic channel complex IR (amplitude and phase of the eigenrays), where each eigenray may be represented by a complex amplitude function as

$$\mathbf{A}(i) = A_i e^{j\varphi_i}, \quad i = 1, 2, \dots M ,$$

(4.34)

where A_i is the amplitude and φ_i is the phase of the ith eigenray, and M is the number of eigenrays. Note that phase φ_i accounts for boundary reflections and caustics.

A synthetic received signal may be approximated by phased addition of the complex amplitude associated with each eigenray, which resembles the convolution between the ideal channel IR and a replica of the transmitted signal. According to [26], Chapter 8, a synthetic received signal may be constructed as

$$x'(t) = \sum_{m=1}^{M} A_{r_m} x(t - \tau_m) - A_{I_m} \hat{x}(t - \tau_m),$$
(4.35)

where A_{r_m}, A_{I_m}, and τ_m are, respectively, the real component of the complex amplitude, the imaginary component of the complex amplitude, and travel time of the mth eigenray. M is the number of contributing eigenrays, $x(t)$ is the transmitted signal, and $\hat{x}(t)$ is the Hilbert transform of the transmitted signal.

To emulate the signal processing made by the acoustic modems, the synthetic received signal must be shifted to baseband (for more efficient processing) and match filtered considering a baseband replica of the transmitted signal. The output of the matched filter will represent the synthetic channel IR. In this work, the time of the highest peak is defined as the predicted time, t_p.

In Section A, we have seen that the measured one-way travel time, t_m, calculated by the Benthos acoustic modems, is based on the time of the highest peak in the matched filter output. The approach used here is to iteratively attempt to match (within a tolerance) t_p with t_m by varying the horizontal distance, R, between the UUV and the reference point in the ray tracing code. The best estimate for R is achieved when $t_m - \varepsilon \leq t_p \leq t_m + \varepsilon$, where ε is the assumed tolerance.

This approach is fast enough to run on dedicated hardware in real time and is more accurate for estimation of range than a simple multiplication of the one-way travel time with the characteristic medium sound speed. Any eventual errors are small enough to be handled by the tracking algorithm, as is described in Chapter V.

The complete algorithm is depicted in Figure 18. Consider a UUV equipped with an acoustic modem operating in a known region (bottom properties and bathymetry are known), which is able to measure the sound speed of the water column. In this area, assume that a network of reference points is available, as described in Chapter II.

The UUV and one of the reference points establish acoustic communication, and the acoustic wave travel time t_m (one-way travel time) is measured. As part of this measurement, the UUV receives the coordinates of the reference point (latitude, longitude, and depth). Latitude and longitude are later used in the tracking algorithm (Chapter V).

After a successful travel time measurement, the algorithm (running inside the UUV) starts loading into the ray tracing code (BELLHOP) the first guess for the horizontal distance between the UUV and the reference point ($R = 1500 \text{ x } t_m$), having already pre-loaded the bottom properties, the bathymetry, and measured sound speed profile. Then the depth of the UUV and the depth of the reference point are loaded into BELLHOP.

BELLHOP is set to give as output the complex IR (eigenray amplitudes and phases) of the ocean waveguide. Now, the synthetic received signal can be constructed according to Equation (4.35), shifted to baseband, and match filtered. The time of the highest peak, t_p, is taken and compared with the measured one-way travel time, t_m. This process is repeated, adjusting the horizontal distance, R, until t_p and t_m match within the tolerance set by ε.
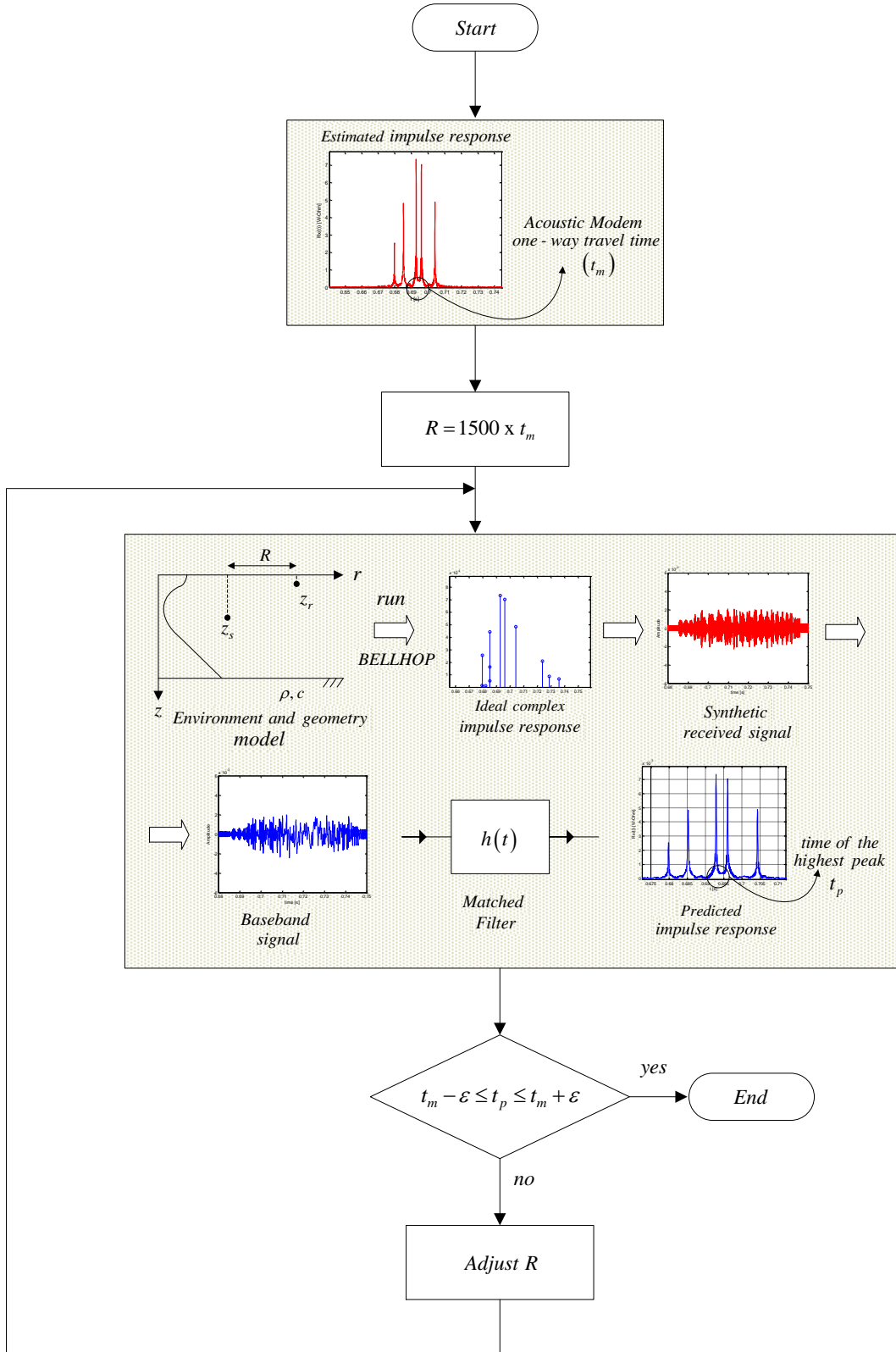
Figure 18.   Matched Peak IR Processing Flowchart

d.   Examples of Application

During the sea trials that took place in Monterey Bay on May 20, 2015, several successful travel time measurements between the UUV and the command ship were taken. In addition, the probe signal's matched filter output associated with each measurement was also recorded.

The area of operation, the bottom properties, the sound speed profile, and the assumption made for the beam patterns are described as follows.

The assets were operating in a relatively flat area, around 75 m of depth, at the edge of the Monterey Bay submarine canyon (see Figure 19).

Colorbar scale in meters.
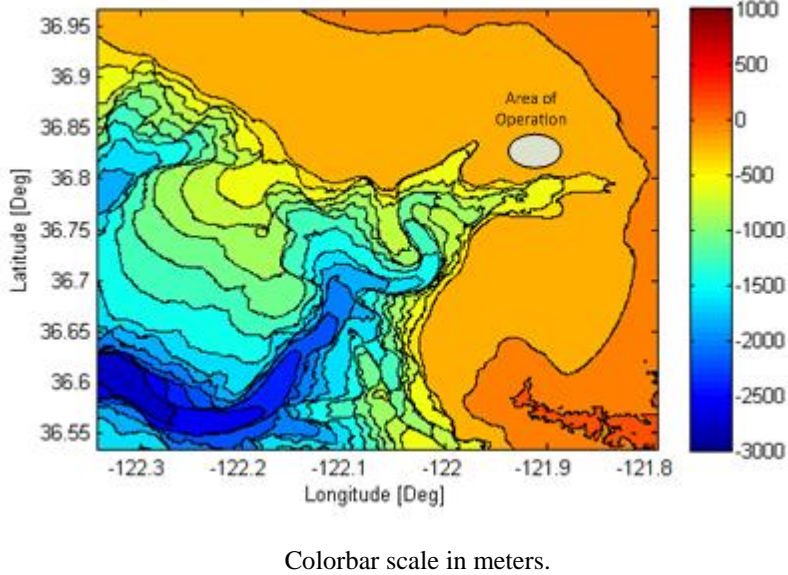
Figure 19.   Area of Operation for May 20, 2015, and August 12, 2015, Sea Trials

The bottom was modeled following Hamilton's approach [37], and the sediments were identified as being silt clay/sand-silt-clay with the following characteristics:

- Compressional sound speed: 1560 m/s;
- Density: 1.6 g/cm^3;
- Attenuation for compressional waves: 5 dB/m.

48

The sound speed profile was measured by the UUV and its average is depicted in Figure 20.
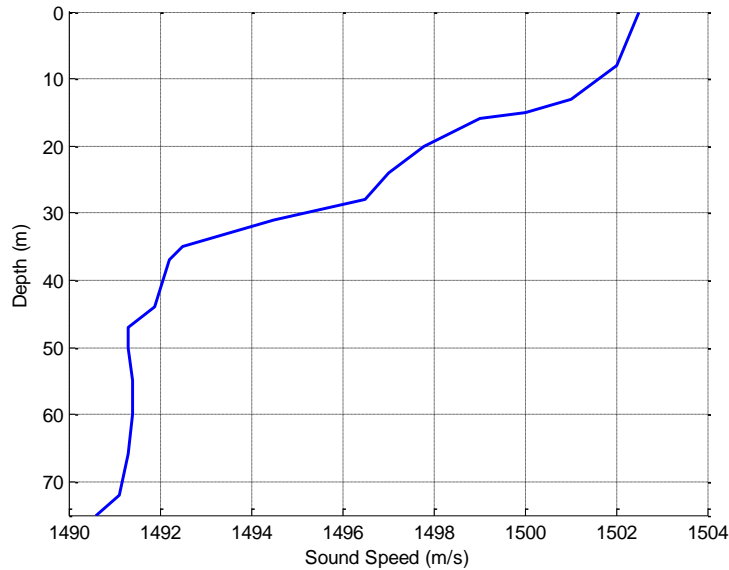
Figure 20.   Sound Speed Profile Measured by the UUV on May 20, 2015

For the purpose of calculations in this dissertation, the acoustic modem's horizontal and vertical transducer beam patterns are considered omnidirectional. This is known to be a simplification, and further efforts to characterize the beam patterns of the transducers mounted in the assets are planned.

Example 1: Mission-4: 20:55:10 (hh:mm:ss) GMT

- UUV depth: 44 m
- Command ship transducer depth: 5 m
- Measured one-way travel time (t_m): 528.13 ms
- Slant range rough estimate ($1500 \times t_m$): 792.2 m
- Horizontal range rough estimate: 791.2 m

Figure 21 shows (a) the paths of the eigenrays and (b) the amplitude and time of arrival associated with these rays. Note that the first group of arrivals (representing the direct path and a surface bounce) has smaller amplitude than the second group of arrivals (representing a bottom bounce and surface-and-bottom bounce). This counterintuitive

49

behavior is due to the spreading of the ray tubes along their trajectories, according to the following explanation.
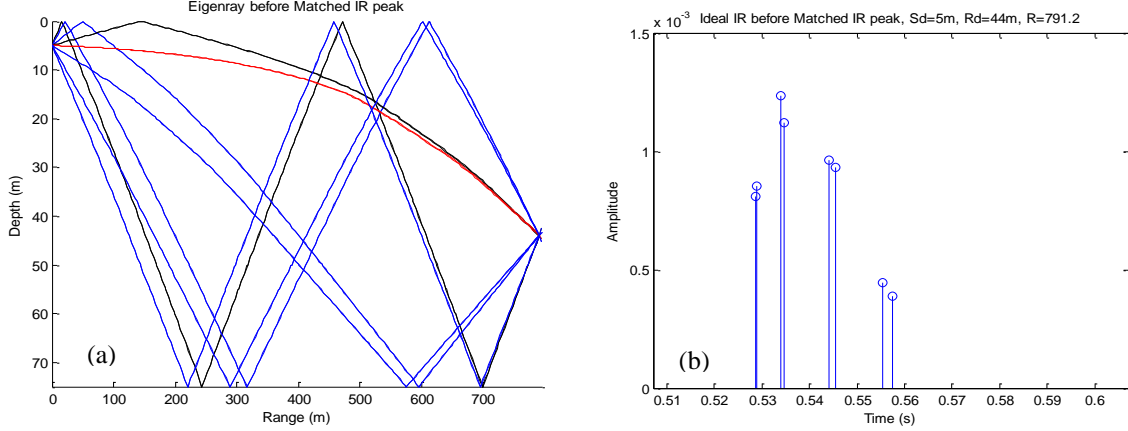
Figure 21.   (a) Eigenrays and (b) Ideal IR before Matched Peak IR Processing.
Data from Example 1

There are two rays for each arrival. Each one represents the central ray of the limiting tube that is contributing to the pressure field at the receiver (Sections B.1.e and B.1.f). These ray tubes undergo spreading and shrinking along their trajectories. The rate of spreading or shrinking is maximized in regions of large sound speed gradients. Note that in the absence of a sound speed gradient, the rays travel in straight lines and the rate of ray spreading is constant with range. For the sound speed in this environment, the sound speed gradient is primarily negative at all depths (see Figure 20), but the largest gradients are near the surface where the ocean temperature varies significantly with depth. Let us consider two situations (referring to Figure 21):

- – Those rays that arrive first follow a direct path and a nearby path that reflects from the surface. The entire propagation path of these rays is concentrated in the shallowest part of the water column where the sound speed gradient is maximum. Thus, the rate at which the associated ray tubes spread is also maximized, thereby reducing the amplitude observed at the receiver.

50

–   The next set of ray arrivals corresponds to steeper propagation paths that do not remain in the upper part of the water column. Instead, most of their propagation path is concentrated in the lower regions of the water column where the sound speed gradient is significantly smaller. The result is that the cumulative ray tube spreading along these paths is less than the direct path, and consequently the contribution to the pressure field at the receiver is larger, despite the longer path lengths and losses at the boundaries.

Figure 22 provides a comparison between (a) the acoustic modem matched filter output (measured channel IR estimation—real data) and (b) a matched filter output prediction, as described in Section B.2.c (predicted channel IR). To save memory, the modem did not record the complete matched filter output time series. For this reason, the time axes are different on the plots. Therefore, the time of the highest peak in Figures 22a, 25a, and 28a should be understood as being the measured one-way travel time (t_m) instead of what is depicted. Nevertheless, the numbers indicated on Figures 22a, 25a, and 28a are still valid to calculate the time difference between the highest peak and the first arrival.
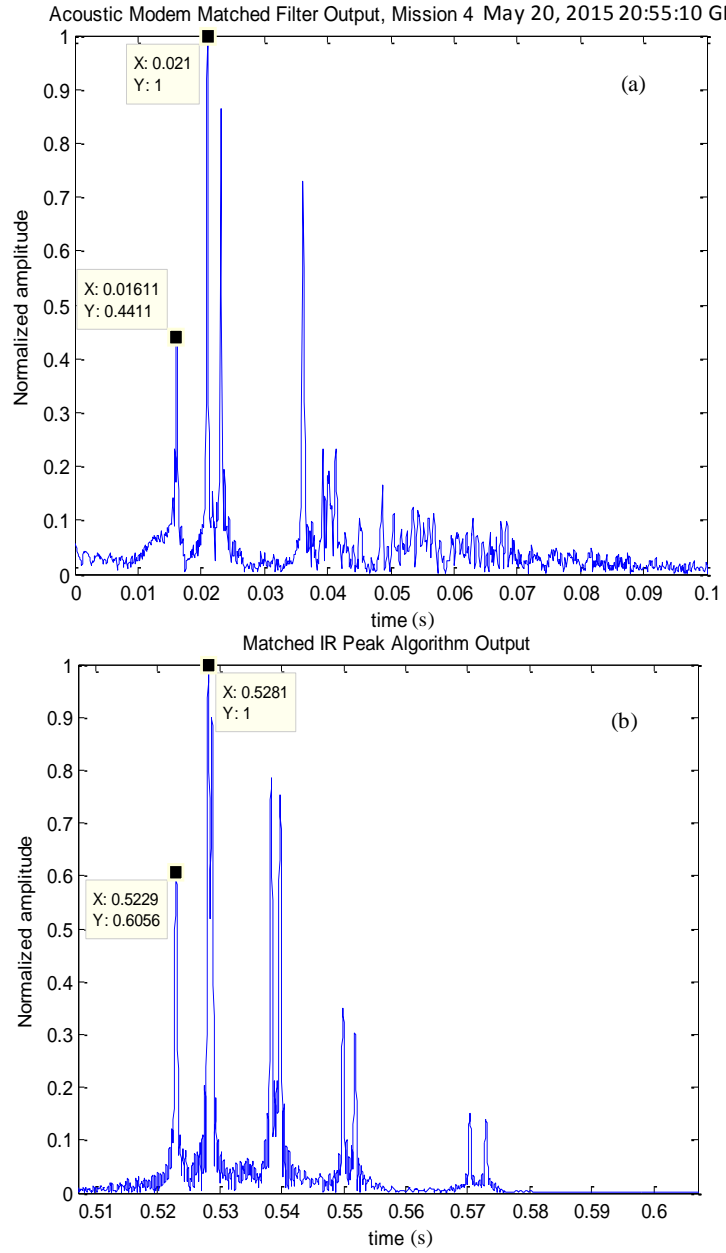
Figure 22.   Acoustic Modem (a) Matched Filter Output and
(b) Matched Peak IR Algorithm Output.
Data from Example 1

In Section B.2.c, an algorithm to match the time of the highest peak in the predicted matched filter output (predicted channel IR) with the measured one-way travel time was developed making use of a ray tracing code to model the propagation through the environment. Figure 22b represents the result of this algorithm after minimizing the

difference between measured and predicted highest peak times. Note that the time of the highest peak in Figure 22b matches with the one-way travel time measured by the acoustic modem.

Another important point is that there is a match between real data (Figure 22a) and the prediction (Figure 22b) when the time difference between the first and the highest peaks is compared. Probably due to noise or some kind of scattering (in the water column or at the boundaries), no good match in the last portion of Figure 22 (a) and Figure 22 (b) can be found.

The final result depicted in Figure 23 shows that the horizontal distance estimated when the peaks are matched is 782.4 m, compared with the original rough estimate of 791.2 m. The range correction provided by the algorithm is 8.8 m, in this case.
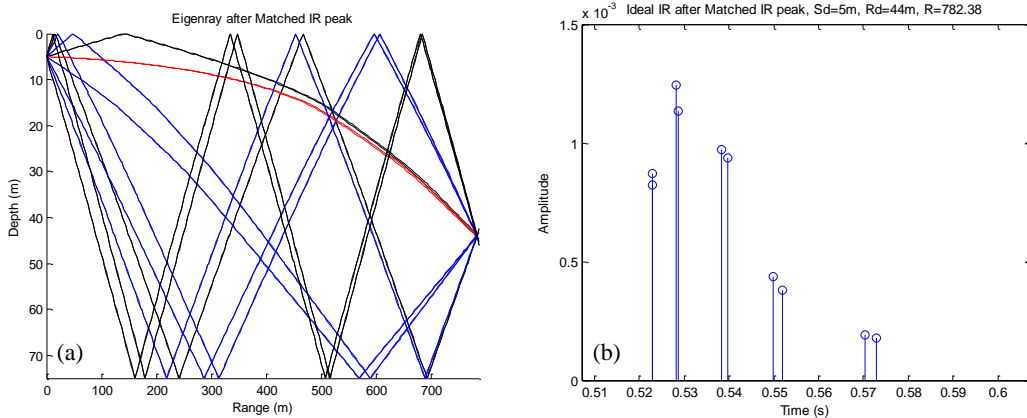
Figure 23.   (a) Eigenrays and (b) Ideal IR after Matched Peak IR Processing.
Data from Example 1

Example 2: Mission-2: 19:04:41 (hh:mm:ss) GMT

-   UUV depth: 1.5 m
-   Command ship transducer depth: 5 m
-   Measured one-way travel time (t_m): 323.6 ms
-   Slant range rough estimate (1500 x t_m): 485.4 m
-   Horizontal range rough estimate: 485.4 m

Figure 24 shows (a) the eigenray paths and (b) the amplitude and time of arrival associated with these rays. Note that the first group of arrivals (representing the direct

53

path and a surface bounce) has greater amplitude when compared with the second group of arrivals (representing a surface-and-bottom bounce and surface-bottom-and-surface bounce).
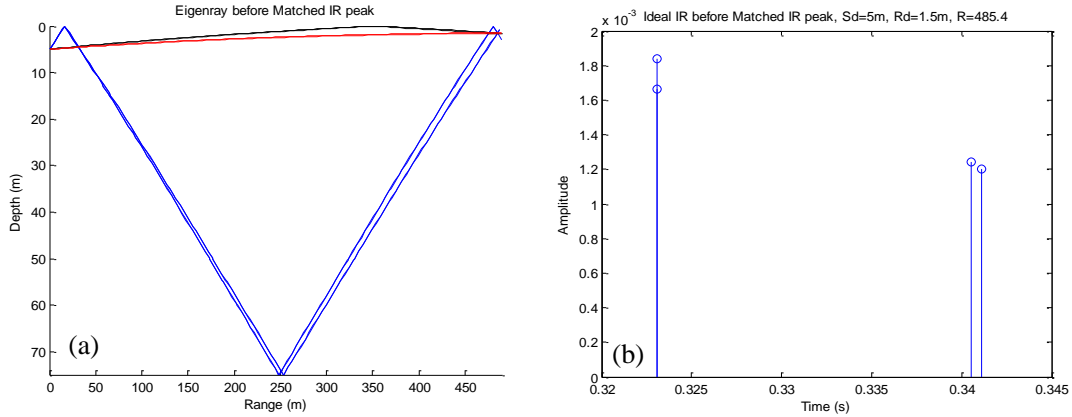
Figure 24.   (a) Eigenrays and (b) Ideal IR before Matched Peak IR Processing.
Data from Example 2

In this case, the attenuation and bottom losses associated with the longer path length are the major factors that cause the smaller amplitude in the second group of arrivals (Figure 24b). Another interesting point is the small time (and path length) difference between the direct path and the surface bounce in the first group of arrivals. Due to this small time difference, surface interference may play an important role in the result presented by the matched filter output.

As before, the time of the highest peak in Figure 25b matches with the one-way travel time measured by the acoustic modem, and there is a match between real data (Figure 25a) and the prediction (Figure 25b) when the time difference between the first and the highest peaks is compared. Again, probably due to noise and some kind of scattering, no match in the last portion of Figure 25 (a) and Figure 25 (b) can be found.
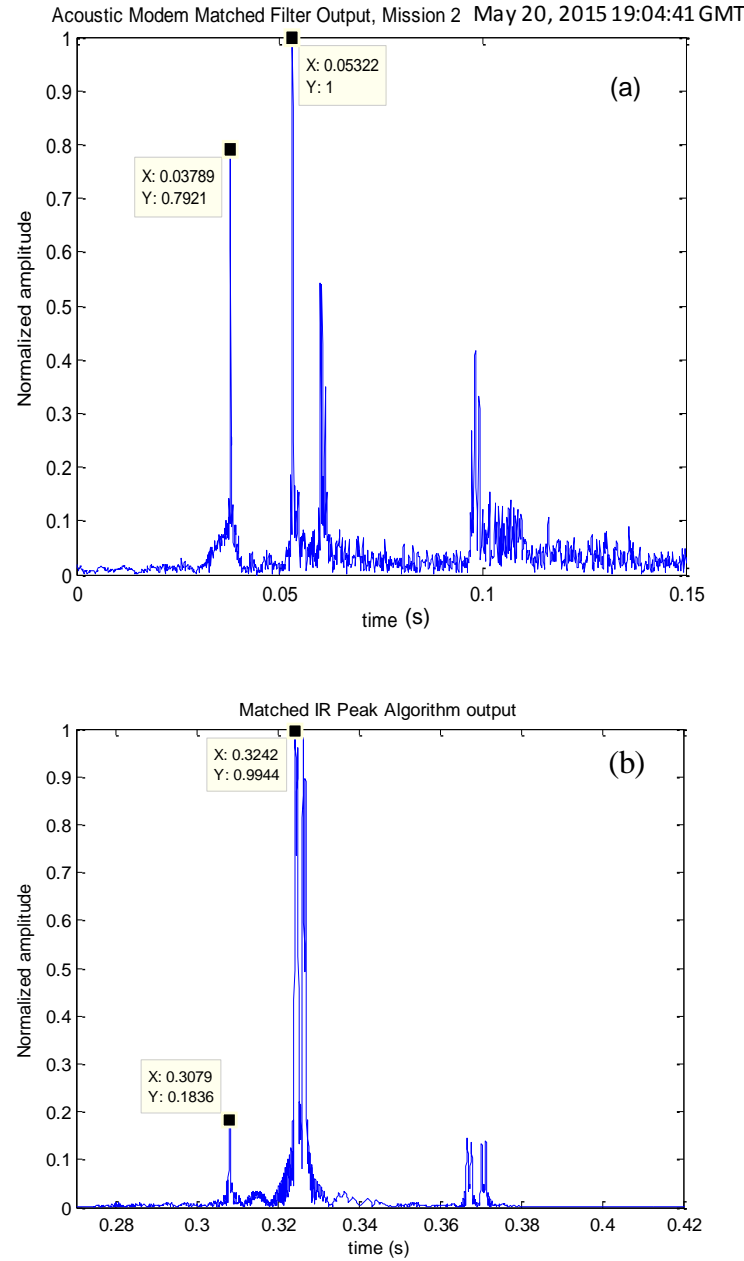
Figure 25.   Acoustic Modem (a) Matched Filter Output and
(b) Matched Peak IR Algorithm Output.
Data from Example 2

It is interesting to note the effect of surface interference in the first group of arrivals. Due to the small time difference, the surfaced reflected wave (180º out of phase)

almost completely cancels the direct wave contribution, causing a reduction in the matched filter output for the first peak (see Figure 25b).

The measured data shows similar behavior (Figure 25a) although, apparently, the reduction in the first peak was not as severe as predicted by the ray model. An attenuation in the second group of arrivals associated with the UUV and command ship transducer's beam patterns may be one contributing factor for this behavior; the beam patterns were considered omnidirectional in all calculations. Changes in the transducer's depth, due to wave motion, in both assets may also be a contributing factor, as could scattering of the surface reflected path. In this particular case, the UUV was at the surface in the "comms" position (i.e., with head tilted down and tail [the antenna] tilted up), which can be heavily affected by surface wave motion. The changing in depth, caused by the wave motion, may affect the amplitude of the arrivals.

The final result, depicted in Figure 26, shows that the horizontal distance estimated when the peaks are matched is 461.7 m, compared with the original rough estimate of 485.4 m. In this case, the range correction provided by the algorithm is 23.7 m.
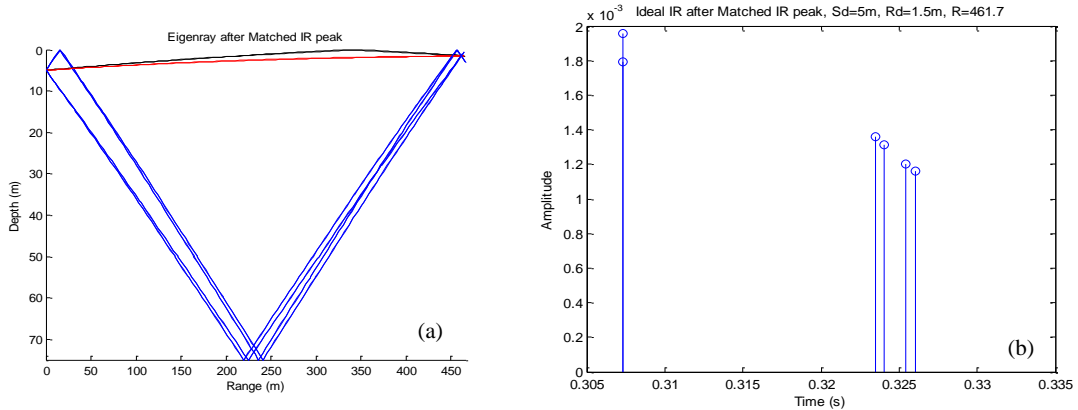
Figure 26.   (a) Eigenrays and (b) Ideal IR after Matched Peak IR Processing. Data from Example 2

Example 3: Mission-4: 20:41:06 (hh:mm:ss) GMT.

- UUV depth: 48.2 m
- Command ship transducer depth: 5 m
- Measured one-way travel time (t_m): 430 ms
- Slant range rough estimate (1500 x t_m): 645 m
- Horizontal range rough estimate: 643.6 m

Figure 27 shows (a) the eigenray paths and (b) the amplitude and time of arrival associated with these rays. Note that the first group of arrivals (representing the direct path and a surface bounce) has smaller amplitude when compared with the second group of arrivals (representing a bottom bounce and surface-and-bottom bounce). Again, this is due to the spreading of the ray tubes along their trajectories.
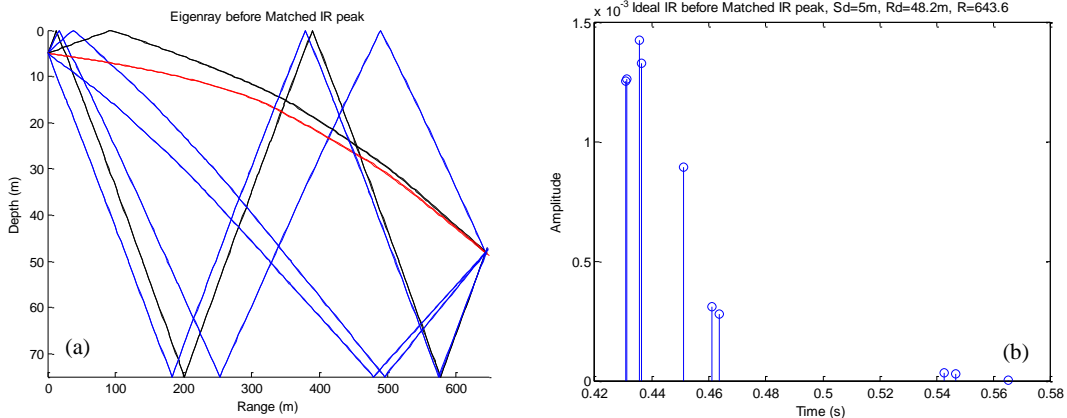
Figure 27.   (a) Eigenrays and (b) Ideal IR before Matched Peak IR Processing. Data from Example 3

As in the previous examples, the time of the highest peak in Figure 28b matches with the one-way travel time measured by the acoustic modem, and there is a match between real data (Figure 28a) and the prediction (Figure 28b) when the time difference between the first and second peaks is compared. Again, probably due to noise and some kind of scattering, it is hard to find a good match in the last portion of Figure 28 (a) and Figure 28 (b).
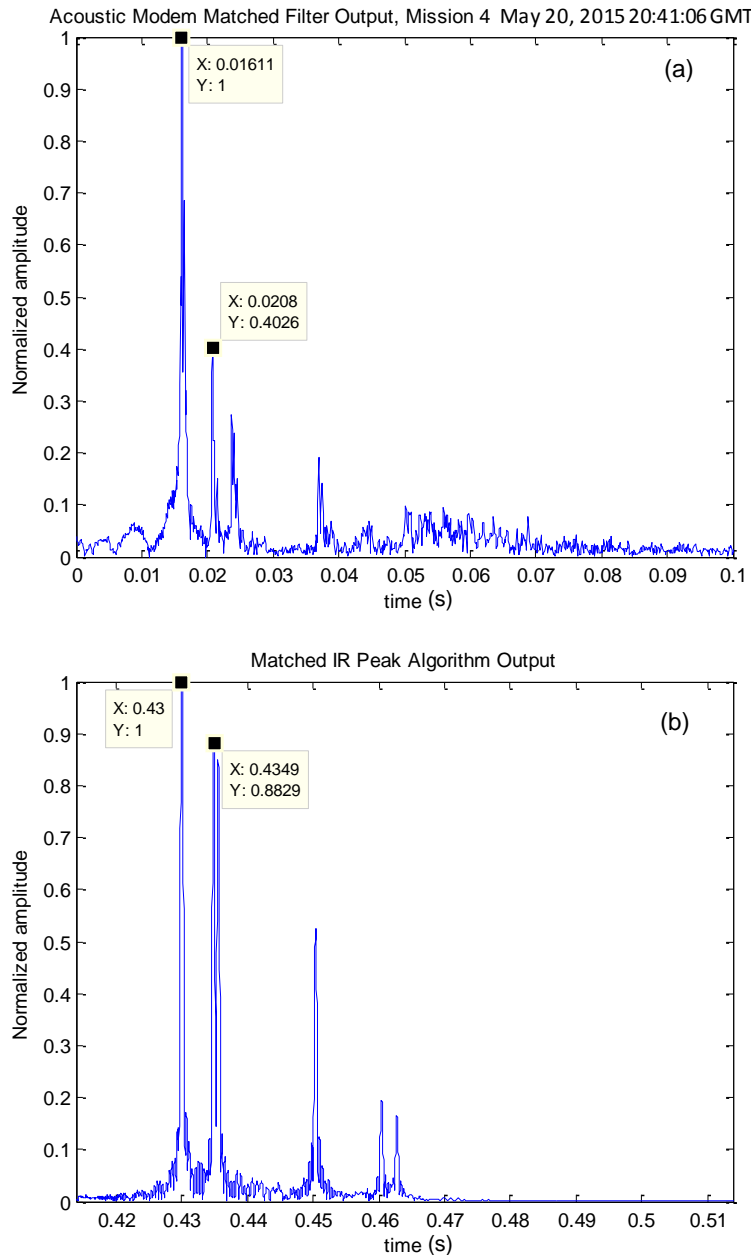
Figure 28.   Acoustic Modem (a) Matched Filter Output and
(b) Matched Peak IR Algorithm Output.
Data from Example 3

In Figure 27, the second group of arrivals (representing a bottom bounce and surface-and-bottom bounce) has higher amplitude than the first group of arrivals (representing the direct path and a surface bounce). However, Figure 28b indicates that

the interference between arrivals produced the opposite effect, and the first group of arrivals produces the highest IR peak. This effect was confirmed in the real data (Figure 28a).

Also observable in the Figure 28 plots is a mismatch of the amplitude difference between the first and second arrival groups in the real data compared with the prediction. This mismatch could be associated with the transducer beam patterns on the UUV and command ship, surface scattering, or unknown environmental effects.

The final result, depicted in Figure 29, shows that the horizontal distance estimated when the peaks are matched is 642.2 m, compared with the original rough estimate of 643.6 m. The range correction provided by the algorithm is only 1.4 m. This small difference simply accounts for the refraction of the sound waves (rays bending versus straight line propagation), since it is this first arrival that provides the highest peak in the matched filter output.
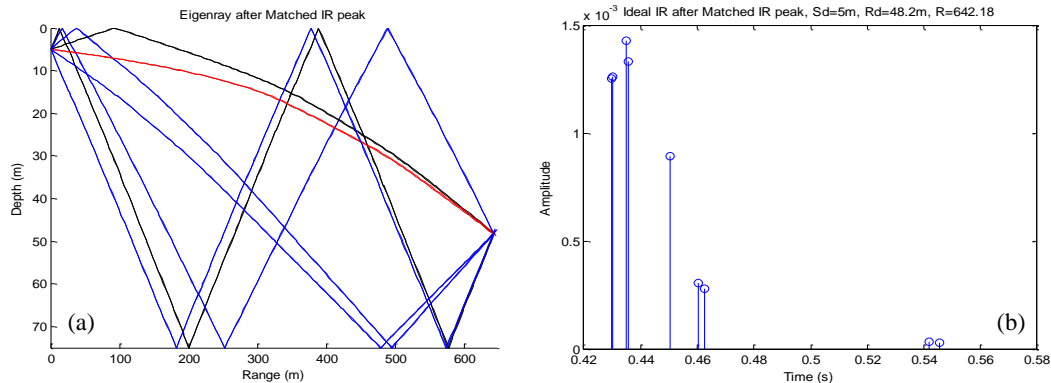
Figure 29.   (a) Eigenrays and (b) Ideal IR after Matched Peak IR Processing.
Data from Example 3

To claim any improvement associated with the method developed in this chapter, we use the horizontal distances estimated when the peaks are matched and roughly estimated as inputs for the tracking algorithm, as developed in Chapter V, and the results are compared in Chapter VII.

THIS PAGE INTENTIONALLY LEFT BLANK

V. THE TRACKING ALGORITHM

Parts of this chapter were previously published by IEEE [1].*

As defined in [38], "estimation is the process of inferring the value of a quantity of interest from indirect, inaccurate and uncertain observations," and "tracking is the estimation of the state of a moving object that can be done using one or more sensors at known locations." The Kalman filter, in all its variations, is one of the most widely used methods for tracking and estimation.

In this chapter, a tracking algorithm based on the KF is developed for a UUV. Due to non-linearities in the measurement equation two approaches are taken, first using the EKF and then using the UKF. The advantages and disadvantages of both approaches are highlighted. Additionally, tuning and smoothing algorithms are discussed and, as sea current is part of the UUV state representation, a consensus algorithm to take advantage of these predictions from different UUVs is developed.

A. KALMAN FILTER

The KF [39] can be seen as an optimal state estimator for discrete-time linear stochastic dynamic systems for which state space representation is given by Equations (2.13) and (2.14). KF is the optimal minimum mean square error estimator when all the noises entering the system (including the initial state error) are Gaussian. If these random variables are not Gaussian, KF is still the best (minimum error variance) linear state estimator [38].

KF is a recursive filter composed of two steps:

- – Prediction: the state of the system is predicted according to the state equation, given the previous updated state estimate;
- – Measurement update: prediction is updated given a measurement collected at this time step.

Derivations of the KF equations can be found in [9], [38] and are not presented in this dissertation.

a)   System model and initial assumptions

The state and measurement equations for a discrete-time linear stochastic dynamic system, as previously stated in Equations (2.13) and (2.14), are

$$\mathbf{x}(k+1) = \mathbf{F}(k)\mathbf{x}(k) + \mathbf{G}(k)\mathbf{u}(k) + \upsilon(k)$$
$$\mathbf{z}(k) = \mathbf{H}(k)\mathbf{x}(k) + \omega(k),$$

(5.1)

where, for simplicity, **D** in Equation (2.14) was set to zero, and **F**, **G**, **u,** and **H** are deterministic sequences assumed to be known for all k. The noises $\upsilon(k)$ and $\omega(k)$ are assumed to be zero mean, white (i.e., uncorrelated) Gaussian processes, such that

$$E\big[\upsilon(k)\big] = E\big[\omega(k)\big] = 0$$
$$E\big[\upsilon(k)\upsilon(j)^T\big] = \mathbf{Q}_k \delta_{k,j}$$
$$E\big[\omega(k)\omega(j)^T\big] = \mathbf{R}_k \delta_{k,j}$$
$$E\big[\upsilon(k)\omega(j)^T\big] = 0 \; \forall \, k, j \,.$$

(5.2)

At each step (k), the state estimate and error covariance matrix is determined by a sequence of well-defined prediction and measurement updates (also called correction), as follows:

b)   Prediction

$$\hat{\mathbf{x}}(k+1|k) = \mathbf{F}(k)\hat{\mathbf{x}}(k|k) + \mathbf{G}(k)\mathbf{u}(k)$$
$$\mathbf{P}(k+1|k) = \mathbf{F}(k)\mathbf{P}(k|k)\mathbf{F}(k)^T + \mathbf{Q}_k \,,$$

(5.3)

where $\hat{\mathbf{x}}(k|k)$ is the last updated state estimate and $\mathbf{P}(k|k)$ is the covariance matrix associated with this estimate.

c) Measurement update:

$$\mathbf{K}_{k+1} = \mathbf{P}(k+1|k)\mathbf{H}(k+1)^{T}\left[\mathbf{H}(k+1)\mathbf{P}(k+1|k)\mathbf{H}(k+1)^{T} + \mathbf{R}_{k+1}\right]^{-1}$$

$$\hat{\mathbf{x}}(k+1|k+1) = \hat{\mathbf{x}}(k+1|k) + \mathbf{K}_{k+1}\left[\mathbf{z}(k+1) - \mathbf{H}(k+1)\hat{\mathbf{x}}(k+1|k)\right] \qquad (5.4)$$

$$\mathbf{P}(k+1|k+1) = \left[\mathbf{I} - \mathbf{K}_{k+1}\mathbf{H}(k+1)\right]\mathbf{P}(k+1|k)\left[\mathbf{I} - \mathbf{K}_{k+1}\mathbf{H}(k+1)\right]^{T} + \mathbf{K}_{k+1}\mathbf{R}_{k+1}\mathbf{K}_{k+1}^{T},$$

where

- $\mathbf{K}_{k+1}$ is called the Kalman Gain matrix;
- $\hat{\mathbf{x}}(k+1|k+1)$ is the updated state and $\mathbf{P}(k+1|k+1)$ is the covariance matrix associated with the updated state;
- $\mathbf{z}(k+1)$ is the measurement. If no measurement is available at this step, just set $\hat{\mathbf{x}}(k+1|k+1) = \hat{\mathbf{x}}(k+1|k)$ and $\mathbf{P}(k+1|k+1) = \mathbf{P}(k+1|k)$, ignoring step (c).

B.   EXTENDED KALMAN FILTER

In many cases, dynamic systems are not linear by nature, which means that KF cannot be used for state estimation. In such situations, the state or the measurement equations can be non-linear. The most common approach makes use of Taylor series expansions to treat the non-linearities, giving origin to the EKF.

a) System model and initial assumptions:

The state and measurement equations for a discrete-time non-linear stochastic dynamic system, as previously stated in Equations (2.11) and (2.12), are

$$\mathbf{x}(k+1) = \mathbf{f}\left[\mathbf{x}(k)\right] + \upsilon(k)$$
$$\mathbf{z}(k) = \mathbf{h}\left[\mathbf{x}(k)\right] + \omega(k), \qquad (5.5)$$

where, for simplicity, $\mathbf{g}\left[\mathbf{u}(k)\right]$ in Equation (2.11) was set to zero assuming no deterministic inputs, and $\mathbf{f}\left[\mathbf{x}(k)\right]$ and $\mathbf{h}\left[\mathbf{x}(k)\right]$ are non-linear functions. The noises $\upsilon(k)$ and $\omega(k)$ are assumed to be zero mean, white (i.e., uncorrelated) Gaussian processes, as in Equation (5.2).

63

b) Taylor series expansion:

In the classical approach, the non-linear functions are expanded to the first order around the latest estimate (second order expansions can be found in [38]), as

$$
\mathbf{f}\left[\mathbf{x}(k)\right]=\mathbf{f}\left[\hat{\mathbf{x}}(k|k)\right]+\mathbf{F}_{k}\left[\mathbf{x}(k)-\hat{\mathbf{x}}(k|k)\right]
$$
$$
\mathbf{h}\left[\mathbf{x}(k)\right]=\mathbf{h}\left[\hat{\mathbf{x}}(k+1|k)\right]+\mathbf{H}_{k+1}\left[\mathbf{x}(k)-\hat{\mathbf{x}}(k+1|k)\right],
$$
(5.6)

where $\mathbf{F}_{k}=\dfrac{\partial\,\mathbf{f}\left[\mathbf{x}(k)\right]}{\partial\,\mathbf{x}(k)}\bigg|_{\mathbf{x}(k)=\hat{\mathbf{x}}(k|k)}$ and $\mathbf{H}_{k+1}=\dfrac{\partial\,\mathbf{h}\left[\mathbf{x}(k)\right]}{\partial\,\mathbf{x}(k)}\bigg|_{\mathbf{x}(k)=\hat{\mathbf{x}}(k+1|k)}$.

Substituting Equation (5.6) into Equation (5.5), we obtain

$$
\begin{aligned}
\mathbf{x}(k+1)&=\mathbf{f}\left[\hat{\mathbf{x}}(k|k)\right]+\mathbf{F}_{k}\left[\mathbf{x}(k)-\hat{\mathbf{x}}(k|k)\right]+\upsilon(k)\\
&=\mathbf{F}_{k}\mathbf{x}(k)+\mathbf{f}\left[\hat{\mathbf{x}}(k|k)\right]-\mathbf{F}_{k}\hat{\mathbf{x}}(k|k)+\upsilon(k)
\end{aligned}
$$
(5.7)

$$
\begin{aligned}
\mathbf{z}(k)&=\mathbf{h}\left[\hat{\mathbf{x}}(k+1|k)\right]+\mathbf{H}_{k+1}\left[\mathbf{x}(k)-\hat{\mathbf{x}}(k+1|k)\right]+\omega(k)\\
&=\mathbf{H}_{k+1}\mathbf{x}(k)+\mathbf{h}\left[\hat{\mathbf{x}}(k+1|k)\right]-\mathbf{H}_{k+1}\hat{\mathbf{x}}(k+1|k)+\omega(k).
\end{aligned}
$$
(5.8)

Hence, we have the linearized state and measurement equations

$$
\mathbf{x}(k+1)=\mathbf{F}_{k}\mathbf{x}(k)+\mathbf{v}(k)+\upsilon(k)
$$
$$
\mathbf{z}(k)=\mathbf{H}_{k+1}\mathbf{x}(k)+\mathbf{y}(k)+\omega(k),
$$
(5.9)

with deterministic terms

$$
\mathbf{v}(k)=\mathbf{f}\left[\hat{\mathbf{x}}(k|k)\right]-\mathbf{F}_{k}\hat{\mathbf{x}}(k|k)
$$
$$
\mathbf{y}(k)=\mathbf{h}\left[\hat{\mathbf{x}}(k+1|k)\right]-\mathbf{H}_{k+1}\hat{\mathbf{x}}(k+1|k).
$$
(5.10)

c) Prediction:

$$
\begin{aligned}
\hat{\mathbf{x}}(k+1|k)&=\mathbf{F}_{k}\hat{\mathbf{x}}(k|k)+\mathbf{v}(k)\\
&=\mathbf{F}_{k}\hat{\mathbf{x}}(k|k)+\mathbf{f}\left[\hat{\mathbf{x}}(k|k)\right]-\mathbf{F}_{k}\hat{\mathbf{x}}(k|k)\\
&=\mathbf{f}\left[\hat{\mathbf{x}}(k|k)\right]
\end{aligned}
$$
(5.11)

$$
\mathbf{P}(k+1|k)=\mathbf{F}_{k}\mathbf{P}(k|k)\mathbf{F}_{k}^{T}+\mathbf{Q}_{k}.
$$
(5.12)

d) Measurement update:

$$
\mathbf{K}_{k+1}=\mathbf{P}(k+1|k)\mathbf{H}_{k+1}^{T}\left[\mathbf{H}_{k+1}\mathbf{P}(k+1|k)\mathbf{H}_{k+1}^{T}+\mathbf{R}_{k+1}\right]^{-1}
$$
$$
\hat{\mathbf{x}}(k+1|k+1)=\hat{\mathbf{x}}(k+1|k)+\mathbf{K}_{k+1}\left[\mathbf{z}(k+1)-\mathbf{h}\left[\hat{\mathbf{x}}(k+1|k)\right]\right]
$$
$$
\mathbf{P}(k+1|k+1)=\left[\mathbf{I}-\mathbf{K}_{k+1}\mathbf{H}_{k+1}\right]\mathbf{P}(k+1|k)\left[\mathbf{I}-\mathbf{K}_{k+1}\mathbf{H}_{k+1}\right]^{T}+\mathbf{K}_{k+1}\mathbf{R}_{k+1}\mathbf{K}_{k+1}^{T},
$$
(5.13)

where $\mathbf{z}(k+1)$ is the measurement. If no measurement is available at this step, just set $\hat{\mathbf{x}}(k+1|k+1) = \hat{\mathbf{x}}(k+1|k)$ and $\mathbf{P}(k+1|k+1) = \mathbf{P}(k+1|k)$, ignoring step (d).

C.   UNSCENTED KALMAN FILTER

The UKF as seen in [40], [41], and [42] is a technique that utilizes the unscented transform (UT) [43], [44], and can be applied in models of the form of Equation (5.5). Instead of using linear approximations, as EKF requires, the idea of the UT is to deterministically choose a fixed number of *sigma points* that capture the mean (state) and covariance of the original distribution. These *sigma points* are then propagated through the non-linearity, and the mean and covariance of the transformed variable are estimated from them. According to [42], UT is able to capture higher order moments when compared with Taylor series based approximations.

Assuming the system model (state and measurement equations) and initial assumptions as in Equation (5.5), at each step (k), the general approach is along similar lines as the KF and the EKF, by prediction and measurement update as follows [45]:

a)   Prediction

 - Form sigma points:

$$\begin{aligned}
\boldsymbol{\chi}_k^{(0)} &= \hat{\mathbf{x}}(k|k), \\
\boldsymbol{\chi}_k^{(i)} &= \hat{\mathbf{x}}(k|k) + \sqrt{n+\lambda}\left[\sqrt{\mathbf{P}(k|k)}\right]_i, \\
\boldsymbol{\chi}_k^{(i+n)} &= \hat{\mathbf{x}}(k|k) - \sqrt{n+\lambda}\left[\sqrt{\mathbf{P}(k|k)}\right]_i, \quad i=1,...,n,
\end{aligned}$$ (5.14)

where the matrix square root denotes a matrix such that $\sqrt{\mathbf{P}}\sqrt{\mathbf{P}}^T = \mathbf{P}$, n is the length of the state, $[\cdot]_i$ denotes the ith column of the matrix, and λ is a scaling parameter defined as $\lambda = \alpha^2(n+\kappa)-n$. The parameters α and κ determine the spread of the sigma points around the mean.

- Propagate the sigma points through the state model:

$$\hat{\boldsymbol{\chi}}_k^{(i)} = \mathbf{f}\left(\boldsymbol{\chi}_k^{(i)}\right) \quad i=0,...,2n.$$ (5.15)

65

- Compute the predicted state and covariance:

$$\hat{\mathbf{x}}(k+1|k) = \sum_{i=0}^{2n} W_i^{(m)} \hat{\chi}_k^{(i)}$$

$$\mathbf{P}(k+1|k) = \sum_{i=0}^{2n} W_i^{(c)} \left(\hat{\chi}_k^{(i)} - \hat{\mathbf{x}}(k+1|k)\right)\left(\hat{\chi}_k^{(i)} - \hat{\mathbf{x}}(k+1|k)\right)^T + \mathbf{Q}_k \ , \tag{5.16}$$

where the weights $W_i^{(m)}$ and $W_i^{(c)}$ are defined as

$$W_0^{(m)} = \frac{\lambda}{n+\lambda},$$

$$W_0^{(c)} = \frac{\lambda}{n+\lambda} + \left(1 - \alpha^2 + \beta\right),$$

$$W_i^{(m)} = \frac{1}{2(n+\lambda)}, \quad i = 1,...,2n, \tag{5.17}$$

$$W_i^{(c)} = \frac{1}{2(n+\lambda)}, \quad i = 1,...,2n,$$

and β is a parameter that can be used to incorporate prior information on the (non-Gaussian) distribution of the state.

b)   Measurement update

- Form the sigma points:

$$\chi_{k+1}^{(0)} = \hat{\mathbf{x}}(k+1|k),$$

$$\chi_{k+1}^{(i)} = \hat{\mathbf{x}}(k+1|k) + \sqrt{n+\lambda}\left[\sqrt{\mathbf{P}(k+1|k)}\right]_i, \tag{5.18}$$

$$\chi_{k+1}^{(i+n)} = \hat{\mathbf{x}}(k+1|k) - \sqrt{n+\lambda}\left[\sqrt{\mathbf{P}(k+1|k)}\right]_i, \quad i = 1,...,n.$$

- Propagate the sigma points through the measurement model:

$$\hat{\mathbf{z}}_{k+1}^{(i)} = \mathbf{h}\left[k, \chi_{k+1}^{(i)}\right], \quad i = 0,...,2n. \tag{5.19}$$

- Compute the predicted measurement mean μ_k , covariance of the measurement S_k , and cross-covariance of the state and measurement, C_k :

$$\mu_{k+1} = \sum_{i=0}^{2n} W_i^{(m)} \hat{\mathbf{z}}_{k+1}^{(i)}$$

$$\mathbf{S}_{k+1} = \sum_{i=0}^{2n} W_i^{(c)} \left(\hat{\mathbf{z}}_{k+1}^{(i)} - \mu_{k+1}\right)\left(\hat{\mathbf{z}}_{k+1}^{(i)} - \mu_{k+1}\right)^T + \mathbf{R}_{k+1} \tag{5.20}$$

$$\mathbf{C}_{k+1} = \sum_{i=0}^{2n} W_i^{(c)} \left(\chi_{k+1}^{(i)} - \hat{\mathbf{x}}(k+1|k)\right)\left(\hat{\mathbf{z}}_{k+1}^{(i)} - \mu_{k+1}\right)^T.$$

- Compute the Kalman Gain and the updated state and covariance:

$$\mathbf{K}_{k+1} = \mathbf{C}_{k+1}\mathbf{S}_{k+1}^{-1}$$
$$\hat{\mathbf{x}}(k+1|k+1) = \hat{\mathbf{x}}(k+1|k) + \mathbf{K}_{k+1}\left(\mathbf{z}(k+1) - \boldsymbol{\mu}_{k+1}\right) \quad (5.21)$$
$$\mathbf{P}(k+1|k+1) = \mathbf{P}(k+1|k) - \mathbf{K}_{k+1}\mathbf{S}_{k+1}\mathbf{K}_{k+1}^{T},$$

where $\mathbf{z}(k+1)$ is the measurement. If no measurement is available at this step, just set

$\hat{\mathbf{x}}(k+1|k+1) = \hat{\mathbf{x}}(k+1|k)$ and $\mathbf{P}(k+1|k+1) = \mathbf{P}(k+1|k)$, ignoring step (b).

D.   KF-BASED TRACKING ALGORITHMS

For convenience and completeness, some equations in this section are repeated from Sections B and C of this chapter, and from Chapter II, Section B.3.

1.   EKF-Based UUV Tracking Algorithm

As demonstrated in Chapter II, the UUV state space representation is composed by a linear state equation and a non-linear measurement equation.

a)   System model and initial assumptions:

From Equation (2.28), the UUV state and measurement equations are

$$\mathbf{x}(k+1) = \mathbf{F}(k)\mathbf{x}(k) + \mathbf{G}(k)\mathbf{u}(k) + \upsilon(k)$$
$$z(k) = h\left[k, \mathbf{x}(k)\right] + \omega(k), \quad (5.22)$$

where

− The matrices $\mathbf{F}(k)$ and $\mathbf{G}(k)$ are deterministic and known for all k:

$$\mathbf{F}(k) = \begin{bmatrix} 1 & 0 & \Delta t(k) & 0 \\ 0 & 1 & 0 & \Delta t(k) \\ 0 & 0 & 1 & 0 \\ 0 & 0 & 0 & 1 \end{bmatrix}, \quad \mathbf{G}(k) = \begin{bmatrix} \Delta t(k) & 0 \\ 0 & \Delta t(k) \\ 0 & 0 \\ 0 & 0 \end{bmatrix};$$

− The input sequence $\mathbf{u}(k)$ is a deterministic and known for all k:

$$\mathbf{u}(k) = V(k)\cos(\phi(k)) \begin{bmatrix} \sin(\theta(k)) \\ \cos(\theta(k)) \end{bmatrix};$$

− $z(k) = r(k)^2 - x_r(k)^2 - y_r(k)^2$ is the measurement;

67

- $h[k, \mathbf{x}(k)] = x(k)^2 - 2x(k)x_r(k) - 2y(k)y_r(k) + y(k)^2$ is a non-linear function;
- The noises $\upsilon(k)$ and $\omega(k)$ are assumed to be zero mean, white (i.e., uncorrelated) Gaussian processes as in Equation (5.2).

In the measurement, $r(k)$ is the horizontal distance from the UUV to the reference point estimated according to Chapter IV (Section B.2.c). The coordinates of the reference point (longitude and latitude mapped to Cartesian coordinates) are $x_r(k)$ and $y_r(k)$.

   b)   Taylor series expansion

$$z(k) = \mathbf{H}_{k+1}\mathbf{x}(k) + y(k) + \omega(k)$$
$$y(k) = h[\hat{\mathbf{x}}(k+1|k)] - \mathbf{H}_{k+1}\hat{\mathbf{x}}(k+1|k),$$

(5.23)

where

$$\mathbf{H}_{k+1} = \frac{\partial\, h[\mathbf{x}(k)]}{\partial\, \mathbf{x}(k)}\bigg|_{\mathbf{x}(k)=\hat{\mathbf{x}}(k+1|k)}$$

$$= \left[\frac{\partial\, h[\mathbf{x}(k)]}{\partial x(k)}\quad \frac{\partial\, h[\mathbf{x}(k)]}{\partial y(k)}\quad \frac{\partial\, h[\mathbf{x}(k)]}{\partial c_x(k)}\quad \frac{\partial\, h[\mathbf{x}(k)]}{\partial c_y(k)}\right]\bigg|_{\mathbf{x}(k)=\hat{\mathbf{x}}(k+1|k)}$$

$$= \left[2x(k) - 2x_r(k)\quad 2y(k) - 2y_r(k)\quad 0\quad 0\right]\big|_{\mathbf{x}(k)=\hat{\mathbf{x}}(k+1|k)}$$

$$= \left[2\hat{x}(k+1|k) - 2x_r(k)\quad 2\hat{y}(k+1|k) - 2y_r(k)\quad 0\quad 0\right].$$

(5.24)

The final result in Equation (5.24) is also known as the Jacobian matrix.

   c)   Prediction

$$\hat{\mathbf{x}}(k+1|k) = \mathbf{F}(k)\hat{\mathbf{x}}(k|k) + \mathbf{G}(k)\mathbf{u}(k)$$
$$\mathbf{P}(k+1|k) = \mathbf{F}(k)\mathbf{P}(k|k)\mathbf{F}(k)^T + \mathbf{Q}_k,$$

(5.25)

where $\hat{\mathbf{x}}(k|k)$ is the last updated state estimate and $\mathbf{P}(k|k)$ is the 4x4 covariance matrix associated with this estimate. Modeling $\upsilon(k)$ as continuous white noise acceleration, according to [38], the covariance matrix $\mathbf{Q}_k$ takes the form

$$\mathbf{Q}(k) = \mathrm{cov}(\upsilon(k)) = q^2\begin{bmatrix} \Delta t(k)^3/3 & \Delta t(k)^2/2 & 0 & 0 \\ \Delta t(k)^3/3 & \Delta t(k)^2/2 & 0 & 0 \\ 0 & 0 & \Delta t(k)^2/2 & \Delta t(k) \\ 0 & 0 & \Delta t(k)^2/2 & \Delta t(k) \end{bmatrix},$$

(5.26)

where q is the tuning parameter and Δt is the sampling time.

d)   Measurement update

$$z(k+1) = r(k+1)^2 - x_r(k+1)^2 - y_r(k+1)^2$$
$$\mathbf{K}_{k+1} = \mathbf{P}(k+1|k)\mathbf{H}_{k+1}{}^T\left[\mathbf{H}_{k+1}\mathbf{P}(k+1|k)\mathbf{H}_{k+1}{}^T + \mathbf{R}_{k+1}\right]^{-1}$$
$$\hat{\mathbf{x}}(k+1|k+1) = \hat{\mathbf{x}}(k+1|k) + \mathbf{K}_{k+1}\left[z(k+1) - \mathbf{h}\left[\hat{\mathbf{x}}(k+1|k)\right]\right] \qquad (5.27)$$
$$\mathbf{P}(k+1|k+1) = \left[\mathbf{I} - \mathbf{K}_{k+1}\mathbf{H}_{k+1}\right]\mathbf{P}(k+1|k)\left[\mathbf{I} - \mathbf{K}_{k+1}\mathbf{H}_{k+1}\right]^T + \mathbf{K}_{k+1}\mathbf{R}_{k+1}\mathbf{K}_{k+1}{}^T,$$

where $\mathbf{z}(k+1)$ is the measurement. If no measurement is available at this step, just set

$\hat{\mathbf{x}}(k+1|k+1) = \hat{\mathbf{x}}(k+1|k)$ and $\mathbf{P}(k+1|k+1) = \mathbf{P}(k+1|k)$, ignoring step (d).

2.   UKF-Based UUV Tracking Algorithm

Assuming the system model and initial assumptions as in Equation (5.22), at each step (k) the following operations are performed [45]:

a)   Prediction

 - Form sigma points:

$$\boldsymbol{\chi}_k^{(0)} = \hat{\mathbf{x}}(k|k),$$
$$\boldsymbol{\chi}_k^{(i)} = \hat{\mathbf{x}}(k|k) + \sqrt{n+\lambda}\left[\sqrt{\mathbf{P}(k|k)}\right]_i, \qquad (5.28)$$
$$\boldsymbol{\chi}_k^{(i+n)} = \hat{\mathbf{x}}(k|k) - \sqrt{n+\lambda}\left[\sqrt{\mathbf{P}(k|k)}\right]_i, \qquad i = 1,...,n,$$

where the matrix square root denotes a matrix such that $\sqrt{\mathbf{P}}\sqrt{\mathbf{P}}^T = \mathbf{P}$, n is the length of the state, $[\cdot]_i$ denotes the ith column of the matrix, and λ is a scaling parameter defined as $\lambda = \alpha^2(n+\kappa) - n$. The parameters α and κ determine the spread of the sigma points around the mean. The vector $\hat{\mathbf{x}}(k|k)$ is the last updated state estimate and $\mathbf{P}(k|k)$ is the 4x4 covariance matrix associated with this estimate.

 - Propagate the sigma points through the state model:

$$\hat{\boldsymbol{\chi}}_k^{(i)} = \mathbf{F}(k)\boldsymbol{\chi}_k^{(i)} + \mathbf{G}(k)\mathbf{u}(k), \quad i = 0,...,2n, \qquad (5.29)$$

where $\mathbf{F}(k)$, $\mathbf{G}(k)$, and $\mathbf{u}(k)$ are defined in Equation (5.22).

- Compute the predicted state and covariance:

$$\hat{\mathbf{x}}(k+1|k) = \sum_{i=0}^{2n} W_i^{(m)} \hat{\boldsymbol{\chi}}_k^{(i)}$$

$$\mathbf{P}(k+1|k) = \sum_{i=0}^{2n} W_i^{(c)} \left(\hat{\boldsymbol{\chi}}_k^{(i)} - \hat{\mathbf{x}}(k+1|k)\right)\left(\hat{\boldsymbol{\chi}}_k^{(i)} - \hat{\mathbf{x}}(k+1|k)\right)^T + \mathbf{Q}_k,$$

(5.30)

where the matrix $\mathbf{Q}_k$ is defined in Equation (5.26), and the weights $W_i^{(m)}$ and $W_i^{(c)}$ are defined as

$$W_0^{(m)} = \frac{\lambda}{n+\lambda},$$

$$W_0^{(c)} = \frac{\lambda}{n+\lambda} + \left(1 - \alpha^2 + \beta\right),$$

$$W_i^{(m)} = \frac{1}{2(n+\lambda)}, \quad i = 1,\dots,2n,$$

$$W_i^{(c)} = \frac{1}{2(n+\lambda)}, \quad i = 1,\dots,2n,$$

(5.31)

and β is a parameter that can be used to incorporate prior information on the (non-Gaussian) distribution of the state.

b)   Measurement update

- Form the sigma points:

$$\boldsymbol{\chi}_{k+1}^{(0)} = \hat{\mathbf{x}}(k+1|k),$$

$$\boldsymbol{\chi}_{k+1}^{(i)} = \hat{\mathbf{x}}(k+1|k) + \sqrt{n+\lambda}\left[\sqrt{\mathbf{P}(k+1|k)}\right]_i,$$

(5.32)

$$\boldsymbol{\chi}_{k+1}^{(i+n)} = \hat{\mathbf{x}}(k+1|k) - \sqrt{n+\lambda}\left[\sqrt{\mathbf{P}(k+1|k)}\right]_i, \quad i = 1,\dots,n.$$

- Propagate the sigma points through the measurement model:

$$\hat{z}_{k+1}^{(i)} = h\left[k, \boldsymbol{\chi}_{k+1}^{(i)}\right], \quad i = 0,\dots,2n,$$

(5.33)

where $h\left[k, \boldsymbol{\chi}_{k+1}^{(i)}\right] = x^{(i)}(k)^2 - 2x^{(i)}(k)x_r(k) - 2y^{(i)}(k)y_r(k) + y^{(i)}(k)^2$, $x^{(i)}$ is the position in x of the ith sigma point and $y^{(i)}$ is the position in y of the ith sigma point.

- Compute the predicted measurement mean μ_k, covariance of the measurement S_k, and cross-covariance of the state and measurement, C_k:

$$\mu_{k+1} = \sum_{i=0}^{2n} W_i^{(m)} \hat{z}_{k+1}^{(i)}$$

$$S_{k+1} = \sum_{i=0}^{2n} W_i^{(c)} \left(\hat{z}_{k+1}^{(i)} - \mu_{k+1}\right)\left(\hat{z}_{k+1}^{(i)} - \mu_{k+1}\right)^T + R_{k+1} \qquad (5.34)$$

$$C_{k+1} = \sum_{i=0}^{2n} W_i^{(c)} \left(\chi_{k+1}^{(i)} - \hat{x}(k+1|k)\right)\left(\hat{z}_{k+1}^{(i)} - \mu_{k+1}\right)^T.$$

- Compute the Kalman Gain and the updated state and covariance:

$$z(k+1) = r(k+1)^2 - x_r\left(k+1\right)^2 - y_r\left(k+1\right)^2$$

$$\mathbf{K}_{k+1} = \mathbf{C}_{k+1}S_{k+1}^{-1}$$

$$\hat{\mathbf{x}}\left(k+1|k+1\right) = \hat{\mathbf{x}}\left(k+1|k\right) + \mathbf{K}_{k+1}\left(z\left(k+1\right) - \mu_{k+1}\right) \qquad (5.35)$$

$$\mathbf{P}\left(k+1|k+1\right) = \mathbf{P}\left(k+1|k\right) - \mathbf{K}_{k+1}S_{k+1}\mathbf{K}_{k+1}^T,$$

where $z(k+1)$ is the measurement. If no measurement is available at this step, just set $\hat{\mathbf{x}}\left(k+1|k+1\right) = \hat{\mathbf{x}}\left(k+1|k\right)$ and $\mathbf{P}\left(k+1|k+1\right) = \mathbf{P}\left(k+1|k\right)$, ignoring step (b).

E.   GENERAL OBSERVATIONS

In this section, the advantages and disadvantages of using EKF and UKF are highlighted, and an alternative model considering non-additive Gaussian noise is briefly discussed.

1.   EKF and UKF Comparison

As seen in Section B, EKF makes use of Taylor series expansions to treat the non-linearities in the state space model. This approach introduces limitations in the use of this technique. First, the non-linearities need to be differentiable and second, higher order moments are not considered in the Taylor series expansion.

As presented in Section C, instead of linear approximations, UKF makes use of deterministically chosen *sigma points* to capture the true mean and covariance of the states. Those points are then propagated through the non-linearities, and the mean (predicted state) and covariance are estimated from them. This process is also called statistical linearization.

Advantages of the UKF in comparison with EKF are:

- Non-linearities do not need to be differentiable nor do their Jacobian matrices need to be calculated;

- UKF can capture higher order moments better than EKF [42].

Despite these advantages, UKF requires more computing efforts due to the generation and propagation of the *sigma points*. The number of sigma points (*N*) is a function of the size of the state (*n*), $N = 2n+1$, and depending on the size of the state, the computational load can represent a limiting factor.

2. Non-additive Gaussian Noise

A different model considering non-additive Gaussian noise in the measurement equation can be used, and for this approach the UUV state space representation becomes

$$\mathbf{x}(k+1) = \mathbf{F}(k)\mathbf{x}(k) + \mathbf{G}(k)\mathbf{u}(k) + \upsilon(k)$$
$$z(k) = h\big[k, \mathbf{x}(k), \omega(k)\big].$$

(5.36)

The differences in the presented EKF and UKF algorithms in comparison with this case are small and, to avoid repetition, are not be presented in this dissertation. However, they can be found in [45].

F. TUNING

The performance of KF-based algorithms is heavily dependent on the tuning parameters. These parameters are often set manually at great cost of engineering time leading to, generally, non-optimum choices.

In KF and EKF the tuning parameters are the covariance matrices of the measurement and plant noises (**R** and **Q**) only. The UKF requires, additionally, the tuning of three scalar parameters (α, β, and κ) also known as hyper-parameters.

The hyper-parameters α and κ are related with the spreading of the sigma points, and the hyper-parameter β is related to the distribution of the filtered states. Some heuristics to choose these tuning parameters have been proposed [40], [41], but there is no consensus regarding such methods. An increasing number of authors have

proposed the use of optimization techniques (or optimizers) to select the hyper-parameters [46], [47], [48], or the covariance matrices of the noises.

In this approach, the KF-based algorithm is used to construct the objective function (or cost function) $f(\mathbf{x})$ where, for the most comprehensive case (UKF), $\mathbf{x} = [\alpha, \beta, \kappa, \mathbf{R}, \mathbf{Q}]$ is subjected to the feasible set Ω such that $\mathbf{x} \in \Omega$. The optimization technique will find the best vector $\mathbf{x}$ over all possibilities in Ω that minimizes or maximizes the objective function.

The objective function is not unique, and in some circumstances, the choice of the most suitable objective function can be very challenging. The existence of discontinuities and multiple local extrema on the objective function may be a problem for the optimizer.

Using the tracking data of the KF-based algorithm, it is possible to define the following objective functions:

a)   Residual measurement error

Represents the quadratic measurement error weighted by the associated covariance matrix. It is used when the set of measurements is reliable. The optimization technique should find a vector that minimizes the objective function

$$ f(\mathbf{x}) = \sum_{k=1}^{N} \left(z_k - h(\hat{x}_{k|k}) \right) S_k \left(z_k - h(\hat{x}_{k|k}) \right)^T, \tag{5.37} $$

where z_k is the measurement at discrete time k, S_k is the covariance matrix associated with this measurement, $h(\hat{x}_{k|k})$ is the nonlinear measurement equation evaluated for the updated state $\hat{x}_{k|k}$, and N is the number of measurements available.

b)   Residual prediction error

Represents the quadratic prediction error weighted by the associated covariance matrix. It is used when "ground truth" data is available. The optimization technique should find a vector that minimizes the objective function

$$ f(\mathbf{x}) = \sum_{k=1}^{N} \left(\mathbf{x}_k - \hat{\mathbf{x}}_{k|k} \right) \mathbf{P}_k \left(\mathbf{x}_k - \hat{\mathbf{x}}_{k|k} \right)^T, \tag{5.38} $$

where $\mathbf{x}_k$ is the true state at discrete time k, $\hat{\mathbf{x}}_{k|k}$ is the updated predicted state at discrete time k, $\mathbf{P}_k$ is the covariance matrix associated with this state, and N is the number of states available.

c) Log-likelihood of the measurements:

Used in Gaussian processes when the set of measurements is reliable. The optimization technique should find a vector that maximizes the objective function [49]

$$f(\mathbf{x}) = \ln p(z_{1:N}|\mathbf{x}) = \sum_{k=1}^{N}\left[-\frac{1}{2}z_k^T S_k^{-1} z_k - \frac{1}{2}\ln|S_k| - \frac{N}{2}\ln 2\pi\right], \qquad (5.39)$$

where z_k is the measurement at discrete time k, S_k is the covariance matrix associated with this measurement, and N is the number of measurements available.

d) Log-likelihood of the states

Used in Gaussian processes when "ground truth" data is available. The optimization technique should find a vector that maximizes the objective function [49]

$$f(\mathbf{x}) = \ln p(\mathbf{x}_{1:N}|\mathbf{x}) = \sum_{k=1}^{N}\left[-\frac{1}{2}\mathbf{x}_k^T \mathbf{P}_k^{-1} \mathbf{x}_k - \frac{1}{2}\ln|\mathbf{P}_k| - \frac{N}{2}\ln 2\pi\right], \qquad (5.40)$$

where $\mathbf{x}_k$ is the true state at discrete time k, $\mathbf{P}_k$ is the covariance matrix associated with the predicted state $\hat{\mathbf{x}}_{k|k}$, and N is the number of states available.

In all the preceding objective functions, the input data of the KF-based algorithm is used as training data. The quality of the resulting tuning will depend on how well the training data represents the situations that the filter could encounter in real applications. Ideally, an ample set of training data, representing different conditions (ambient noise, sea state, relative positioning between assets, etc.) should be available to select the tuning parameters. In environments where the conditions during the mission are expected to change significantly, the tuning would probably have to be redone. In this case, different sets of tuning parameters could be stored in the UUV and used accordingly.

The selection of the optimal tuning parameters, for a given training data, involves several runs of the KF-based algorithm (UKF or EKF) and it can take time to converge. As seen in Figure 30, the process starts by initializing the tuning parameters. The UKF

then runs and the cost function is calculated. To be able to find the cost function's extrema (minimum or maximum), the optimizer will run UKF and calculate the cost function for several different tuning parameters. Different techniques can be used to find the extrema and most popular solvers make use of variational calculus algorithms, as in MATLAB fmicon (constrained nonlinear minimization), or artificial intelligence techniques, as in the genetic algorithms or simulated annealing algorithms.
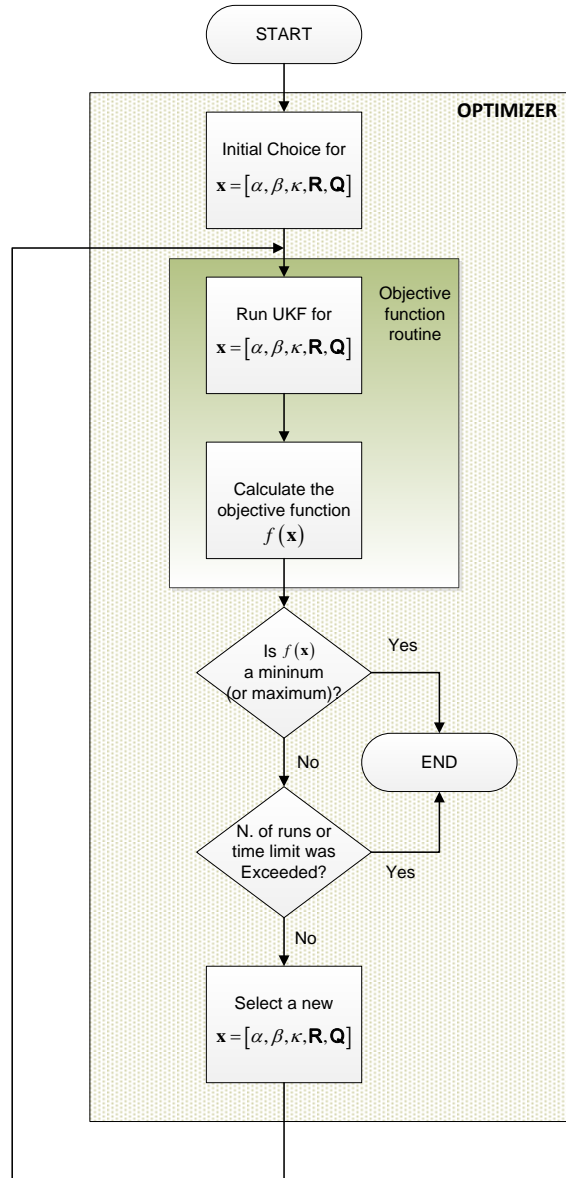
Figure 30.   Tuning Flow Chart for UKF

75

G. SMOOTHING

Smoothing is a non-real-time processing that uses all measurements between t_1 and t_2 to estimate the state of a system at certain time t, where $t_1 \leq t \leq t_2$ [9]. It is particulary useful to provide realistic trajectories during the transient portions of the tracking and in situations where few measurements are available.

Smoothing requires a backward iteration after the forward filtering has been performed resulting in $\hat{\mathbf{x}}(k|k)$, $\hat{\mathbf{x}}(k+1|k)$, $\mathbf{P}(k|k)$, and $\mathbf{P}(k+1|k)$ that should be stored [38]. The smoothing algorithm presented in this section is known as the KF fixed interval smoother or Rauch-Tung-Striebel smoother.

Considering KF and EKF, for all k from $k=N-1$ until $k=0$ (N is number of samples) the following operations must be performed [9]:

a)   Smoother gain calculation

$$\mathbf{D}(k) = \mathbf{P}(k|k)\mathbf{F}(k)^T \mathbf{P}(k+1|k)^{-1} .\tag{5.41}$$

b)   Smoothed state and covariance

$$\hat{\mathbf{x}}(k|N) = \hat{\mathbf{x}}(k|k) + \mathbf{D}(k)\left[\hat{\mathbf{x}}(k+1|N) - \hat{\mathbf{x}}(k+1|k)\right]$$
$$\mathbf{P}(k|N) = \mathbf{P}(k|k) + \mathbf{D}(k)\left[\mathbf{P}(k+1|N) - \mathbf{P}(k+1|k)\right]\mathbf{D}(k)^T .\tag{5.42}$$

For UKF additionally, during the forward filtering, the cross-covariance $\mathbf{C}_{k+1}$ must be stored resulting in the following operations from $k=N-1$ until $k=0$ [45]:

a)   Smoother gain calculation

$$\mathbf{D}(k) = \mathbf{C}_{k+1}\mathbf{P}(k+1|k)^{-1} .\tag{5.43}$$

b)   Smoothed state and covariance

$$\hat{\mathbf{x}}(k|N) = \hat{\mathbf{x}}(k|k) + \mathbf{D}(k)\left[\hat{\mathbf{x}}(k+1|N) - \hat{\mathbf{x}}(k+1|k)\right]$$
$$\mathbf{P}(k|N) = \mathbf{P}(k|k) + \mathbf{D}(k)\left[\mathbf{P}(k+1|N) - \mathbf{P}(k+1|k)\right]\mathbf{D}(k)^T .\tag{5.44}$$

H. CONSENSUS CURRENT ALGORITHM

As shown in Chapter II, as part of the UUV tracking model, the drift caused by the sea current was modeled as a random walk and is part of the state of the system.

Predictions for the sea current from different UUVs may be transmitted via the reference point at the surface to a command ship or shore-based command center for further processing. The purpose of this section is to develop a consensus algorithm able to take advantage of this information.

In the classical problem of consensus, a group of agents need to agree (or a solution needs to converge) upon a certain quantity of interest [50]. It is important to consider that some of the agents may have access to better information than others. In this situation, the consensus algorithm needs to be biased in favor of those with more reliable information [51].

There are basically three types of networks in consensus problems:

1.   In a centralized network, the agents involved only have the ability to communicate with a centralized location;

2.   In a decentralized network, the agents involved only have the ability to communicate with each other;

3.   In a mixed network, the agents have the ability to communicate with a centralized location and with each other.

Let us expand the scenario described in Chapter II (depicted in Figure 1) for a multi-agent (multiple UUVs) centralized network where the assets at the surface can share information collected from the UUVs with a shore-based command center. After a certain time underwater, the UUVs are able to update their position without going to the surface by running the KF-based algorithm. During this process, when a measurement to a surface asset is taken, the UUV may transmit its prediction for the sea current and associated uncertainty.

This information is then transmitted, by the surface asset, to the shore command center using satellite communication. The command center will receive the information about the sea current coming from different UUVs at different times and will need to solve a recursive problem to find the consensus sea current (see Figure 31).
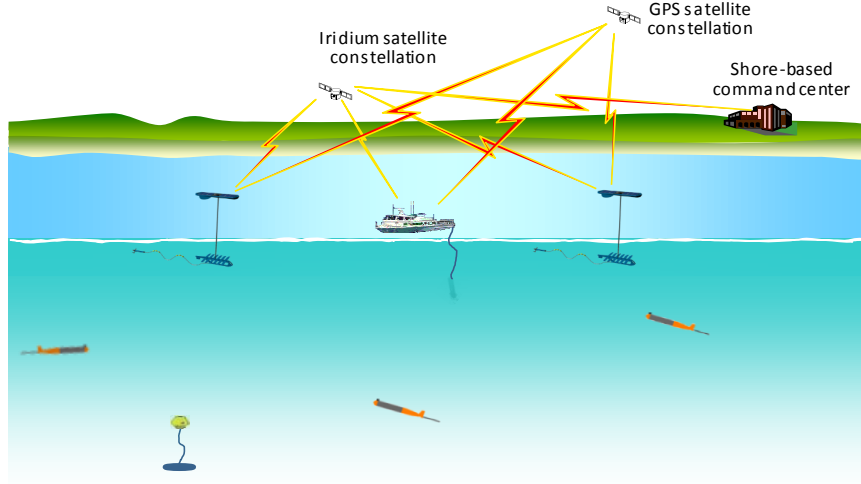
Figure 31.   Centralized Multi-agent Network

The tracking algorithm, running in the UUVs, is able to make predictions for sea current in x and y directions, as well as predict the associated covariance. We can select part of the state and covariance related with the sea current to form the following quantities

$$\mathbf{c} = \begin{bmatrix} c_x & c_y \end{bmatrix}, \quad \mathbf{P_c} = \begin{bmatrix} \sigma_x^2 & \sigma_{xy} \\ \sigma_{yx} & \sigma_y^2 \end{bmatrix}, \tag{5.45}$$

where

-    $\mathbf{c}$ is the sea current vector and $\mathbf{P_c}$ is the associated covariance matrix;

-    σ_x^2 is the covariance in x, σ_y^2 is the covariance in y, and $\sigma_{xy} = \sigma_{yx}$ is the cross-covariance.

Note that the covariance matrix is symmetric. An important property of symmetric matrices is that the eigenvalues (λ) are real and the eigenvectors (Ψ) are orthogonal to each other [52]. Eigenvalues and eigenvectors of a covariance matrix may be geometrically interpreted as

-    Eigenvectors are orthogonal unit vectors that represent the axis of a confidence ellipse for which the center is the mean (c);

-    Eigenvalues are real numbers representing the length of the ellipse axes (see Equation (5.46) and Figure 32).

78

$$\mathbf{P_c}\Psi = \Psi\lambda$$

$$\Rightarrow \lambda = \begin{bmatrix} e & 0 \\ 0 & f \end{bmatrix}; \quad \Psi = \begin{bmatrix} \cos\theta & -\sin\theta \\ \sin\theta & \cos\theta \end{bmatrix}. \tag{5.46}$$
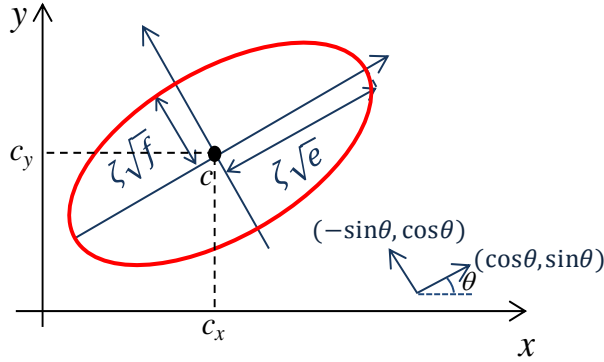
ζ is a scaling factor to attribute a certain percentage to the confidence ellipse, for example, for a 95% confidence ellipse (considering normally distributed data) $\zeta = \sqrt{5.991}$.

Figure 32.   Ellipse Representing a Confidence Interval around the Mean c
According to Equation (5.46)

We can say that the eigenvector associated with the smaller eigenvalue points to the direction with smaller variation around the mean (or points to a more reliable region). From Equation (5.46) and Figure 32, the eigenvector associated with the smaller eigenvalue is

$$\mathbf{H} = \begin{bmatrix} -\sin\theta \\ \cos\theta \end{bmatrix}. \tag{5.47}$$

The eigenvector $\mathbf{H}$ may be used to reduce the amount of data transmitted by the UUV, while still carrying information about the uncertainty associated with the prediction for the sea current. This may be done by writing

$$y = \mathbf{cH} = \begin{bmatrix} c_x & c_y \end{bmatrix} \begin{bmatrix} -\sin\theta \\ \cos\theta \end{bmatrix}. \tag{5.48}$$

The UUV may now transmit only two real numbers (the angle θ and the quantity y) instead of five real numbers as in Equation (5.45). The command center will receive y and H from different UUVs at different times and have to solve recursively for $c(k)$, using the relationship

79

$$y(k) = \mathbf{c}(k)\mathbf{H}(k). \tag{5.49}$$

Equation (5.49) may be thought of as being a measurement and the following state space representation may be used

$$\mathbf{c}(k+1) = \mathbf{F}(k)\mathbf{c}(k) + \upsilon(k)$$
$$\mathbf{y}(k) = \mathbf{H}(k)\mathbf{c}(k) + \omega(k), \tag{5.50}$$

where $\mathbf{F}(k)$ is the identity matrix and the noises $\upsilon(k)$ and $\omega(k)$ are assumed to be zero mean, white (i.e., uncorrelated) Gaussian processes.

The sea current $\mathbf{c}(k)$ in Equation (5.50) may be solved using the Kalman equations as shown in Section A. When the predictions for the current converge to a steady-state value, we have the consensus sea current (CSC). Uses for the CSC may be as follows:

- the command center can use CSC in its upper level tracking algorithm;
- CSC can be broadcasted to all UUVs to be used in their tracking algorithms;
- CSC can help to decide if two UUVs have reliable position to take distance measurements from each other (CSC amplitude and time of the last position update could be the criteria);

A complete view of the consensus algorithm is shown in Figure 33.
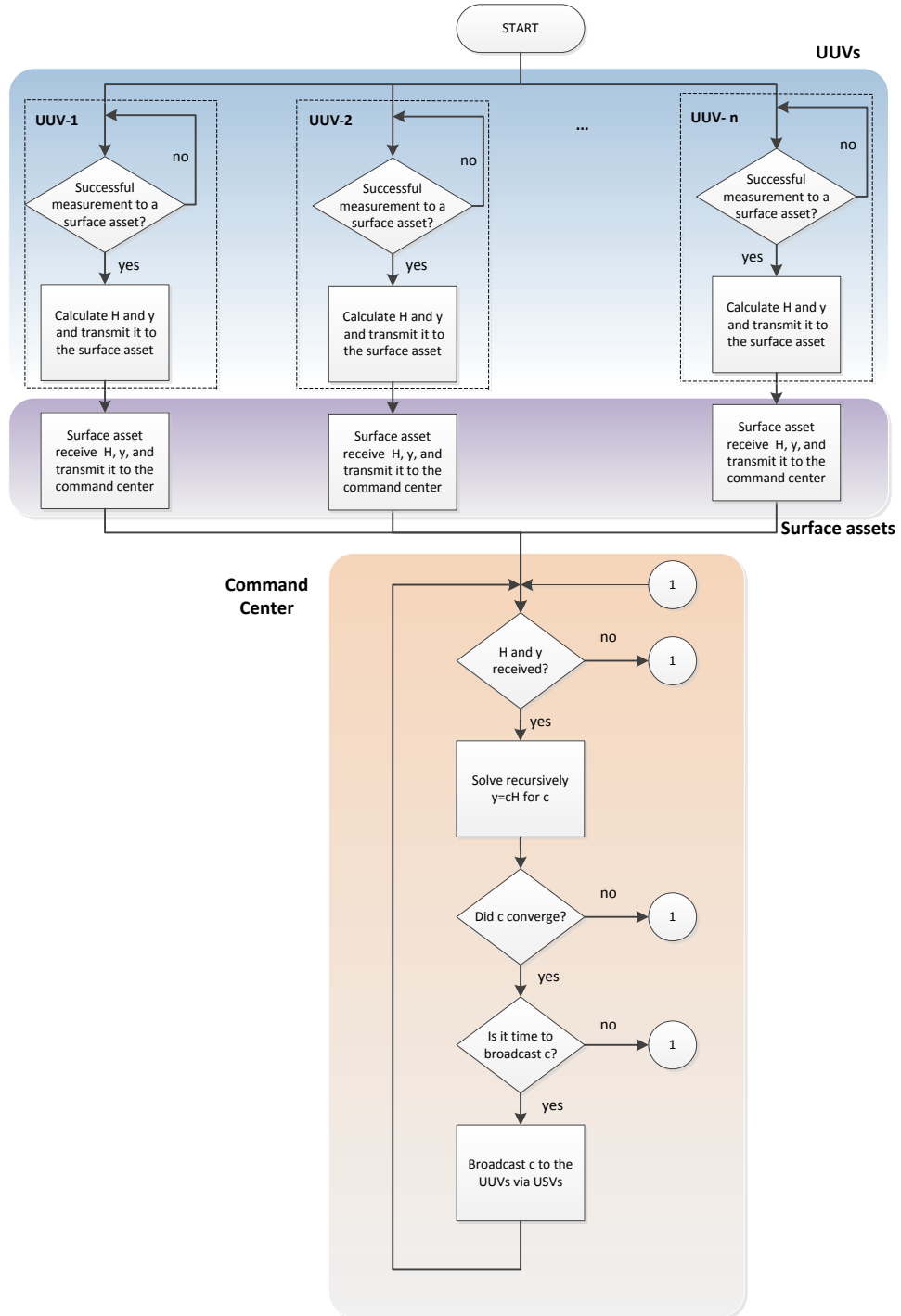
Figure 33.   Consensus Current Algorithm

81

THIS PAGE INTENTIONALLY LEFT BLANK

VI. SIMULATIONS

In this chapter, the algorithms developed in Chapter V are tested considering three distinct cases. The first is the ideal case where all the measurements are successful and no noise is present. The second case considers failure in the measurements during a certain portion of the UUVs mission. In the third, noise is added to the previous case.

A scenario in which two UUVs navigating in an area where three surface assets are present is simulated. The surface assets, represented by Wave Gliders (WG) in Figure 34, have access to GPS and can share information with the shore-based command center via satellite as in a centralized multi-agent network, permitting evaluation of the consensus current algorithm.
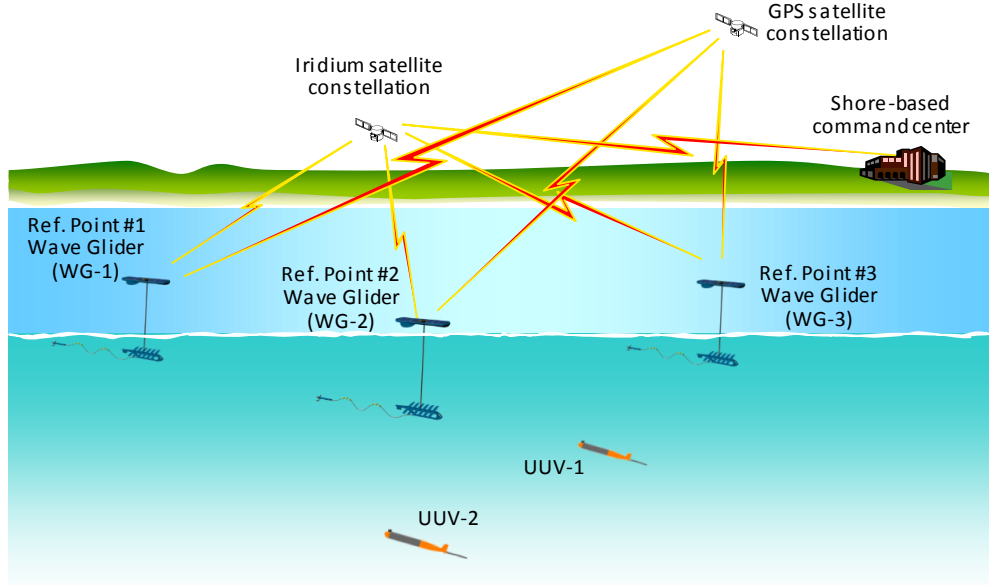
Figure 34.   Simulation Scenario

The true trajectory of the UUVs is depicted in Figure 35. The UUVs are set to navigate at 1 knot in an area with a constant current of 0.5 knots at 135°. The starting point for UUV-1 is (-400m, 1400m) and for UUV-2 is (1000m, 1400m), in a Cartesian

coordinate system. For simplicity, the WGs are considered stationed at fixed positions, as in a perfect hovering mission.
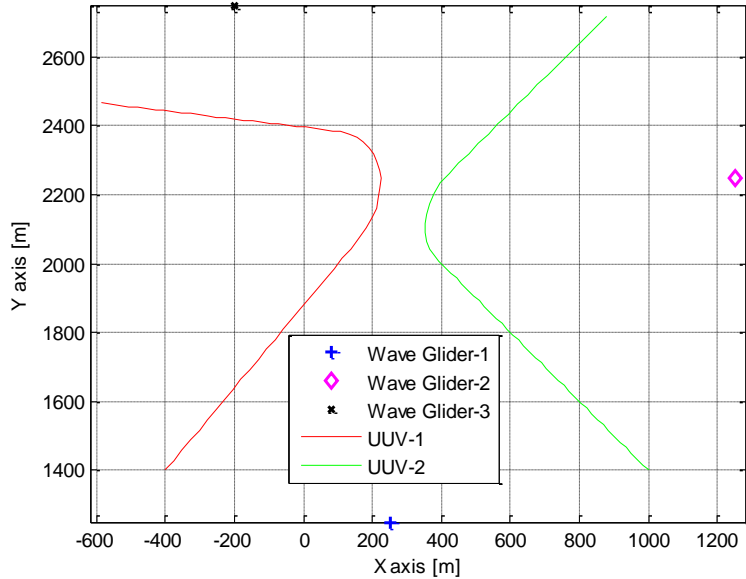
Figure 35.   UUVs True Trajectory

A.   IDEAL CASE

In this ideal case, each UUV has a successful measurement every three minutes, as depicted in Figure 36. As described in Chapter II, a measurement from the UUVs to two or more reference points (WGs) at the same time is not possible, and no bearing information associated with the distance measurements is available. Therefore, in the xy-plane, each measurement represents a circle of possible UUV positions (see Figure 37).
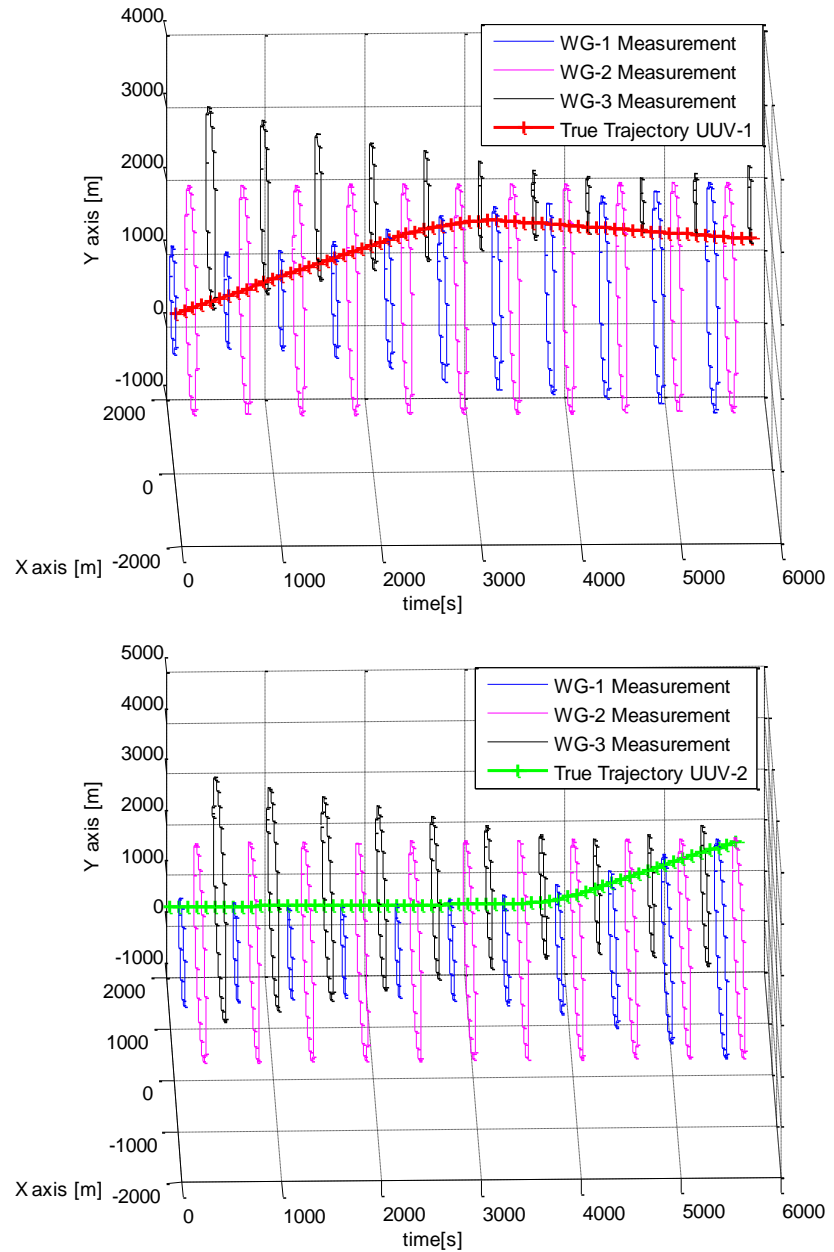
Figure 36.　　Time Evolution of the Distance Measurements, Ideal Case
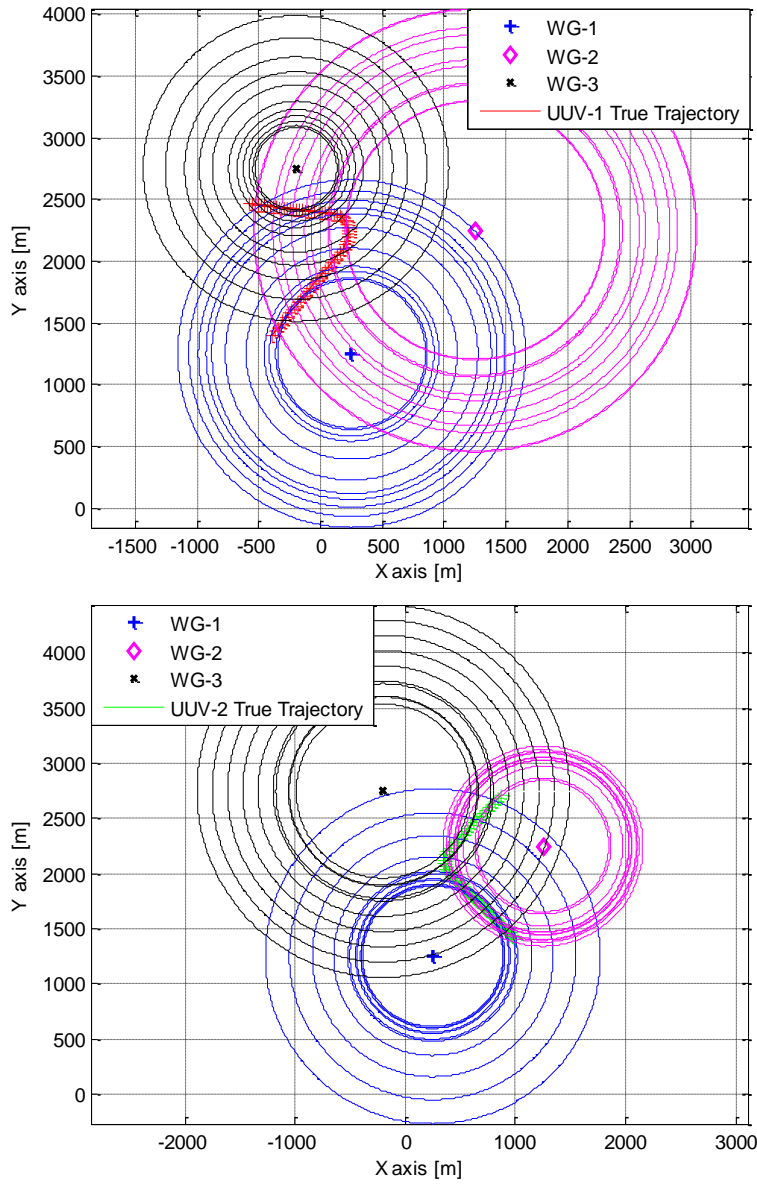
Figure 37.   Distance Measurements in xy-Plane, Ideal Case

Figure 38 shows the tracking results (predicted and smoothed trajectories) for both algorithms (EKF and UKF) and in Figure 39 the tracking errors are presented. The prediction errors in Figure 39 show that both algorithms converge to the true trajectory, but UKF converges faster. A comparison in Figure 39 between predictions and smoothed

trajectories shows how useful the smoother is to reduce the errors during the transient portion of the tracking.

Figure 40 shows the consensus current results. As UKF running in the UUVs was able to converge to the true current faster, the consensus current based on the UKF tracking has a smoother profile and converges faster than EKF.
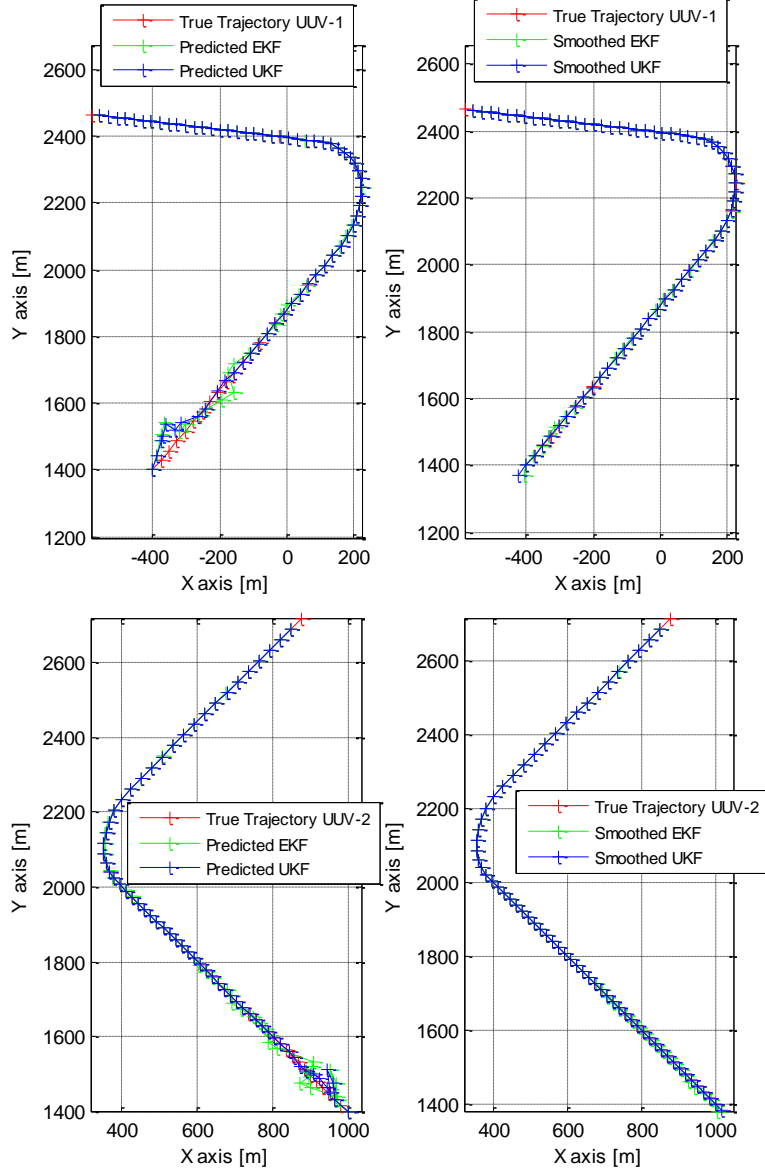
Figure 38.   Tracking Results, Ideal Case
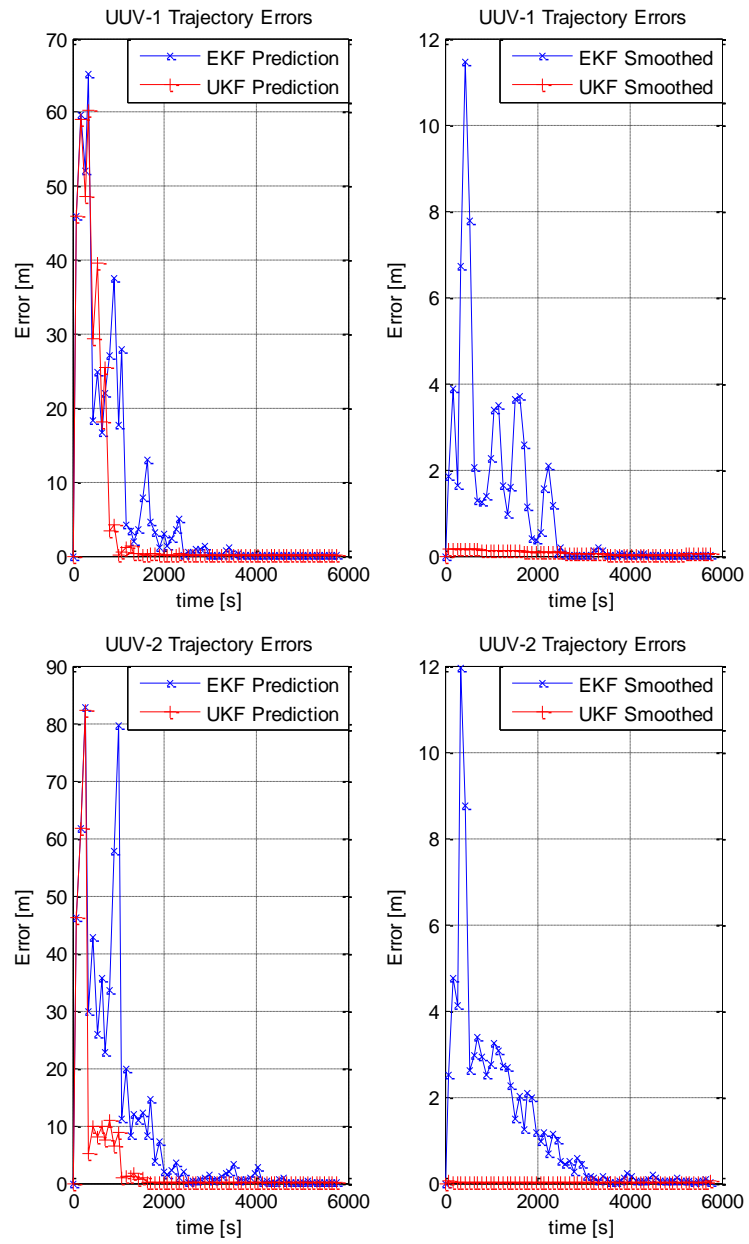
Figure 39.   Error Analysis, Ideal Case
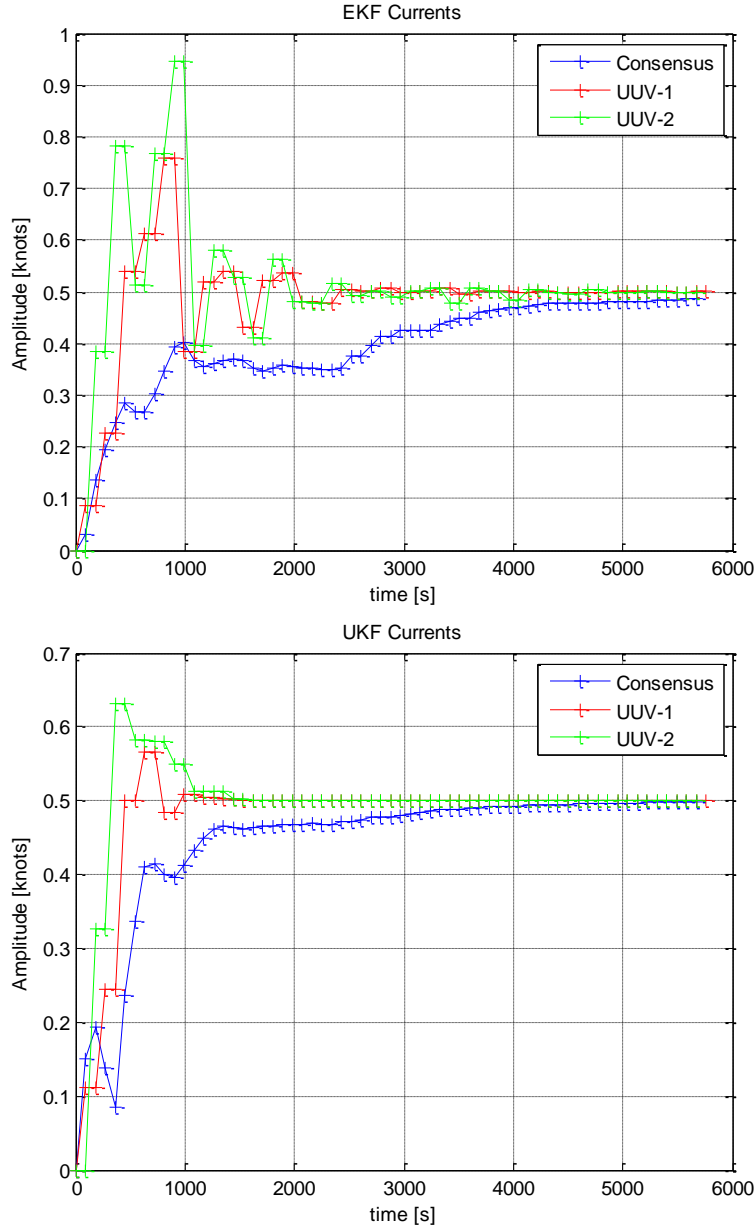
Figure 40.   Consensus Current, Ideal Case

B.   MEASUREMENT FAILURE

In this case, the UUVs are experiencing a failure in the distance measurement during part of their mission, as depicted in Figures 41 and 42. The tracking results show that both algorithms converge to the true trajectory, although the EKF takes more time and is highly affected during the turn (see Figures 43 and 44). A comparison in Figure 44

between predictions and smoothed trajectories shows that the smoother was able to reduce the tracking errors during the transient portion of the tracking and during the period of failure in the measurements.

Figure 45 shows the consensus current results. As in the previous case, because UKF running on the UUVs was able to converge to the true current faster, the consensus current based on UKF tracking has a smoother profile and converges faster than EKF.
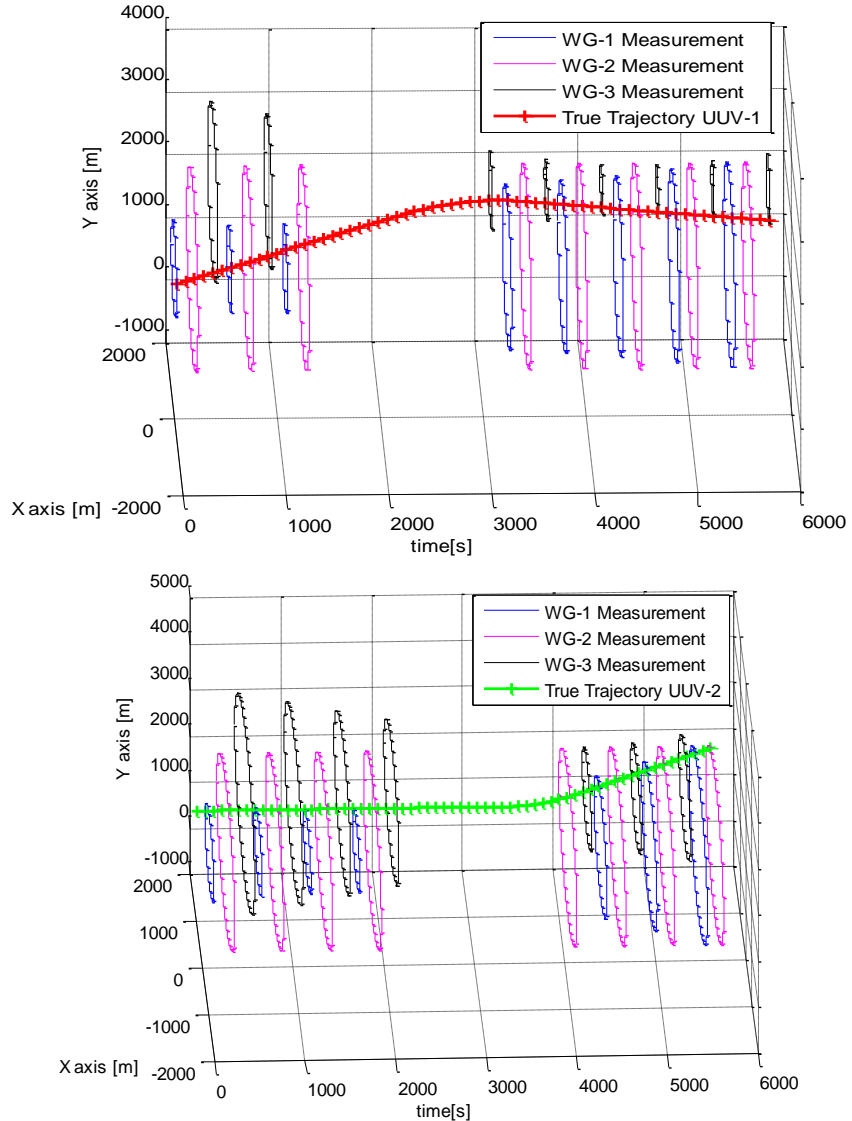
Figure 41.　Time Evolution of the Distance Measurements,
Measurement Failure Case

90
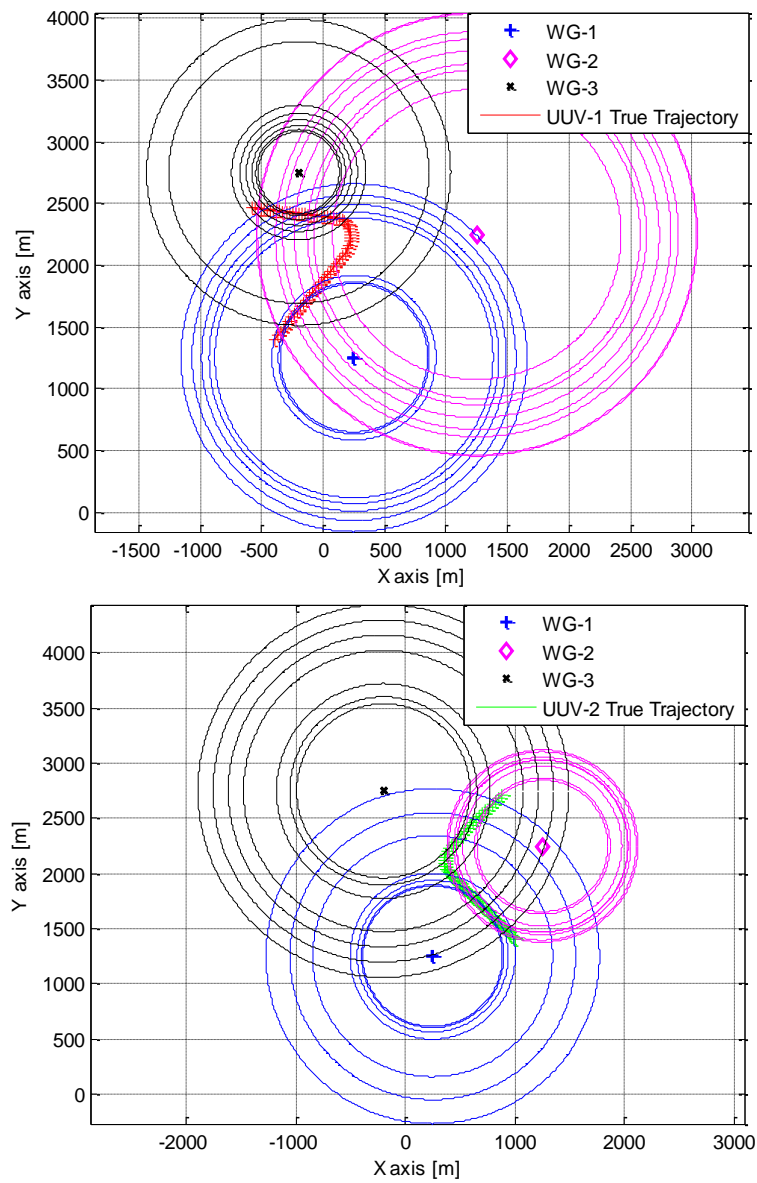
Figure 42.   Distance Measurements in xy-Plane, Measurement Failure Case
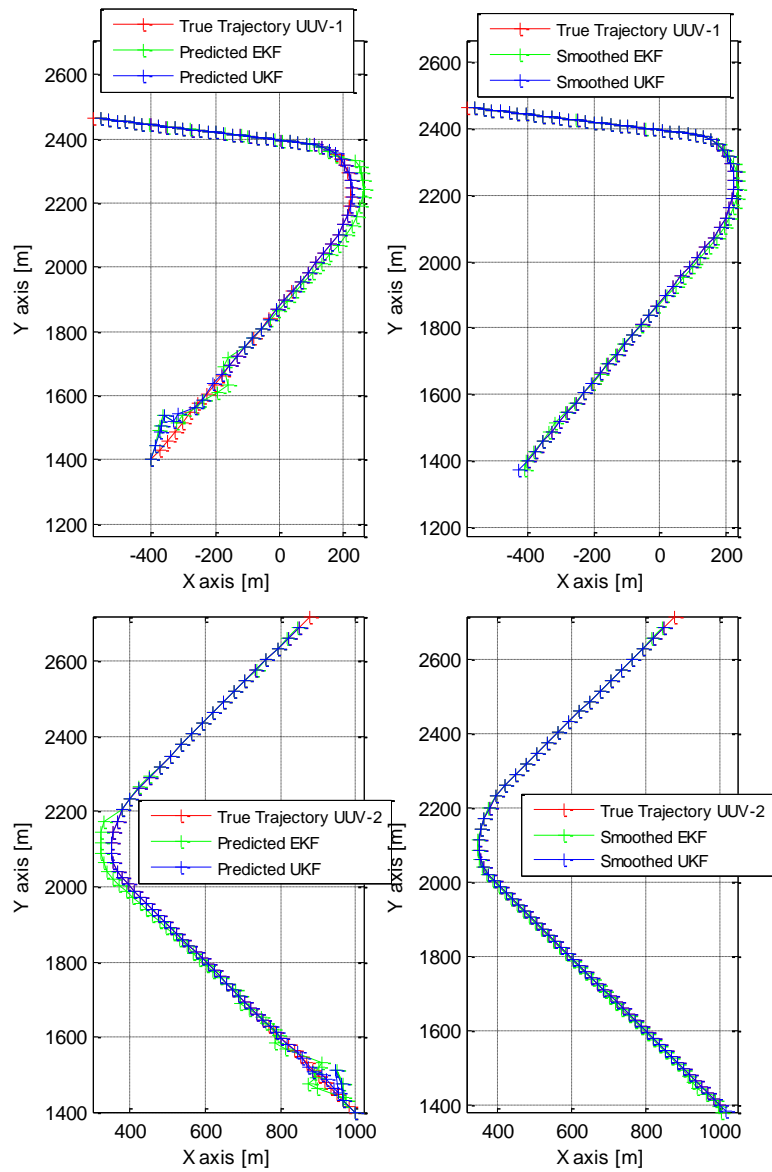
Figure 43.   Tracking Results, Measurement Failure Case
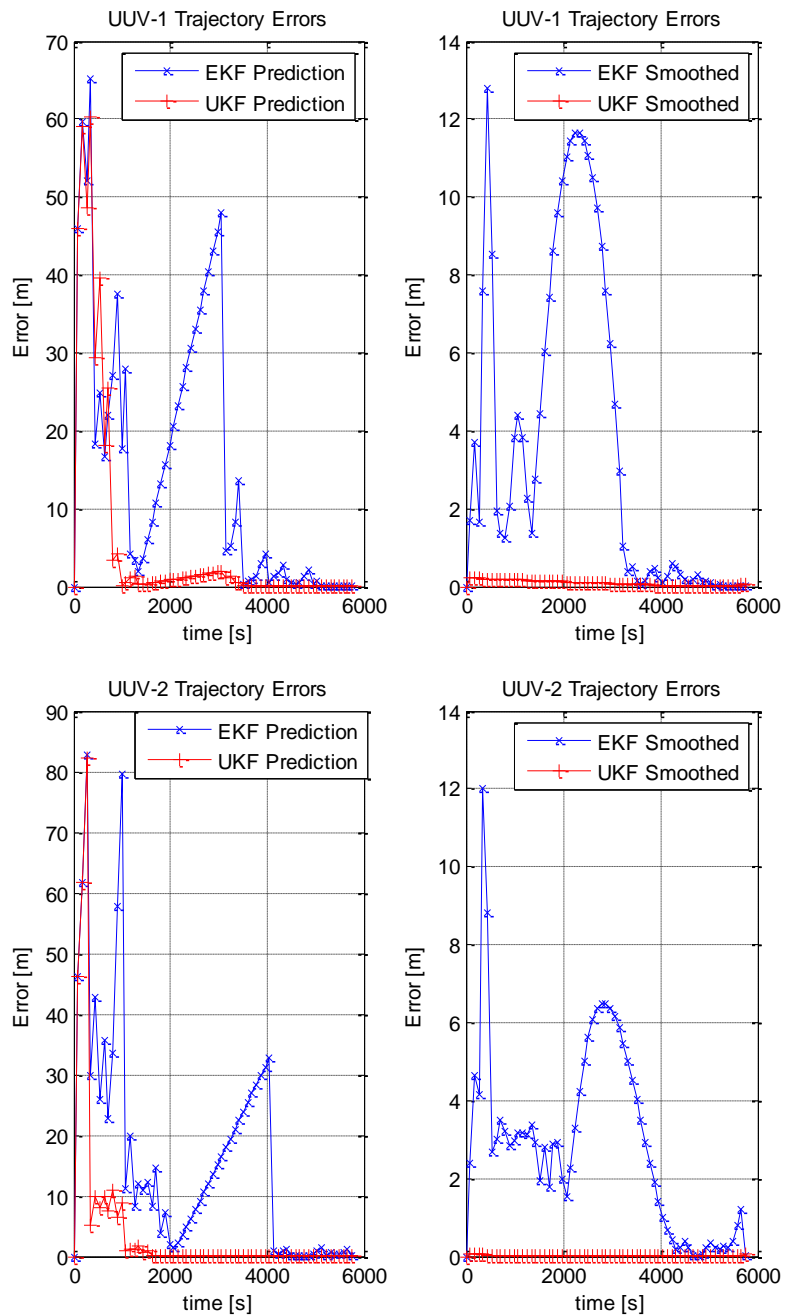
Figure 44.　Error Analysis, Measurement Failure Case
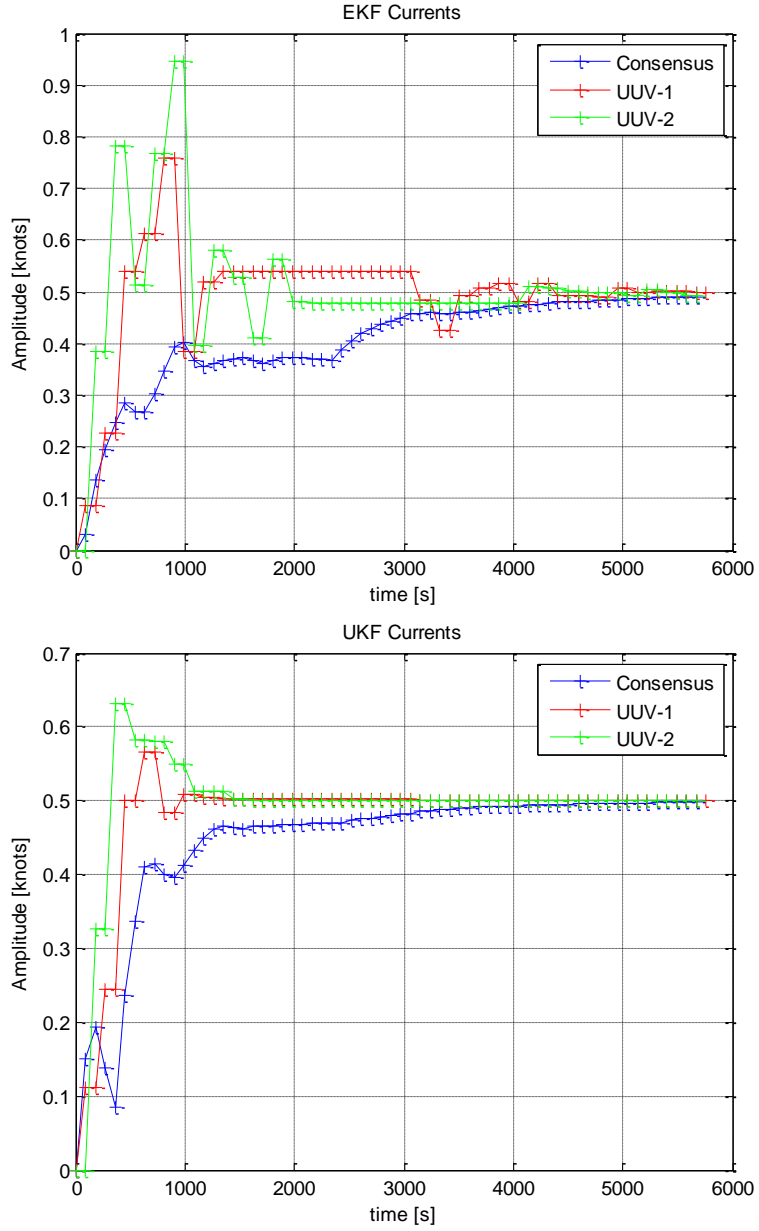
Figure 45.   Consensus Current, Measurement Failure Case

C.   SIMULATIONS WITH MEASUREMENT NOISE

For this case, in addition to measurement failures presented in Figures 41 and 42, noise is added in the distance measurements. To account for the random characteristics of the noise, Figures 46, 47, and 48 are the result of the average of 100 simulations.

As described in Chapter IV, distances underwater are estimated using the one-way travel time, and the one-way travel time is estimated by the time of the highest peak in the modem's matched filter output. In a multipath environment, the arrival with higher energy (highest peak) is not always the direct path (first group of arrivals) but is representative of a bottom/surface bounce arriving later. As a consequence, the distance is overestimated, which means that the errors associated with the distance measurements are always positive (biased noise). This particular characteristic is considered in the simulations.

The tracking results show that both algorithms converge to the true trajectory but the errors are higher than in the previous cases. In Figure 47, it can be seen that UKF has a more stable behavior and smaller errors when compared with EKF, probably because UKF was able to handle the biased noise better. This result is consistent with the claim that UKF, by the use of *sigma points*, can capture the characteristics of the true distribution better than EKF.

A comparison in Figure 47 between predictions and smoothed trajectories shows that the smoother was able to reduce the tracking errors. In Figure 48, the consensus current results show that the consensus based on the UKF tracking has a smoother profile and converges faster than EKF.
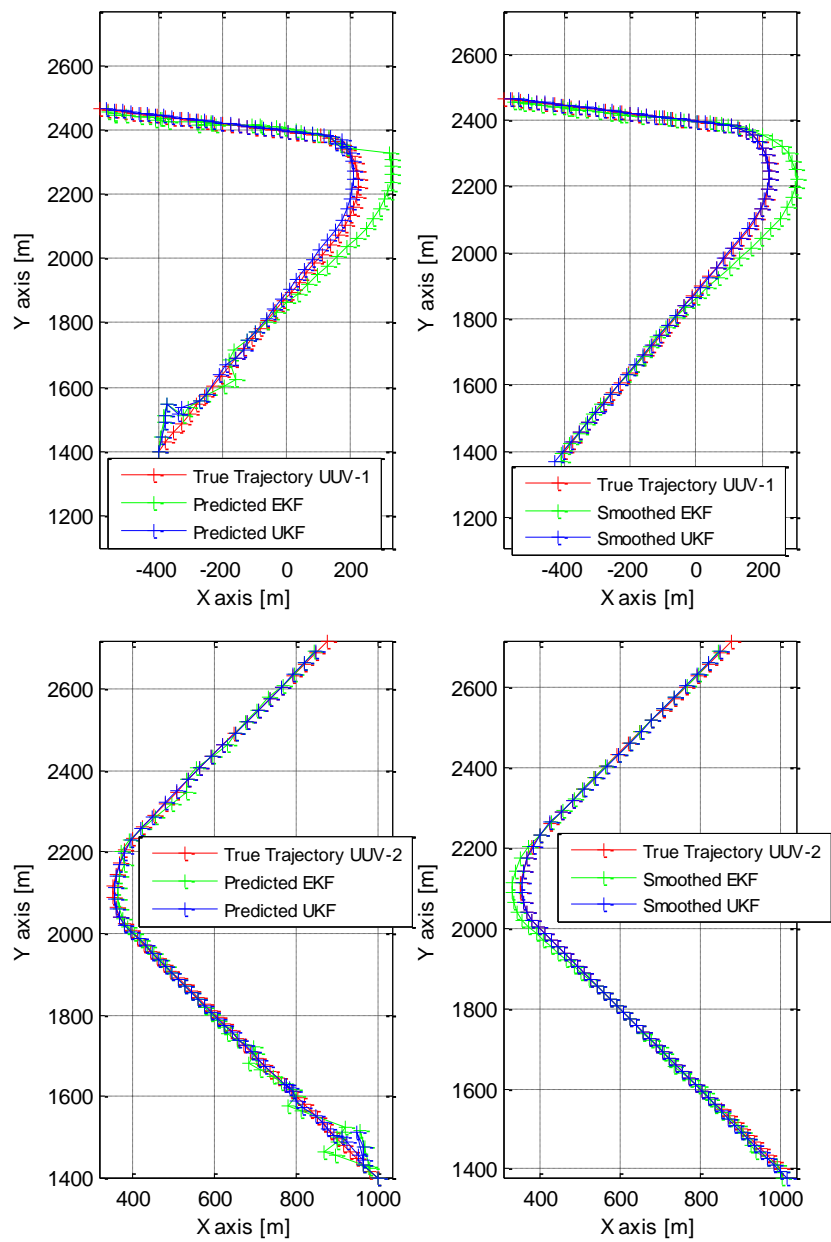
Figure 46.   Tracking Results, Measurement Failure Case Plus Noise
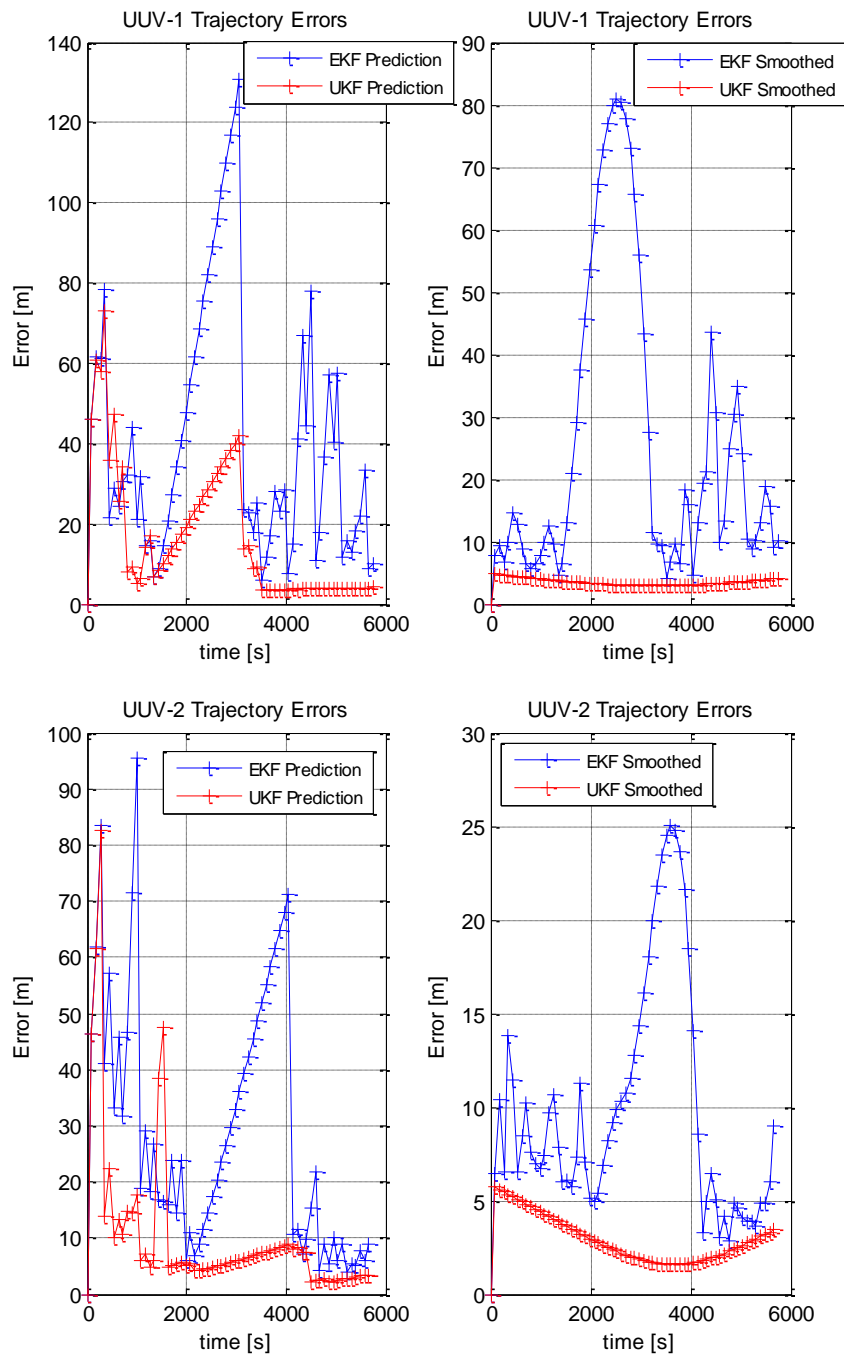
Figure 47.   Error Analysis, Measurement Failure Case Plus Noise
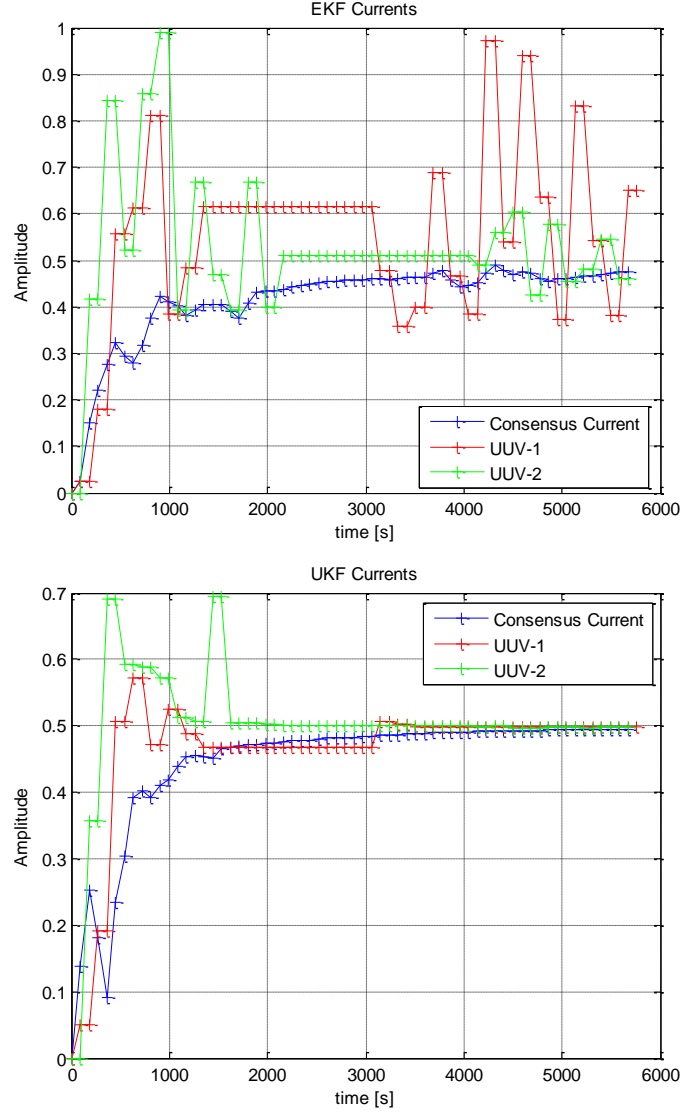
Figure 48.   Consensus Current, Measurement Failure Case Plus Noise

D.   CURRENT ESTIMATION BY THE CONSENSUS ALGORITHM

In the previous sections, the consensus current algorithm was demonstrated to produce a smoother profile and quicker convergence than EKF when the tracking results from the UKF-based algorithm were used as input. In this section, the tracking results from UKF are used in a situation where the UUVs are experiencing slightly different currents. UUV-1, navigating at 1 knot, is experiencing a current of 0.45 knots at 135° and UUV-2, navigating at 1 knot, is experiencing a current of 0.6 knots at 132°. Their

trajectories are depicted in Figure 49. The scenario defined was consistent with the case described in Section C (measurement failure plus noise).
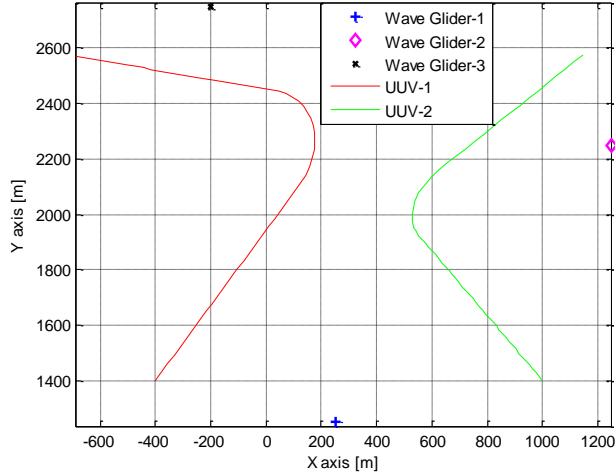
Figure 49.   True Trajectory of UUVs (Experiencing Different Currents)
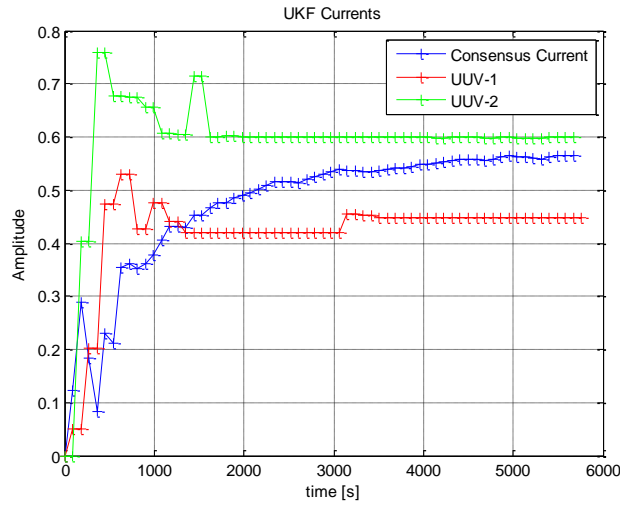
Figure 50.   Consensus Current, UUVs Experiencing Different Currents

In Figure 50 it can be seen that the consensus current stabilizes to a value between the two true currents. Probably due to a lower covariance associated with the current predictions from UUV-2 (i.e., predictions for UUV-2 converge faster), the consensus current is closer to this value.

THIS PAGE INTENTIONALLY LEFT BLANK

VII. SEA TESTS

In this chapter, the results of the sea tests that took place in Monterey Bay in August 2015 are presented. In a one-week sea test, two Liquid Robotics Wave Gliders (unmanned surface vehicles, or USVs named Mako and Tiburon) and a command ship (NOOA R/V Fulmar), all equipped with Teledyne-Benthos acoustic modems (ATM-900 series) and GPS connectivity are forming a network of reference points for an Exocetus Coastal Glider (UUV named LG16), which is also equipped with the same type of acoustic modem (see Figure 51).

The objective of the sea test was to evaluate the ability of the tools developed in this work (i.e., the tracking algorithm and matched peak impulse response processor) to track the UUV. During the sea tests, several one-hour missions were successfully conducted. For each mission, the UUV navigation system recorded its position predictions and, due to miscalibration and misalignment of its sensors and the sea current, errors of the order of 500 meters and above were observed between the final UUV predicted position and its GPS location, measured soon after it surfaced.

During the course of the missions, several travel time measurements between the UUV and the reference points were successfully recorded. The travel times were converted to horizontal distances and supplied to the tracking algorithm for processing.
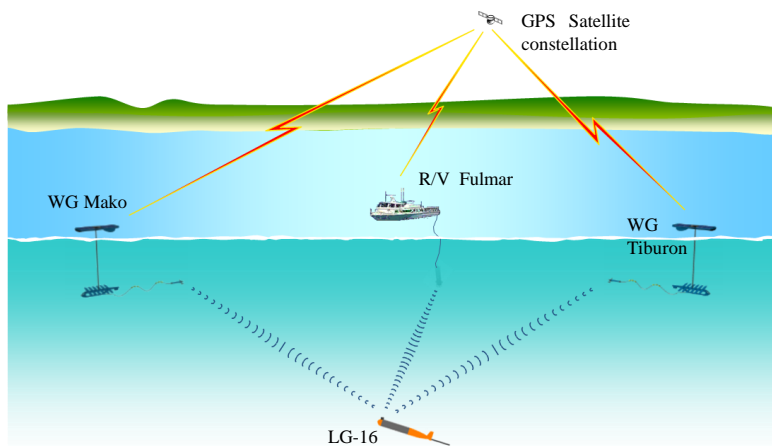
Figure 51.   Sea Test Configuration

A. KEY ASSETS

This section provides the basic characteristics and capabilities of the UUV and the Wave Gliders used in the sea trials.

1. Exocetus Coastal Glider

This vehicle makes use of a buoyancy engine to achieve forward motion in a saw tooth pattern by descending and ascending from changes in its buoyancy. There are no external moving parts or propeller. To maneuver, the glider has to pitch and roll its internal battery. It can carry a payload of 5 kg, and can reach speeds up to 2 knots. Its navigation system relies on a digital magnetic compass board and speed estimates based on the buoyancy engine dynamics. Communications capabilities include Iridium, UHF (Freewave radio modem), and WiFi.

Figure 52.   Exocetus Coastal Glider. Source: Exocetus Autonomous Systems, www.exocetussystems.com

Here at the Naval Postgraduate School the vehicle was rigged on its head with a syntactic foam mount for the acoustic modem as seen in Figure 53. The purpose of the synthetic foam mount was to offset the weight of the modem transducer to avoid interference with the buoyancy engine operations.

Figure 53.   Coastal Glider Rigged with Syntactic Foam Mount for Acoustic Modem

2.   Liquid Robotics Wave Glider

This is a hybrid vehicle composed of a surface (or float) unit and an underwater (or sub) unit attached to each other via a tether (umbilical cable). The underwater unit is able to convert part of the upward and downward motion of the water column into forward motion by using its cantilevered wings. As waves move the system up and down, the underwater unit acts as a tug pulling the surface float along a predetermined course. It can tow up to 500 kg, and can reach speeds up to 3 knots. It has GPS connectivity and communications capabilities that include Iridium and WiFi. The WGs used in the sea tests also have an acoustic modem installed in a towfish structure, for communication with the UUV, as represented schematically in Figure 55.
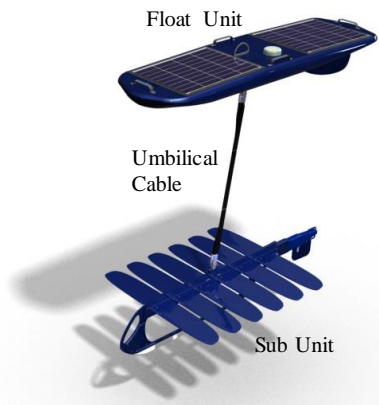
Figure 54.   Liquid Robotics Wave Glider Model SV2. Source: Liquid Robotics,
https://www.liquid-robotics.com/
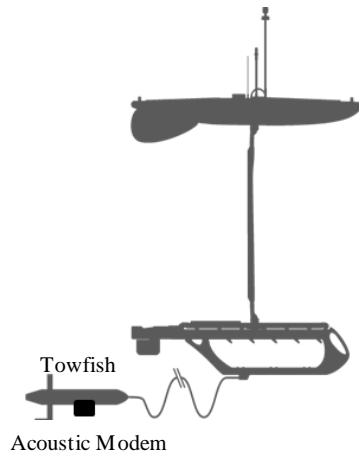
Figure 55.   Wave Glider Equipped with Towfish Modem. Adapted from Liquid Robotics,
https://www.liquid-robotics.com/

B.   AREA OF OPERATION AND ENVIRONMENTAL CHARACTERISTICS

The assets were operating in a relatively flat area around 75 m of depth at the edge of the Monterey Bay submarine canyon about 5 nautical miles from the shore (see Figure 19). Sediments in the area were identified as being silt-clay/sand-silt-clay and modeled as a fluid-like half-space, according to [37], with the following characteristics:

- Compressional sound speed: 1560 m/s;
- Density: 1.6 g/cm^3;
- Attenuation for compressional waves: 5dB/m.

The sound speed profile was measured by the UUV during the tests, and its average is depicted in Figure 56.
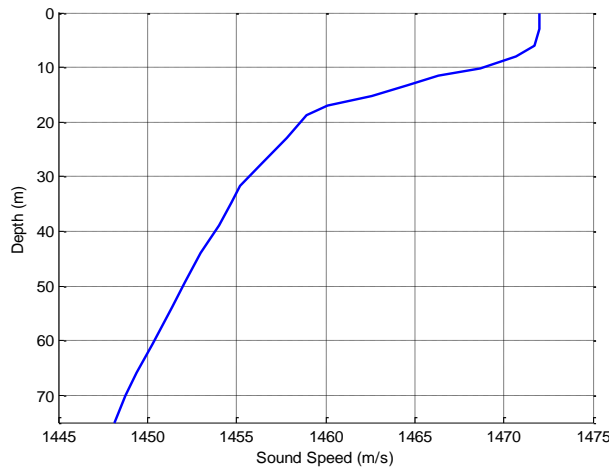
Figure 56.   Average Sound Speed Profile Measured by the UUV on August 12, 2015

C.   UUV MISSIONS

After a week of preliminary tests, on August 12, 2015, four UUV missions were run. For three of them, successful travel time measurements from the UUV to the reference points were recorded. Those travel times were converted into distances using the algorithm described in Chapter IV, Section B.2.c. The travel time data, the data from the UUV navigation system, and the coordinates of the reference points were supplied to the tracking algorithm for processing. All data collected was post processed.

The tuning parameters were selected automatically using the algorithm described in Chapter V, Section E, and the objective function used was the residual prediction error. Data after the smoothing was used to calculate the objective function. Unfortunately, the EKF method proved to be unstable for automatic tuning using real data. The results presented in this section include only UKF.

To verify the effectiveness of the algorithm described in Chapter IV, Section B.2.c, a comparison of the tracking results using distance estimations according to that section and distances roughly estimated are performed. For the purpose of this dissertation, the term *distances roughly estimated* is defined as being the result of the multiplication of the one-way travel time by the characteristic medium sound speed, corrected by the asset's depth (representing a horizontal distance).

Based on the sound speed profile depicted in Figure 56, the rough estimates of the distances from the UUV to the reference points are calculated using a constant sound speed of 1465 m/s (corresponding to the sound speed associated with typical depths of the reference points and the UUV when the measurements were recorded).

1.   Data Collection and Sources of Errors

Despite our efforts to minimize and account for errors in measurements, we identified the following main sources of errors that introduce uncertainties and may affect the tracking results:

- Wave Glider GPS positions: The WGs record their GPS positions in 5-minute intervals. In order to establish their position at the instant of a travel time measurement it becomes necessary to interpolate between GPS recordings.

- Offset between the GPS antenna and the acoustic modem: Due to the use of the tow fish, the GPS antenna on a WG is displaced from the acoustic modem transducer (see Figure 55). The estimated displacement is around 4 to 6 meters, and the sub unit heading can be used to apply a correction in the proper direction.

- Sound speed profile: The sound speed profile represented in Figure 56 is the average of the UUV's measurements during several dives throughout its mission (and extrapolated to the area depth). The actual measurements are depicted in Figure 57. The variability in the sound speed profile may cause errors in distance estimations based on the matched peak IR algorithm by affecting the amplitude of the arrivals.

- Acoustic modem beam patterns: As mentioned in Chapter IV, Section B.2.d, the vertical and horizontal beam patterns are considered omnidirectional. To be able to take into account the standard transducer beam pattern, as well as the effects of mounting onto the UUV and tow fish bodies, the beam patterns should be measured when the modems are mounted in their respective structures. The omnidirectional assumption may cause errors in distance estimations based on the matched peak IR algorithm by affecting the amplitude of the arrivals.
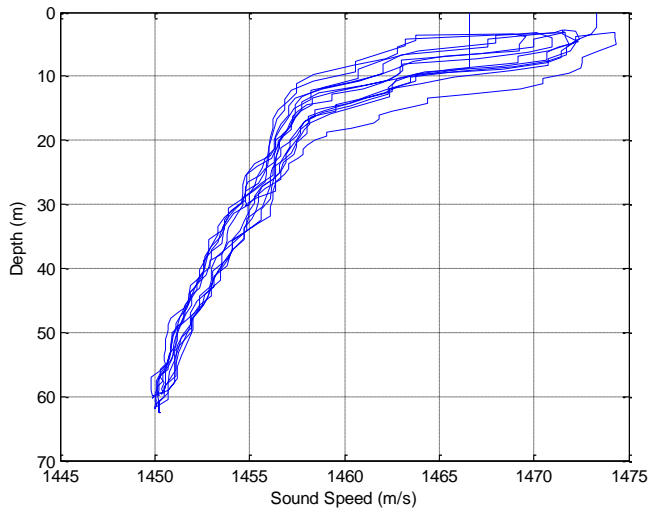
Figure 57.   Sound Speed Profile as Measured by the UUV on August 12, 2015

2.   Mission-1

Mission-1 started at 09:34:24 AM and ended at 10:36:48 AM. During this period of time the UUV navigation system recorded its estimated postion. Due to errors in dead reckoning and the sea current, an error of 1095 meters was observed between the final UUV predicted position and its GPS location measured soon after it surfaced (see Figure 58).

During the course of this mission, several travel time measurements between the UUV and the reference points were successfully recorded. The travel times were converted to horizontal distances using the algorithm described in Chapter IV, and the evolution of the distance measurements over time is depicted in Figure 59.

Note that the measurements were recorded from the UUV to only two reference points and in an inconsistent manner. Ideally, the measurements should be taken at constant time intervals to different reference points in a orderly manner, as shown in Chapter VI, Figure 36. Another important point is that no measurement was recorded during the first 3 minutes and 30 seconds, and during the last 5 minutes and 43 seconds of the mission, as well.
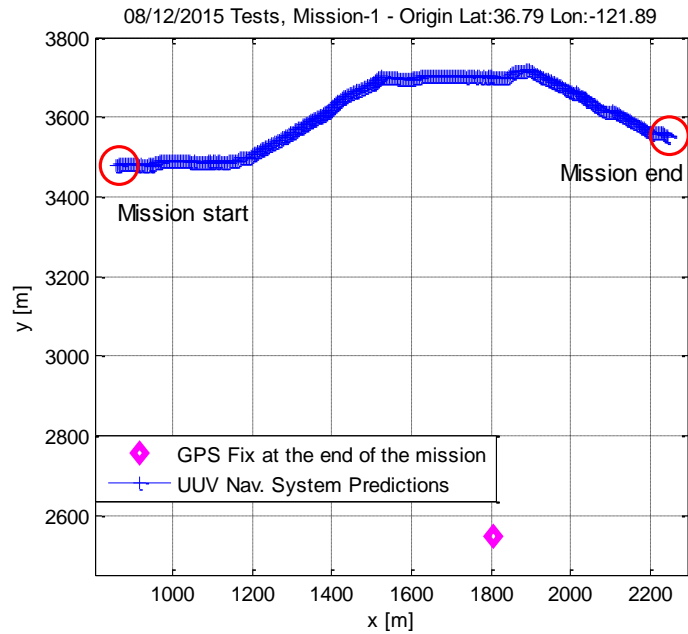
Figure 58.   August 12, 2015, Mission-1
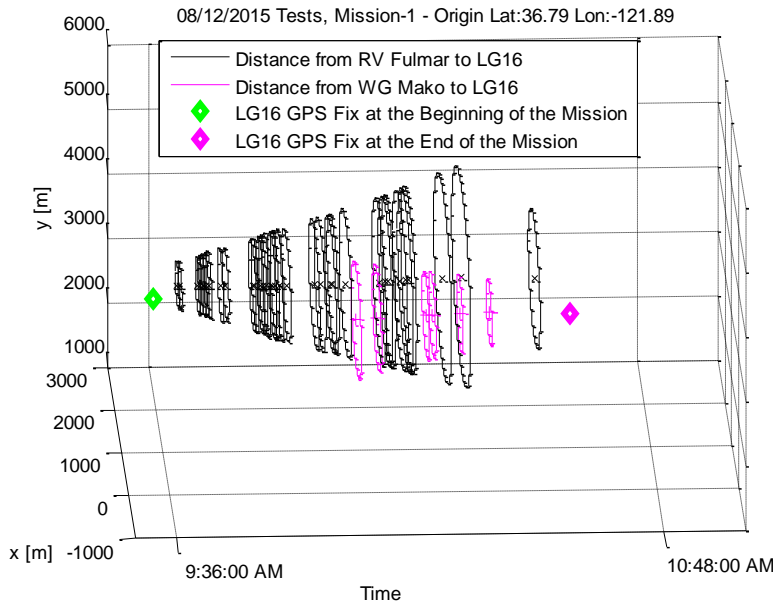
Figure 59.   Mission-1, Time Evolution of the Distance Measurements

The tracking results after automatic tuning, using the distances from the UUV to the reference points estimated according Chapter IV, Section B.2.c, are presented in

Figure 60. Despite the inconsistent measurements, the automatic tuning algorithm was able to find the optimum parameters that provided consistent tracking.
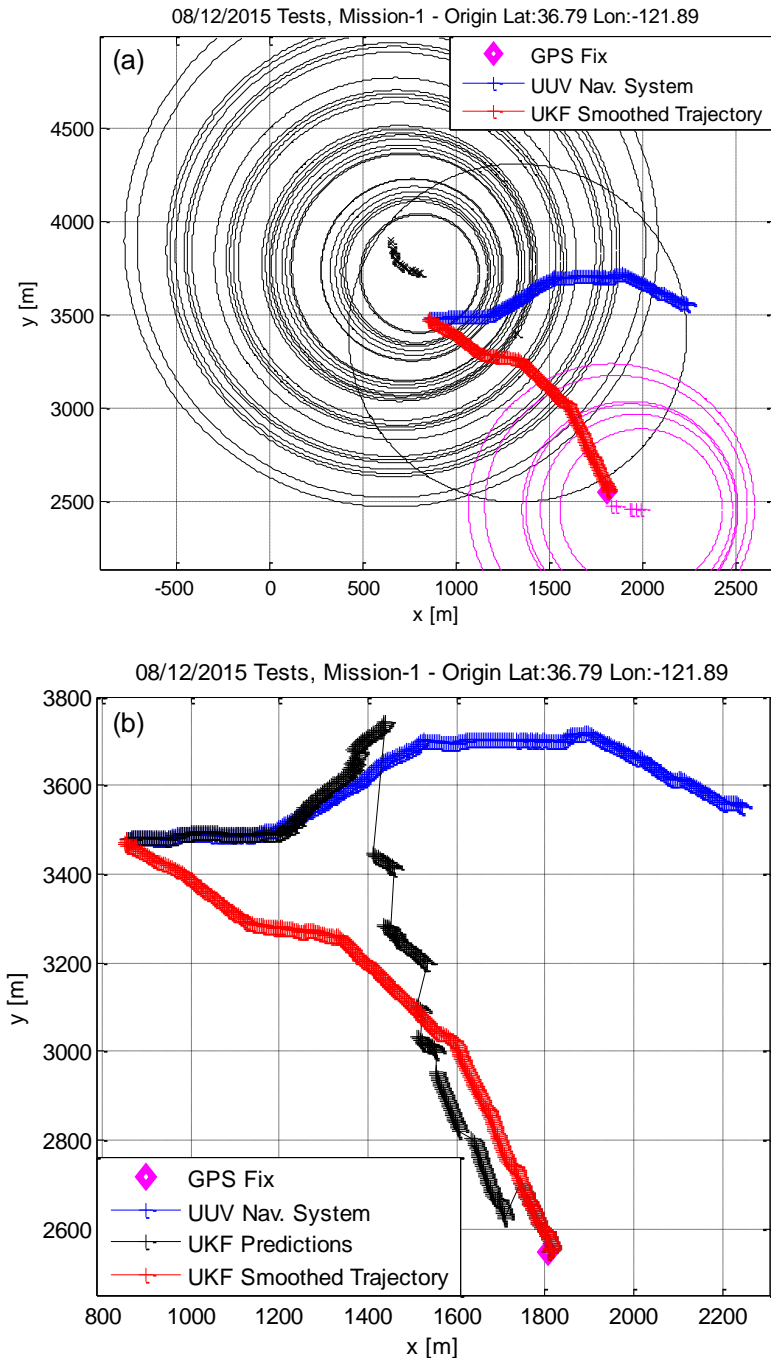
Figure 60.   Mission-1, Results after Automatic Tuning

As seen in Chapter V, Section G, for each prediction there is an associated covariance matrix, and the eigenvalues and eigenvectors of the covariance matrices may be used to represent confidence ellipses around the predictions. Despite some limitations [38], this procedure can provide good information about the uncertainty associated with the predicted states.

In Figure 61, the smoothed covariance matrix associated with the last prediction was used to construct a confidence ellipse around it. The lengths of the main axes were calculated by the square root of the associated covariance matrix eigenvalues and the main axes' directions were taken from the eigenvectors. The confidence ellipse major axis is 7 meters, and the minor is 2 meters. Despite the numbers in Table 2 indicating a "perfect tracking" (i.e., the last prediction matches the GPS fix), the most important result shown by Figure 61 is the realistic size of the confidence ellipse and the fact that the GPS fix is located inside this ellipse.
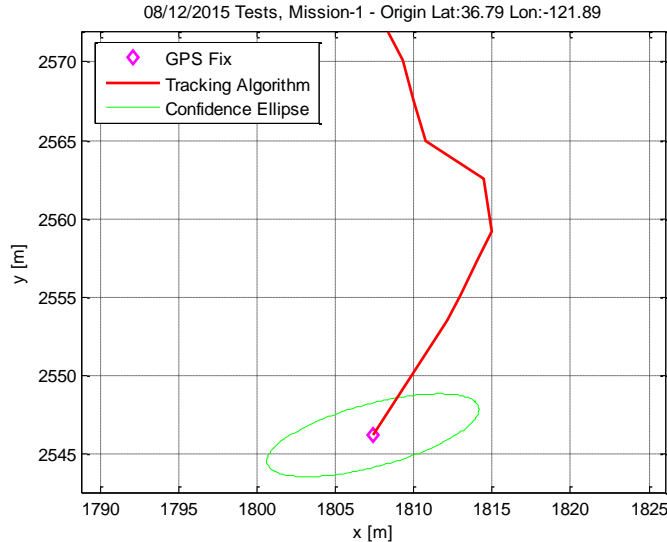
Figure 61.   Mission-1, Confidence Ellipse at the End of the Mission

The optimum tuning parameters for this mission are shown in Table 1. The parameter $\sqrt{R}$ represents the uncertainty associated with the measurements, combining the uncertainties in the horizontal distance and in the position of the reference points (in x

and y). A large $\sqrt{R}$ may represent a non-reliable or, in this case, inconsistent measurement. As already pointed out, in Figure 59 can be seen that we have scattered measurements to only two of the three reference points.

Table 1.   Mission-1, Optimum Tuning Parameters for Input Data Estimated According to Chapter IV, Section B.2.d

Tuning Parameters	
α	1.08×10^{-1}
β	3.82
κ	2.03×10^{-9}
$q\ [\mathrm{m^2/s^3}]^a$	2.09×10^{-3}
$\sqrt{R}\ [\mathrm{m^2}]$	4.65×10^5

α, β, and κ have no dimensions;

[a] Units according to [38].

For this mission, tracking by dead reckoning (UUV navigation system) yielded an error of 1095 meters (see Figure 58). The tracking algorithm was tested and the results show a more reliable predicted position for the entire UUV trajectory (see Figure 60).

When a rough estimate for the distances is used, errors around 30 meters were observed at the end of the mission. While this is a significant improvement over the UUV's estimated position, it is based on simple straight line propagation that does not account for the refractive and multipath effects of the environment (Figure 62).

When the more complete algorithm described in Chapter IV is used, the tracking algorithm practically eliminates the error at the end of the mission (as represented in Figure 61, there are uncertainties associated with this prediction). This indicates that correlating the measured impulse response of the channel with a ray trace prediction may provide an improvement in the tracking accuracy.

Table 2.   Mission-1, Tracking Comparison

Mission-1	Distances according to Chapter IV	Distances roughly estimated
Objective Function [m^4]	0.47	3.01x10^8
Error at beginning of the Mission [m]	0.04	5.20
Error at end of the Mission [m]	0	29.7
Total Error [m]	0.04	34.9

The row *Error at beginning of the Mission* on Tables 2, 4, and 6 refers to the difference between the first predicted position and the UUV GPS fix at the beginning of the mission. The row *Error at end of the Mission* refers to the difference between the last predicted position and the UUV GPS fix at the end of the mission.
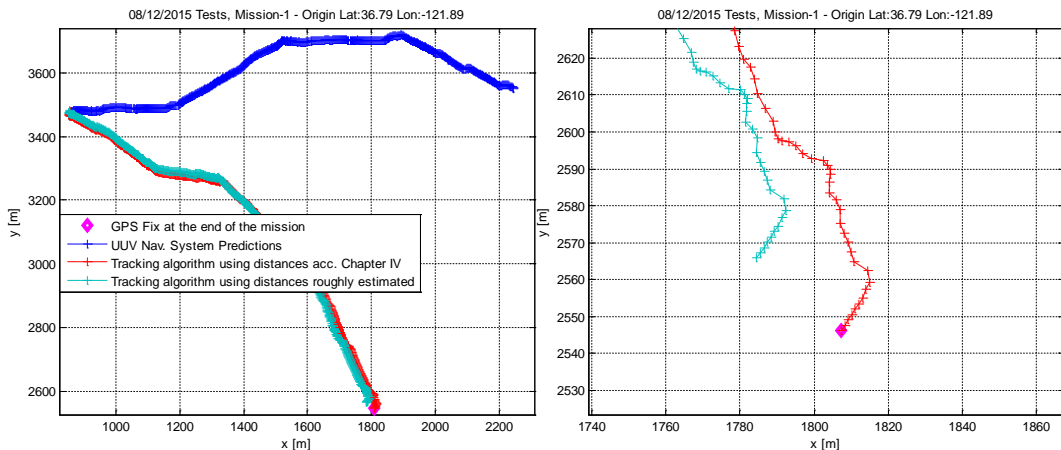
Figure 62.   Mission-1, Tracking Results when Processing the Distances Estimated According to Chapter IV and when Processing the Distances Roughly Estimated

The sea current predicted by the tracking algorithm for this mission is 0.60 knots (i.e., the average of the smoothed predictions) and has a general direction as represented in Figure 63a. It is worth noting the evolution of the tide during the mission period (see Figure 63b).

08/12/2015 Tests, Mission-1 - Origin Lat:36.79 Lon:-121.89
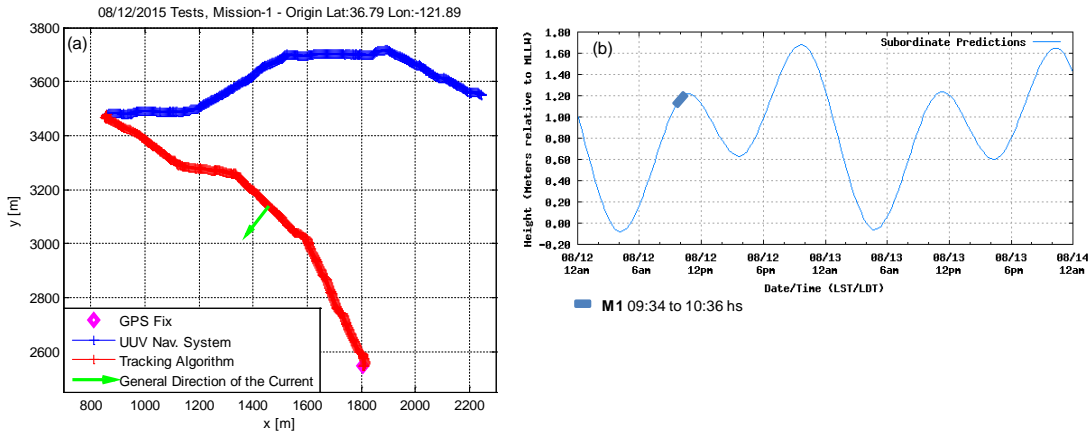
All tide charts in this dissertation were adapted from: https://tidesandcurrents.noaa.gov/noaatide predictions/viewDailyPredictions.jsp?bmon=08&bday=12&byear=2015&timelength=daily&timeZ one=2&dataUnits=1&datum=MLLW&timeUnits=2&interval=highlow&format=Submit&Stationid =9413616.

Figure 63.   Mission-1, Tracking, Sea Current, and Tide

3.   Mission-2

Mission-2 started at 10:49:03 AM and ended at 11:51:38 AM. During this period of time the UUV navigation system recorded its estimated position. Due to errors in dead reckoning and the sea current, an error of 747 meters was observed between the final UUV predicted position and its GPS location, measured soon after it surfaced (see Figure 64).

During the course of this mission, travel time measurements between the UUV and the reference points were successfully recorded. The travel times were converted to horizontal distances using the algorithm described in Chapter IV, and the evolution of the distance measurements over time is depicted in Figure 65.

Note, in Figure 65, that just a few measurements were recorded, but in a more consistent way when compared with mission-1. Another interesting point is that measurements to all three reference points were successfully recorded and the last one was taken just 2 minutes and 21 seconds before the UUV GPS fix at the end of the mission. Note, too, that no measurement was recorded during the first 33 minutes and 50 seconds of this mission.
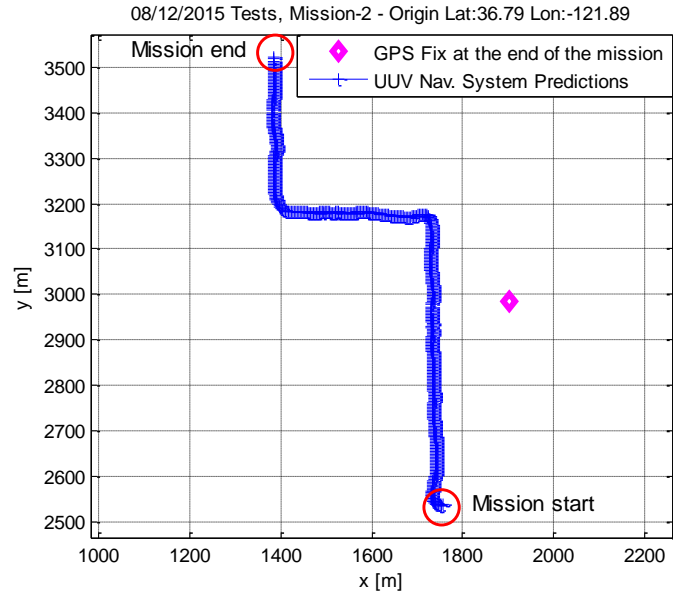
Figure 64.   August 12, 2015, Mission-2
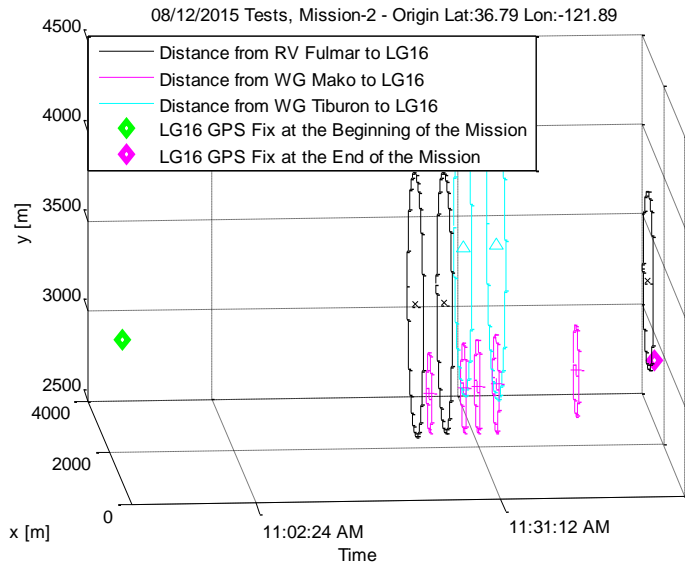
Figure 65.   Mission-2, Time Evolution of the Distance Measurements

The tracking results after automatic tuning, using the distances from UUV to the reference points estimated, as described in Chapter IV, Section B.2.c, are presented in Figure 66. Despite the few measurements, the automatic tuning was able to find the optimum parameters that provided a consistent tracking.

114

Due to the long period without measurements (at the beginning of the mission) and due to the poor performance of the UUV navigation system predicting its velocity, the non-smoothed predictions (represented by the black curve in Figure 66b) appear to be significantly off track before the measurements (represented by the "jumps" on the black curve). But measurements to different reference points were a decisive factor in getting the track on the correct path. In this particular case, the smoothing algorithm proved very important in producing a realistic UUV trajectory.
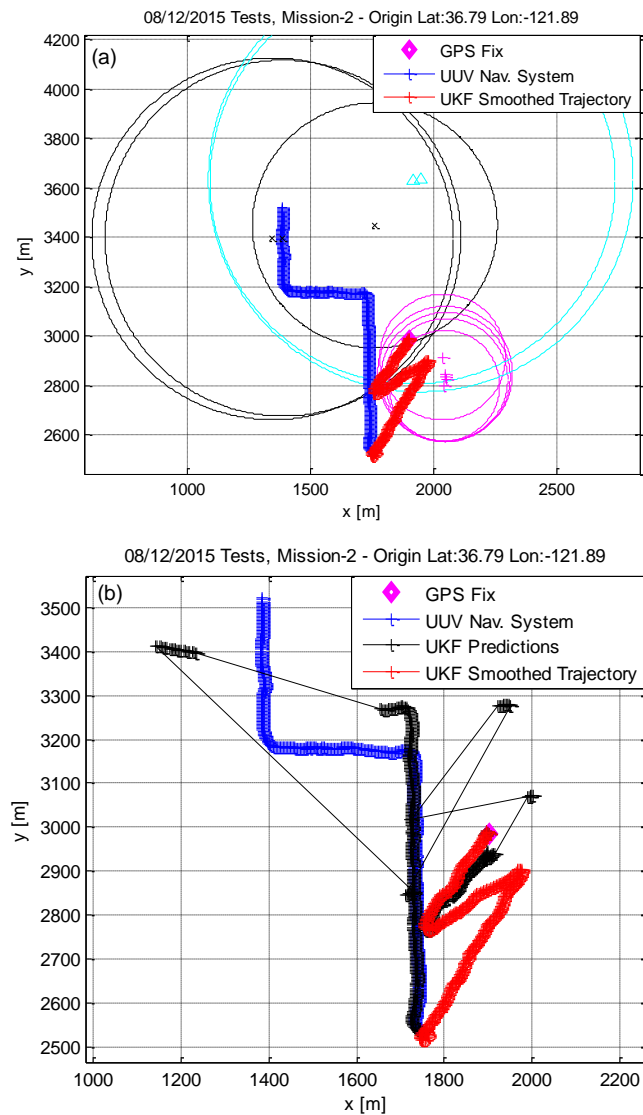
Figure 66.   Mission-2, Results after Automatic Tuning

In Figure 67, the smoothed covariance matrix associated with the last prediction was used to construct a confidence ellipse around it. The lengths of the main axes were calculated by the square root of the associated covariance matrix eigenvalues, and the main axes' directions were taken from the eigenvectors. The confidence ellipse major axis is 8 meters, and the minor is 2 meters. Despite the numbers in Table 4 indicating a "perfect tracking" (i.e., the last prediction matches the GPS fix), the most important result shown in Figure 67 is the realistic size of the confidence ellipse and the fact that the GPS fix is located inside this ellipse.
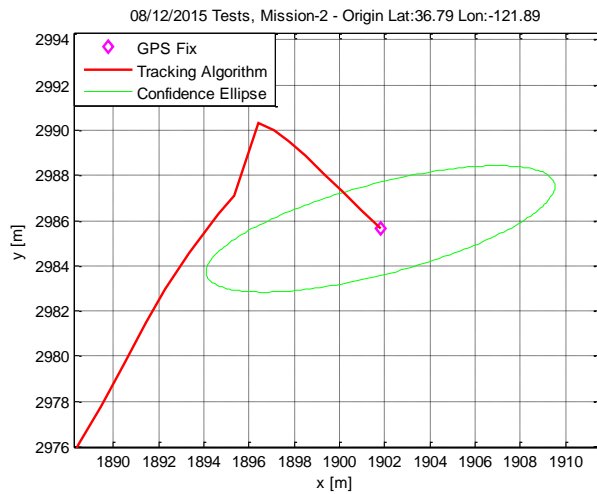
Figure 67.   Mission-2, Confidence Ellipse at the End of the Mission

The optimum tuning parameters for this mission are shown in Table 3. As can be seen, probably due to the more consistent measurement, the parameter $\sqrt{R}$ is in reasonable levels.

Table 3. Mission-2, Optimum Tuning Parameters for Input Data Estimated
According Chapter IV, Section B.2.d

Tuning Parameters	
α	3.05×10^{-1}
β	8.98×10^{-2}
κ	9.40×10^{-3}
$q\ [m^2/s^3]^a$	1.11×10^{-3}
$\sqrt{R}\ [m^2]$	10

α, β, and κ have no dimensions;

[a] Units according to [38].

For this mission, tracking by dead reckoning (UUV navigation system) yielded an error of 747 meters (see Figure 64). The tracking algorithm was tested and the results show a more reliable predicted position for the entire UUV trajectory (see Figure 66). When a rough estimate for the distances is used, errors around 39 meters were observed at the end of the mission. While this is a significant improvement over the UUV's estimated position, it is based on simple straight line propagation that does not account for the refractive and multipath effects of the environment (Figure 68).

When the more complete algorithm described in Chapter IV is used, the tracking algorithm produces no apparent error at the end of the mission (as represented in Figure 67, there are uncertainties associated with this prediction). This indicates that correlating the measured impulse response of the channel with a ray trace prediction may provide an improvement in the tracking accuracy.

Table 4. Mission-2, Tracking Comparison

| Mission-2	Distances according to Chapter IV	Distances roughly estimated
Objective Function [m^4]	0.04	402
Error at beginning of the Mission [m]	0.009	1.02
Error at end of the Mission [m]	0.004	39.1
Total Error [m]	0.013	40.1
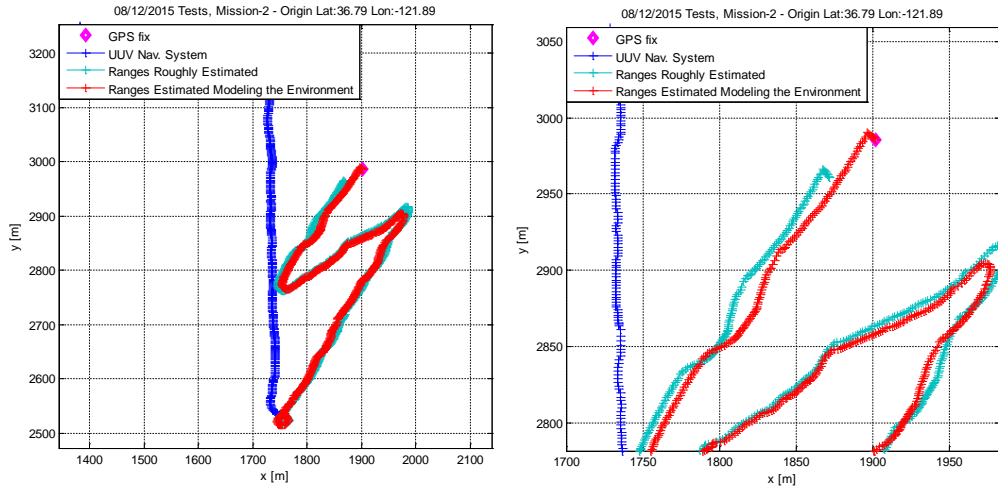
Figure 68. Mission-2, Tracking Results when Processing the Distances Estimated
According to Chapter IV and when Processing the Distances
Roughly Estimated

The sea current predicted by the tracking algorithm for this mission is 0.45 knots (i.e., the average of the smoothed predictions) and has a general direction as represented in Figure 69a. It is worth noting the evolution of the tide during the mission period (see Figure 69b).
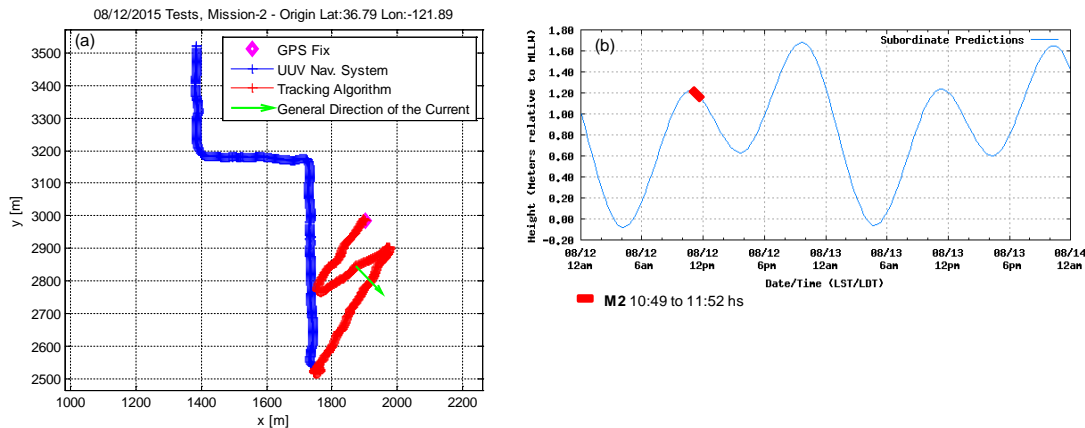
Figure 69.   Mission-2 Tracking, Sea Current, and Tide

4. Mission-3

Mission-3 started at 12:05:01 PM and ended at 13:07:38 PM. During this period of time the UUV navigation system recorded its estimated postion. Due to errors in dead reckoning and the sea current, an error of 476 meters was observed between the final UUV predicted position and its GPS location, measured soon after it surfaced (see Figure 70).

During the course of this mission, travel time measurements between the UUV and the reference points were successfully recorded. The travel times were converted to horizontal distances using the algorithm described in Chapter IV, and the evolution of the distance measurements over time is depicted in Figure 71.

Note the inconsistent measurement at the beginning and the lack of measurements just after the middle of the mission. In the last portion, however, measurements to all three reference points were achieved in a short period of time. The first measurement was not taken until 6 minutes and 15 seconds into the mission and the last one was taken 6 minutes and 37 seconds before the UUV GPS fix at the end.
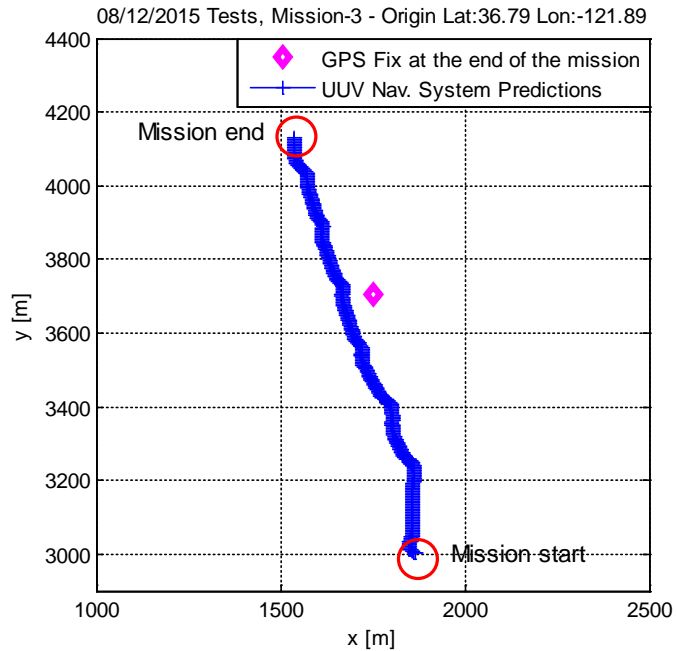

Figure 70.   August 12, 2015, Mission-3
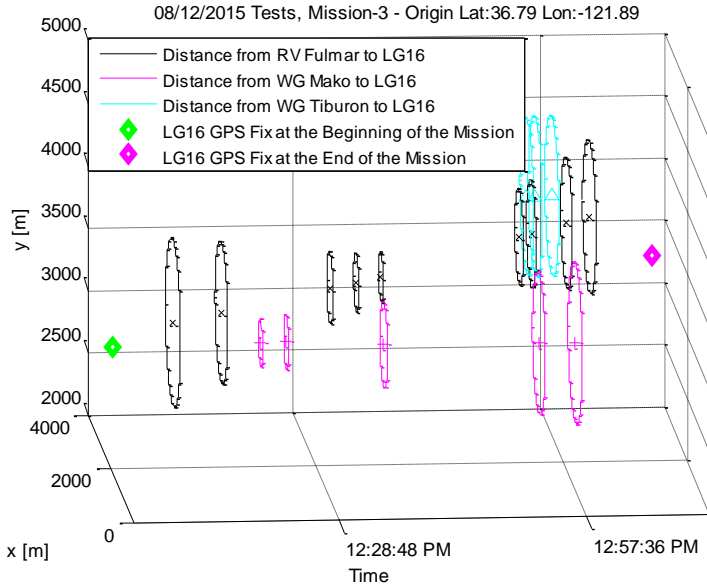
Figure 71.   Mission-3, Time Evolution of the Distance Measurements

The tracking results after automatic tuning, using the distances from UUV to the reference points estimated as decribed in Chapter IV, Section B.2.c, are presented in Figure 72. Despite the reduced number of measurements and the inconsistency during certain portions of the mission, the automatic tuning was able to find the optimum parameters that produced an error of 8.6 meters at the end of the mission (note that there are uncertainties associated with this prediction, as shown in Figure 73).

In Figure 73, the smoothed covariance matrix associated with the last prediction was used to construct a confidence ellipse around it. The lengths of the main axes were calculated by the square root of the associated covariance matrix eigenvalues, and the main axes' directions were taken from the eigenvectors. The confidence ellipse major axis is 27 meters, the minor is 14.5 meters, and the GPS fix is located inside this ellipse.
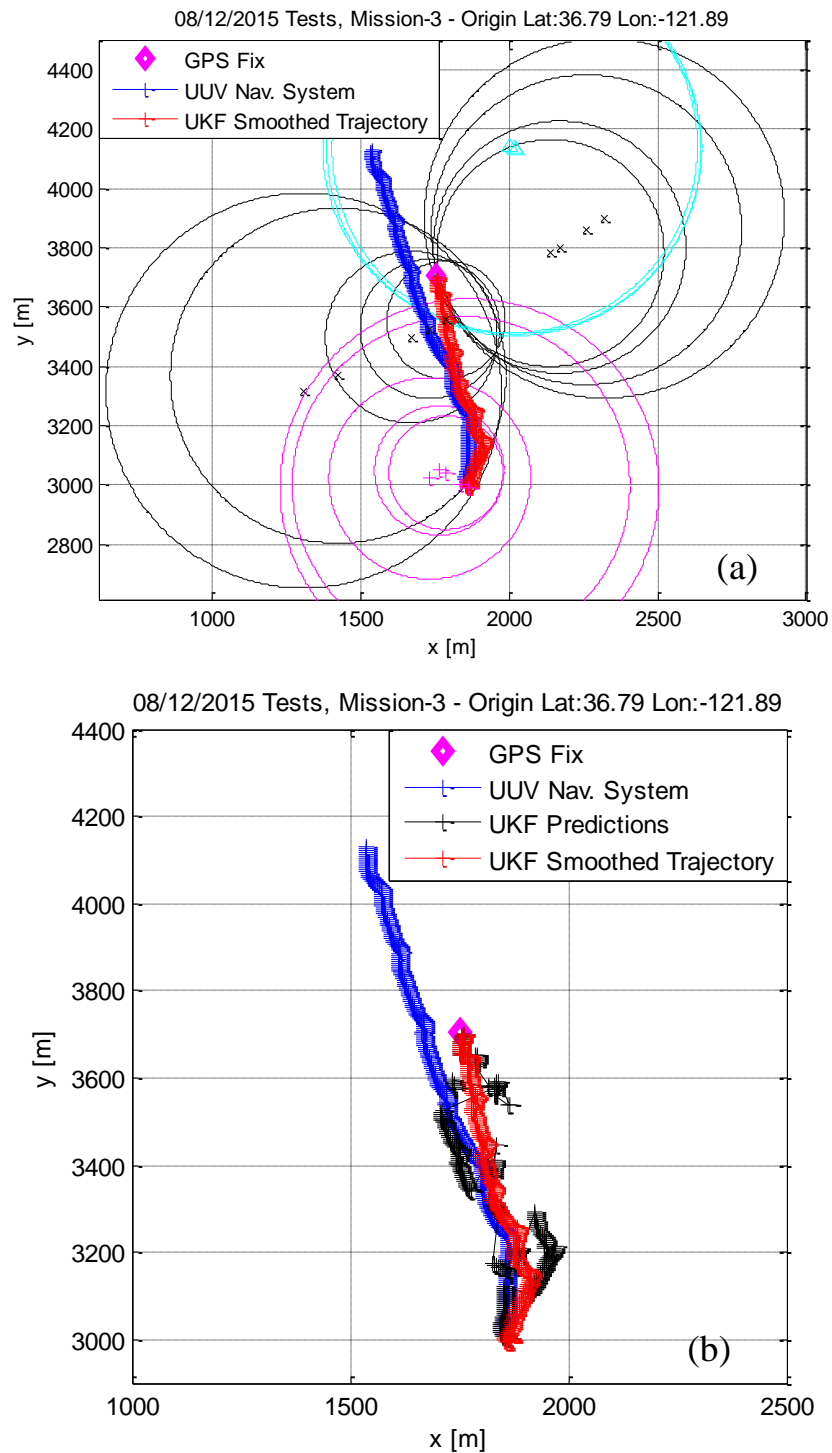
Figure 72.   Mission-3, Results after Automatic Tuning

121
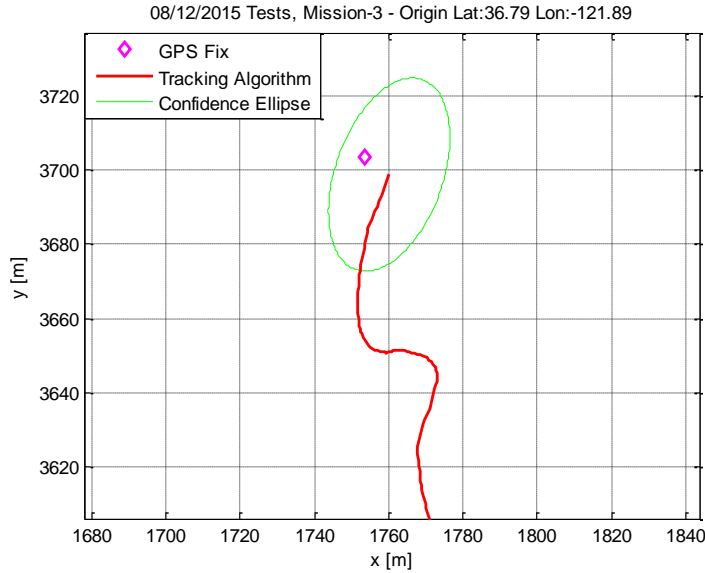
Figure 73.   Mission-3, Confidence Ellipse at the End of the Mission

The optimum tuning parameters for this mission are shown in Table 5. As can be seen, probably due to the more consistent measurement, the parameter $\sqrt{R}$ is in reasonable levels.

Table 5.   Mission-3, Optimum Tuning Parameters for Input Data Estimated According to Chapter IV, Section B.2.d

Tuning Parameters	
α	1.42×10^{-2}
β	3.41
κ	1.53×10^{-3}
q [m^2/s^3][a]	1×10^{-4}
$\sqrt{R}$ [m^2]	6.7

α, β, and κ have no dimensions;

[a] Units according to [38].

For this mission, tracking by dead reckoning (UUV navigation system) yielded an error of 476 meters (see Figure 70). The tracking algorithm was tested and the results show a more reliable predicted position for the entire UUV trajectory (see Figure 72). When a rough estimate for the distances was used, an error of 10.3 meters was observed

at the end of the mission. While this is a significant improvement over the UUV's estimated position, it is based on simple straight line propagation that does not account for the refractive and multipath effects of the environment (Figure 74).

When the more complete algorithm described in Chapter IV is used, the tracking algorithm produces an error of 8.6 meters at the end of the mission (as represented in Figure 73, there are uncertainties associated with the predictions). It's a small improvement in this case but still indicates that correlating the measured impulse response of the channel with a ray trace prediction may provide an improvement in the tracking accuracy.

Table 6.   Mission-3 Tracking Comparison

| Mission-3	Distances according to Chapter IV	Distances roughly estimated
Objective Function [m^4]	1145	1742
Error at beginning of the Mission [m]	2.45	3.10
Error at end of the Mission [m]	8.60	10.3
Total Error [m]	11.1	13.4
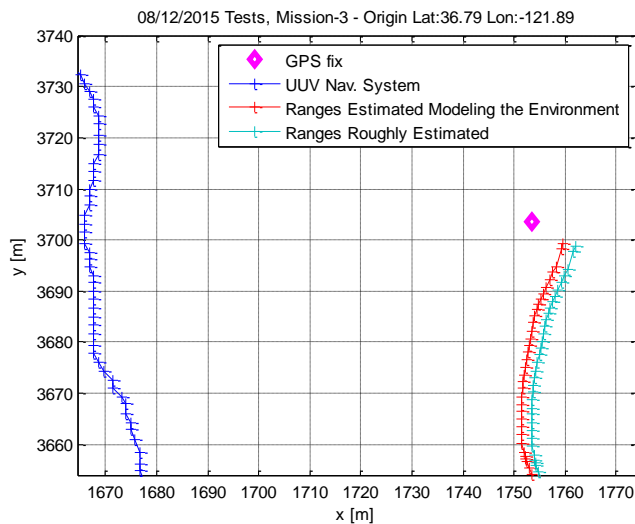
Figure 74.   Mission-3, Tracking Results when Processing the Distances Estimated According to Chapter IV and when Processing the Distances Roughly Estimated

The sea current predicted by the tracking algorithm for this mission is 0.34 knots (i.e., the average of the smoothed predictions) and has a general direction as represented in Figure 75a. It is worth noting the evolution of the tide during the mission period (see Figure 75b).
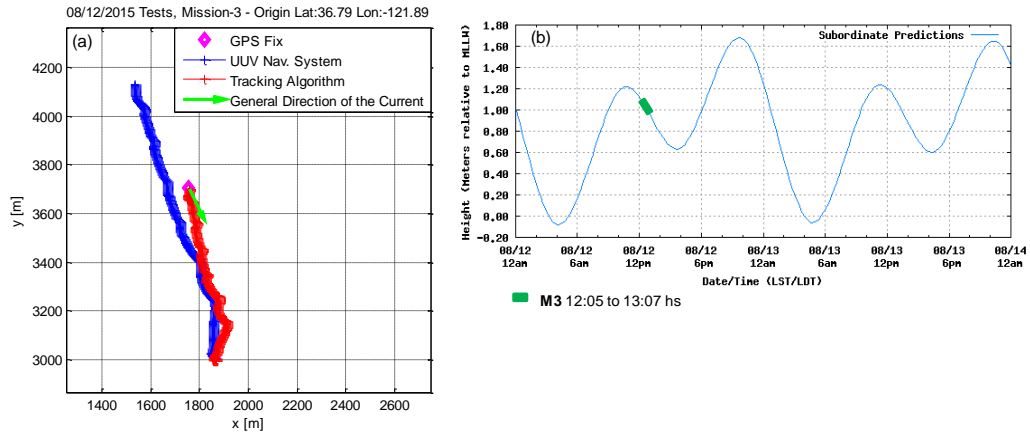

Figure 75.   Mission-3, Tracking, Sea Current, and Tide

D.   GENERAL REMARKS ON TRACKING RESULTS

In this section, a basic check of the corrections provided by the matched peak IR algorithm is made. Additionally, a discussion about the optimum tuning parameters and about the estimated sea currents is provided.

1.   Distance Corrections

In the beginning of this chapter, the term *distance roughly estimated* was defined as being the result of the multiplication of the one-way travel time by the characteristic medium sound speed, corrected by the assets' depth (horizontal distance). Let us define the term *correction* as the difference between the distance roughly estimated and the distance estimated using the approach defined in Chapter IV. Table 7 summarizes the amount of *correction* in each of the UUV's missions.

Table 7.   Summary of the Corrections on the UUV's Mission

	Number of Measurements (NM)	Number of Measurements with *corrections* > 5 m (NM5)	Ratio NM5/NM	Average Correction [m]
Mission-1	40	30	75.0%	9.4
Mission-2	11	6	54.5%	7.9
Mission-3	18	7	38.9%	4.0

From Table 7, it can be seen in mission-1 that 75% of the measurements had a correction greater than 5 meters and the average correction was 9.4 meters. Other missions show smaller numbers. The reason for the difference between missions may be explained in the following manner.

When the UUV is close to a reference point and operating at greater depths, the direct path generally produces a strong first arrival. Therefore, the algorithm may produce a small correction. On the other hand, when the UUV is far from the reference point and operating at shallow depths, the bottom bounce path dominates and a weak first arrival is expected. Therefore, the algorithm may produce a larger correction.

The ratio *distance from the UUV to a reference point (distance)* over *UUV depth (depth)* can be used as an indicator for those situations. A smaller ratio represents a situation where the UUV is closer to a reference point and deep; therefore, small and less frequent corrections are expected. A larger ratio represents a situation where the UUV is farther from a reference point and shallow; therefore, larger and more frequent corrections are expected.

Table 8 represents the average horizontal distance between the UUV and the reference points when a travel time measurement is taken, and Table 9 represents the average UUV depth. Based on these tables, the average ratio *distance* over *depth* can be calculated.

The last column of Table 10 (supported by Tables 8 and 9) shows the ratio of the *average distance* over *depth*, when the travel time measurements were taken for each UUV mission. Mission-1 has the larger ratio, followed by mission-2 and mission-3, which means that larger and more frequent corrections are expected in mission-1,

followed by mission-2 and mission-3. This conclusion is supported by the data shown in Table 7.

Table 8.   Average Horizontal Distance from the UUV to the Reference Points when a Travel Time Measurement is Taken

	Avg. Horizontal Distance from UUV to R/V Fulmar [m] (DIS)	Avg. Horizontal Distance from UUV to WG Mako [m] (DIS)	Avg. Horizontal Distance from UUV to WG Tiburon [m] (DIS)	Avg. Hor. Dist. [m] (DIS_A)
Mission-1	826	594	---	797
Mission-2	610	840	252	497
Mission-3	432	628	441	504

Table 9.   Average UUV Depth when a Travel Time Measurement is Taken

	Avg. UUV depth when a measurement is taken to R/V Fulmar [m] (DEPTH)	Avg. UUV depth when a measurement is taken to WG Mako [m] (DEPTH)	Avg. UUV depth when a measurement is taken to WG Tiburon [m] (DEPTH)	Avg. UUV depth when a measurement is taken [m] (DEPTH_A)
Mission-1	39.8	34.3	----	39
Mission-2	16.3	39.9	33.1	28.2
Mission-3	33.1	49.2	29.7	34.6

Table 10.   Ratio Average Horizontal Distance to a Reference Point over Average UUV Depth when a Travel Time Measurement is Taken

	Ratio DIS / DEPTH for R/V Fulmar	Ratio DIS / DEPTH for WG Mako	Ratio DIS / DEPTH for WG Tiburon	Ratio DIS_A / DEPTH_A
Mission-1	20.8	17.3	----	20.4
Mission-2	37.4	21.1	7.6	17.6
Mission-3	13.1	12.8	14.8	14.6

In Table 11, the time between the last travel time measurement and the UUV GPS fix at the end of the missions is shown. As can be seen, mission-3 has the larger number. This larger time difference, together with the reduced number of measurements, account

for the larger confidence ellipse associated with the last position prediction, in comparison with the previous missions.

Table 11.   Time between the Last Measurement and the UUV GPS Fix
at the End of the Missions

	Time between last measurement and GPS fix [mm:ss]
Mission-1	5:43
Mission-2	2:21
Mission-3	6:37

2.   The Tuning Parameters

The tuning parameters for the UKF-based tracking algorithm can be divided into two groups. The first group is composed of the hyper-parameters α, β, and κ, appearing exclusively in UKF applications. The second group, common to all KF applications, is composed of the matrices **R** and **Q**, representing the covariance of the measurement and covariance of the plant noise (also known as process noise), respectively.

As can be seen in Chapter II, Equation (2.26), the measurements are scalar numbers, which makes **R** a scalar, too. The square root of the scalar R represents the uncertainty associated with the measurements and, in our application, it combines the uncertainties in the estimated horizontal distances and in the position of the reference points (in x and y). The structure of the covariance matrix **Q** is shown in Chapter V, Equation (5.26), where q is used for tuning.

The hyper-parameters α, β, and κ are scalars numbers where α and κ determine the spreading of the sigma points around the predictions (mean) and β is used to incorporate prior information about the non-Gaussian distribution of the predicted states (β is set to 2 to model Gaussian distributions).

Table 12 shows the optimum tuning parameters for all three UUV missions. As can be seen, the parameters vary from mission to mission and, as expected, there is no one set of tuning parameters that works universally. What draws our attention are the large variations between missions. Those variations cannot be attributed only to changes, such as noise and sea state, in the environment.

The problem solved by the tracking algorithm is, essentially, a triangulation problem that consists of range-only measurements not taken simultaneously. As is common in triangulation problems, the number of reference points, their relative positions with respect to the UUV, and the number of measurements all influence the tracking dynamics and performance.

As seen in Figures 60a, 66a, and 72a, the relative position between assets and the measurement dynamics are very different when the missions are compared. Those differences may be considered the major factor for large variations in the tuning parameters, as shown in Table 12.

Simulation shows that when the measurements are consistent and in large numbers, the influence of the asset's relative position on the tuning parameters is reduced. In this situation the tuning parameters for different geometries tends to agree, which could indicate that real-time tracking is still a possibility. Although, as shown in this chapter, with a reduced number of measurements, post processing represents the best choice to reconstruct the UUV trajectory.

Table 12.   Summary of the Tuning Parameters

Optimum Tuning Parameters			
	Mission-1	**Mission-2**	**Mission-3**
α	1.08×10^{-1}	3.05×10^{-1}	1.42×10^{-2}
β	3.82	8.98×10^{-2}	3.41
κ	2.03×10^{-9}	9.4×10^{-3}	1.53×10^{-3}
$q \ [m^2/s^3]$ [a]	2.09×10^{-3}	1.11×10^{-3}	1×10^{-4}
$\sqrt{R} \ [m^2]$	4.65×10^5	10	6.7

α, β, and κ have no dimensions; [a] Units according to [38]

128

3. Sea Current

The tracking errors at the end of the missions, as well as the average predicted sea current, are presented in Table 13. As can be seen, there is a correlation between current and the errors, where higher currents are associated with higher errors. This problem is common to all underwater navigation systems that are not able to estimate or measure the sea current.

Some UUVs, equipped with Doppler velocity logs, have very successful results measuring the sea current by tracking its motion with respect to the bottom [53]. Unfortunately this method does not work for deeper waters (300 m and beyond). Research in the area of sea current estimation and measurement is growing very fast and some are leaning towards KF techniques, as used in this work [54], [55].

Table 13.   Summary of Mission Errors and Average Sea Current

	Approximated Distance Traveled (D) [m]	Final Trajectory Error (E) [m]	E /D	Predicted Average Current [knots]
Mission-1	1400	1095	0.78	0.60
Mission-2	1000	747	0.75	0.45
Mission-3	770	476	0.62	0.34

a. General Direction of the Sea Current

In an open area, where the direction of the water flow is not restricted by any barriers, the tidal current is rotary (i.e., clockwise in the northern hemisphere), flowing continuously throughout all points of the compass, with speeds usually varying during the tidal cycle [56]. The changes in direction and speed may be represented by arrows and generally have an elliptical pattern. On the other hand, in rivers or straights the current flows in approximately opposite directions with speed changing throughout the tidal cycle from zero to a maximum.

As can be seen in Figure 19, the area of operation is not exactly open and at the same time is not extremely restricted as in a straight or river. Therefore, some influence of the canyon (due its proximity) and of the geographical shape of the bay may be

129

expected. The tracking algorithm predictions for sea current and the tide information, for all three missions, are summarized in Figures 76 and 77.

In Figure 77 it can be seen that mission-1 took place on one side of the tide and missions 2 and 3 on the other side. The change in direction is clockwise and smooth from mission-2 to mission-3 (as expected for an open area), but drastic from mission-1 to mission-2. This drastic change in direction may be caused by the change in tide from flood to ebb associated with some influence of the canyon and the bay's geographical shape.
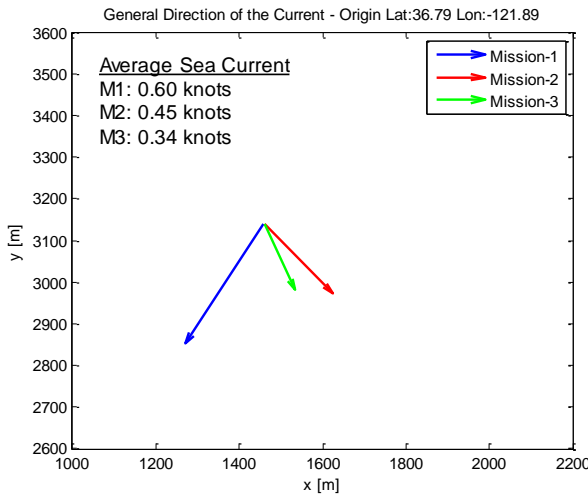
Figure 76.   General Direction of the Sea Current for the Three UUV Missions
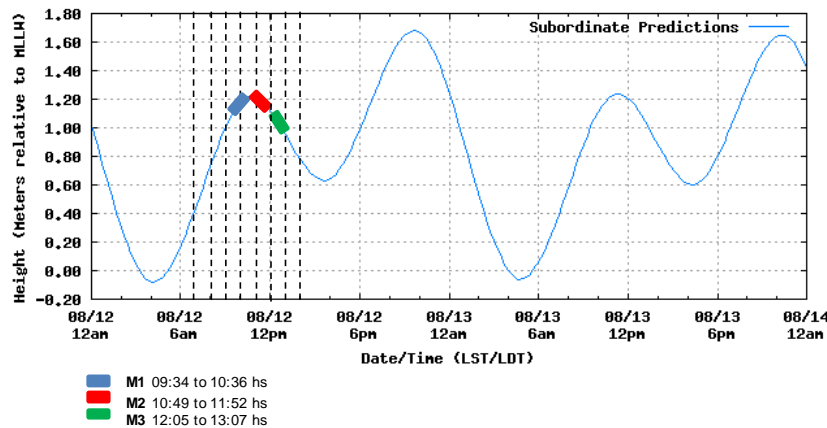
Figure 77.   Tide Evolution during the UUV Mission

130

b. Initialization of the Tracking Algorithm with Previous Knowledge of the Current

Let us consider a situation in which a UUV has previous knowledge of the sea current. We could imagine the scenario described in Chapter V, Section G, where a fleet of UUVs is able to transmit to the Command Center (via surface assets) their predictions for the sea current, and the Command Center (running the consensus current algorithm) broadcasts back to the UUVs the CSC. As an example, let us consider the data from mission-2.

When mission-2 is started, the UUV knowing the CSC, initializes its tracking algorithm with this information. As the first measurement did not happen until the middle of the mission, the initial predictions considering previous knowledge of the current may be improved. As can be seen in Figures 78 and 79, comparing the black and the green curves before the first measurement (first "jump"), the non-smoothed tracking in green is more consistent with the final result (smoothed trajectory in red) than the black curve where no previous knowledge of the current was assumed.

For this particular case, due to the geometry involved (relative position of the UUV and the surface assets) and due to the limited number of measurements, the final result was not affected by the initial assumption for the current. In a different scenario, however, the initial knowledge of the current may improve the overall performance of the tracking algorithm or, at least, provide a faster convergence to the true trajectory.
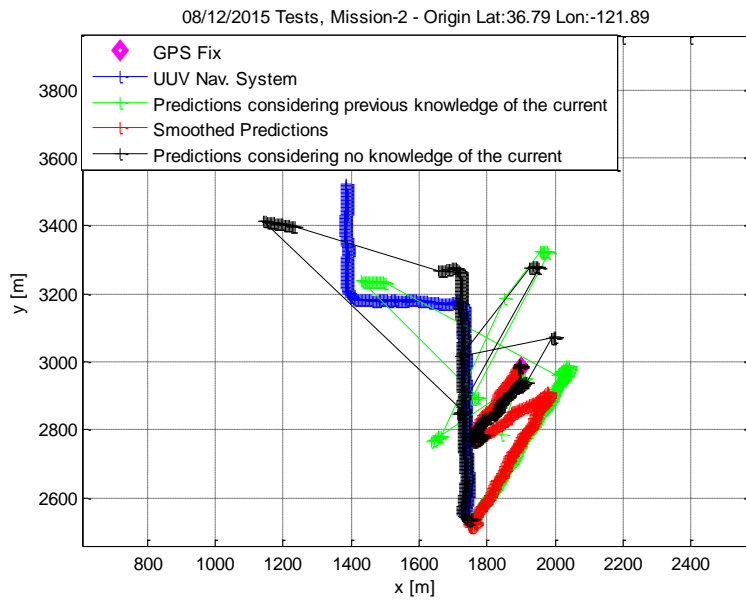
Figure 78. Tracking Considering a Previous Knowledge of the Sea Current
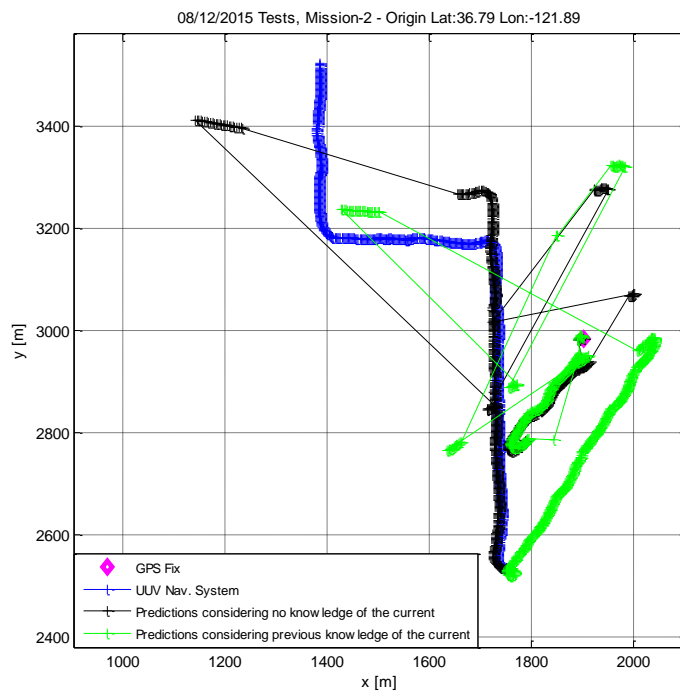
Figure 79. Tracking Considering a Previous Knowledge of the Sea Current,
Alternative View

132

VIII. CONCLUSION

Parts of this chapter were previously published by IEEE [1].*

How can a UUV be kept underwater for longer periods while maintaining accurate positioning? This is a question that this dissertation intended to address. This problem arises due to the nature of underwater navigation where GPS signals (or similar) and other navigation aids are not available.

Underwater navigation typically relies on automatic dead reckoning, gathering information from several sensors. Some systems count on lower error, expensive inertial sensors and others rely on simple magnetic compasses and speed estimates. Independent of how complex the system is, errors accumulate over time and may lead to unacceptable position uncertainties. Therefore, a position update from an external reliable source is a real necessity.

As pointed out in the Chapter I, by surfacing, the UUV can get a position update using its GPS. But this can introduce delays in the UUV's mission. Updating the UUV's position while it is underwater during the course of its mission may reduce the delays, permitting longer missions while maintaining position accuracy.

State-of-the-art techniques estimate a UUV's position by measuring its distance, and in some systems, its bearing to a reference point (or more than one) located at the surface or sea floor where, generally, the reference points—as well as the UUV—are slow moving (or static). By measuring the travel time of an acoustic wave, a system can estimate the distance (and in more advanced systems the bearing, too) and the UUV position can be determined and updated.

This approach is used in systems such as SBL, LBL, USBL, GIB, and some hybrid systems based on the previous ideas. Those systems are reliable when the depth

---

being explored is on the order of or larger than the horizontal distances between the assets.

As shown in Chapter IV, estimation of horizontal distances in relatively shallow water is a difficult task mainly due to the multipath nature of the propagation. Multiple arrivals reach the receiver at different times by different propagation paths, making it difficult to estimate accurately the travel time of the acoustic signals and, consequently, the distance. Some of the systems described earlier are able to account for the refraction of the sound waves when the sound speed profile is available, but none of them provides a solution to treat the errors caused by the multipath in their distance estimations.

Due to their relative low cost, compact design, and reliability, we are relying on battery powered DSP-based acoustic modems that make use of acoustic communication protocols to measure the acoustic wave travel time from the UUV to the reference points (Chapter IV, Section A). Chapter III presents the theoretical bases for wave travel time measurements and the main characteristics of the waveforms used for this task were highlighted.

Based on the travel times measured by the acoustic modems, we developed an algorithm to take into account the multipath and the refraction of the sound waves when estimating distances underwater (Chapter IV, Section B). This algorithm makes use of a ray tracing code to model the environment and an iterative routine to match measurements with synthetic predictions. The whole process is designed to take just a few seconds to converge to a solution, making it appropriate for real-time applications. This approach is a unique contribution of this dissertation.

At this point, using the estimated distances and the coordinates of the reference points, we may establish the UUV position. To accomplish this, it was necessary to develop a tracking algorithm to fuse all available data (i.e., UUV navigation data, reference points' coordinates, and distances from the UUV to the reference points). This was done using KF techniques.

A model for the UUV based on the state space representation was developed in Chapter II, taking into account the two main characteristics of our acoustic modems:

134

inability to take simultaneous measurements to different reference points and lack of bearing (direction) measurement associated with the travel time.

The aforementioned modem's characteristics produce a non-linear measurement equation that was treated using two different approaches: a linearization by Taylor series expansion as in the EKF, and a statistical linearization based on what are called "sigma points," as in the UKF. To produce realistic trajectories, mainly when the number of measurements is limited and during the transient portion of the tracking, a smoothing algorithm had to be used, and the equations are presented in Chapter V, Section F.

Another important part of the tracking algorithm is the choice for the tuning parameters. In Chapter V, Section E, an algorithm was presented to select the optimum tuning parameters automatically for a given set of data (training data). This algorithm used the UKF (or EKF) to construct a cost function and optimization techniques to find the best (or optimum) set of tuning parameters that minimized (or maximized) the cost function.

To account for the drift in the UUV trajectory caused by the sea current, it was modeled as a random walk and was part of the state of the system. In a scenario described as a multi-UUV centralized network (Chapter V, Section G), the predictions for the sea current coming from the UUVs are concentrated in the command center, where an algorithm processing this data tries to establish a consensus current. When the results of the algorithm converge, the CSC is achieved and may be used in several different ways as described in Chapter V, Section G.

At this point, one can see that it was necessary to put together tools already available as well as to make new developments to respond to the short, but not easy, question posed in the beginning of this chapter. The first test for this whole package was the processing of synthetic data.

In Chapter VI a scenario in which two UUVs navigating in an area where three surface assets are present was emulated. The surface assets were assumed to have access to GPS and were able to share information with the shore-based command center via satellite, permitting evaluation of the consensus current algorithm.

Three distinct cases were simulated. The first was the ideal case in which all the measurements were successful, and no noise was present. The second case considered failure in the measurements during a certain portion of the UUV's mission. In the third, noise was added to the previous case. Results showed the importance of the smoothing algorithm to produce realistic trajectories and highlighted that the UKF produced faster convergence and better behavior in the presence of noise. The consensus current algorithm proved converging in all three cases with faster convergence and smoother profiles when UKF was used.

To validate the developed algorithms, real data collected during the sea tests that took place in Monterey Bay on August 2015 was processed (Chapter VII). In a one-week sea test, two Liquid Robotics Wave Gliders (USVs) and a command ship, all equipped with Teledyne-Benthos acoustic modems (ATM-900 series) and GPS connectivity, formed a network of reference points for an Exocetus Coastal Glider (UUV), also equipped with the same type of acoustic modem. On three (one-hour long) UUV missions, successful data was recorded.

During the course of mission-1, 40 measurements from the UUV to the reference points were recorded. The measurements were taken in an inconsistent manner and to only two of the three reference points. After running the automatic tuning algorithm, the optimum value for the parameter $\sqrt{R}$ was very high (see Table 1). This parameter combines the uncertainties associated with the distances between UUV and the reference points, and the uncertainties in the position of the reference points (in x and y).

A large $\sqrt{R}$ indicates a non-reliable or, in this case, inconsistent measurement. The geometry (i.e., the relative position between assets), the large period of time with measurements to only one reference point, and measurements to only two reference points may be causing a high $\sqrt{R}$ (see Figure 59).

In mission-2 and mission-3 fewer measurements were recorded, but they were recorded in a more consistent way and for all the three surface assets (see Figures 65 and 71). That may be the cause of the reduction in the tuning parameter $\sqrt{R}$ (chosen by the automatic tuning algorithm) to reasonable levels (see Table 12).

As seen in mission-1, the GPS fixes for mission-2 and mission-3, that were recorded as soon as the UUV surfaced, are located inside the uncertainty ellipses associated with the last tracking algorithm prediction. It is also worth noting that those ellipses have realistic dimensions (see Figures 61, 67, and 73).

Table 12 showed the optimum tuning parameters for all three UUV missions. In this table, unexpected large differences between missions can be seen. Those differences may be primarily attributed to different geometries (i.e., the relative positioning between assets) and a different dynamic in the measurements (i.e., the time between measurements, total number of measurements, and number of reference points available).

Simulation showed that when the measurements are consistent and in large numbers, the influence of the asset's relative position on the tuning parameters is reduced. In this situation the tuning parameters for different geometries tends to agree, which could indicate that real-time tracking is still a possibility. Although with a reduced number of measurements, post processing represents the best choice to reconstruct the UUV trajectory.

Another interesting point emerged from the predictions for the sea current. Those predictions for all three missions are depicted in Figure 76 (as the average of the smoothed predictions) as well as the evolution of the tide in Figure 77. Note that mission-1 took place on one side of the tide and missions 2 and 3 on the other side. The drastic change in the direction of the current occurred from mission-1 to mission-2 (and mission-3) may be explained by the change in tide from flood to ebb associated with some influence of the canyon and the bay's geographical shape.

Finally, to point out the possible benefits of the CSC, data from mission-2 was used in a scenario that simulated a broadcast of the CSC to all UUVs in a certain area. Results showed that previous knowledge of the current may improve the tracking, mainly in the portion where few measurements are available.

Despite these promising results, improvements can be made in several parts of the system, including:

- Measuring the beam patterns of the acoustic modem's transducers when they are mounted in their respective structures and including this measurement in the modeling of the system;

- Improving the corrections for the displacement between the GPS antenna and the acoustic modem transducer on the Wave Gliders;

- Reducing, on the Wave Gliders, the time between GPS fixes to avoid the use of interpolation to establish their position during the measurements;

- Accounting for the variability in the sound speed profile measured by the UUV.

Continuing with a measurement system able to provide range only, a study of the optimum tuning parameters for different geometries, measurement dynamics, ambient noise, and sea states is an interesting topic for future work. Along this line of thought, different trajectories taken by a mobile reference point could be explored.

Although representing a very interesting topic, the natural evolution of this research points to the use of directional acoustic modems. This equipment, available off the shelf, is able to provide a bearing associated with the travel time and basically has the same dimensions and weight as the non-directional version.

The use of directional modems may reduce the number of reference points to, in theory, only one. It will eliminate the influence of different geometries and measurement dynamics in the optimum tuning parameters, although ambient noise and sea state may still affect them.

APPENDIX A. MATCHED FILTER OUTPUT FOR LFM AND HFM PULSES IN THE PRESENCE OF DOPPLER EFFECT

The purpose of this appendix is to demonstrate how the relative motion between source and target can affect the matched filter output for LFM and HFM pulses.

A.   LFM PULSES

Let us start with the evaluation of the Fourier transform of the rectangular-envelope LFM pulse.

1.   Fourier Transform

Let us start with the rectangular-envelope LFM pulse in complex notation

$$x(t) = A\, rect\left(\frac{t}{T}\right) e^{j\left(2\pi f_c t + D_p t^2\right)}, \tag{A.1}$$

where $D_p \triangleq \pm \dfrac{\pi}{T} B$, and $rect\left(\dfrac{t}{T}\right) = 1$ for $|t| \leq T/2$. The Fourier transform of $x(t)$ is

$$X(f) = \int_{-\infty}^{\infty} A\, rect\left(\frac{t}{T}\right) e^{j\left(2\pi f_c t + D_p t^2\right)}\, e^{-j 2\pi f t} dt. \tag{A.2}$$

Rearranging the terms in Equation (A.2), we obtain

$$X(f) = \int_{-\infty}^{\infty} \underbrace{A\, rect\left(\frac{t}{T}\right)}_{A(t)} e^{j\overbrace{\left(2\pi(f_c - f)t + D_p t^2\right)}^{\phi(t)}} dt. \tag{A.3}$$

To evaluate Equation (A.3) the method of stationary phase [14], [57], and [58] is used. The method of stationary phase is useful to make approximations for integrals with highly oscillatory integrands. The stationary phase point is defined such that the first time derivative of the phase in Equation (A.3) is set to zero, $\phi'(t_o) = 0$. Then the approximation of the integral of Equation (A.3) is [14]

$$X(f) \approx \sqrt{\frac{-2\pi}{\phi''(t_o)}}\, e^{-j\frac{\pi}{4}} A(t_o)\, e^{j\phi(t_o)}. \tag{A.4}$$

The integrand phase and its derivatives are

139

$$\phi(t) = 2\pi(f_c - f)t + D_p t^2$$
$$\phi'(t) = 2\pi(f_c - f) + 2D_p t \quad \text{(A.5)}$$
$$\phi''(t) = 2D_p .$$

The stationary phase point is defined by

$$2\pi(f_c - f) + 2D_p t_o = 0$$
$$t_o = \frac{\pi}{D_p}(f - f_c). \quad \text{(A.6)}$$

Using the definition of D_p and defining $k = B/T$, we can write

$$t_o = \frac{1}{k}(f - f_c). \quad \text{(A.7)}$$

Using the definitions of $A(t)$ and $\phi(t)$ from Equation (A.3) and substituting Equation (A.7) into Equation (A.4), we obtain

$$X(f) \approx A\sqrt{\frac{T}{B}}\ e^{j\frac{\pi}{4}}\ rect\left(\frac{f - f_c}{B}\right) e^{-j\left[\frac{\pi}{k}(f - f_c)^2\right]}. \quad \text{(A.8)}$$

Equation (A.8) is the approximate Fourier transform of the rectangular-envelope LFM pulse by means of the stationary phase method. This result will be used next, in the evaluation of the matched filter output.

2.   Matched Filter Output in the Presence of Doppler Effect

The following development is based on the methodology described by Minkoff [17]. Re-stating Chapter III, Equation (3.17), the Doppler transformed received signal is

$$x'(t) = x(\alpha t - \tau_o), \quad \text{(A.9)}$$

where $x(t)$ is the transmitted signal, τ_o is the two-way travel time, and $\alpha \approx 1 - \frac{2v_r}{c}$. Worth noting that v_r is the relative radial speed between source and target as described in Chapter III, section B.1.

The output of a filter matched to the transmitted signal $x(t)$ is

$$y(t) = x(\alpha t - \tau_o) * x^*(-t), \quad \text{(A.10)}$$

where, in Equation (3.6), t_o was set to zero and K to 1.

Defining

$$Y(f) = \mathbb{F}\{x(\alpha t - \tau_o) * x^*(-t)\}$$

$$Y(f) = \frac{1}{|\alpha|} X\left(\frac{f}{\alpha}\right) e^{-j2\pi\frac{f}{\alpha}\tau_o} X^*(f). \tag{A.11}$$

Therefore

$$y(t) = \int_{-\infty}^{\infty} \overbrace{\frac{1}{|\alpha|} X\left(\frac{f}{\alpha}\right) e^{-j2\pi\frac{f}{\alpha}\tau_o} X^*(f)}^{Y(f)} e^{j2\pi ft} \, df. \tag{A.12}$$

Using Equations (A.8) and (A.12), the matched filter output for the rectangular-envelope LFM pulse is

$$y(t) = \frac{A^2}{\alpha} \frac{T}{B} \int_{-\infty}^{\infty} rect\left(\frac{f/\alpha - f_c}{B}\right) rect\left(\frac{f - f_c}{B}\right) e^{-j2\pi\frac{f}{\alpha}\tau_o} e^{-j\left\{\frac{\pi}{k}\left[(f/\alpha - f_c)^2 - (f - f_c)^2\right]\right\}} e^{j2\pi ft} \, df, \tag{A.13}$$

where α is always positive.

The exponential that contains the quadratic terms may be simplified as

$$e^{-j\left\{\frac{\pi}{k}\left[\underbrace{(f/\alpha - f_c)^2}_{a^2} - \underbrace{(f - f_c)^2}_{b^2}\right]\right\}}$$

$$a^2 - b^2 = (a+b)(a-b) \tag{A.14}$$

$$e^{-j\left\{\frac{\pi}{k}\left[f^2\left(\frac{1-\alpha^2}{\alpha^2}\right) - 2f_c f\left(\frac{1-\alpha}{\alpha}\right)\right]\right\}}.$$

The term that contains α^2 in (A.14) may be simplified as

$$\frac{1-\alpha^2}{\alpha^2} = \frac{1 - \left(1 - \frac{2v_r}{c}\right)^2}{\left(1 - \frac{2v_r}{c}\right)^2} = \frac{\frac{4v_r}{c} - 4\left(\frac{v_r}{c}\right)^2}{1 - \frac{4v_r}{c} + 4\left(\frac{v_r}{c}\right)^2}. \tag{A.15}$$

Considering that $c \gg v_r$ the quadratic terms in (A.15) may be ignored and the term $1 - \frac{4v_r}{c} \approx 1$. Rewriting (A.15) yields

$$\frac{1-\alpha^2}{\alpha^2} \approx \frac{4v_r}{c}. \tag{A.16}$$

Appling the same reasoning in $\frac{1-\alpha}{\alpha}$, we obtain

141

$$\frac{1-\alpha}{\alpha} \approx \frac{2v_r}{c} . \tag{A.17}$$

Substituting (A.16) and (A.17) into (A.14) we obtain

$$e^{-j\pi\frac{4v_r}{c}\left[\frac{f^2}{k}-\frac{f_c f}{k}\right]} = e^{-j\pi\frac{4v_r}{c}\left[\frac{(f-f_c)^2}{k}+\frac{f_c f}{k}-\frac{f_c^2}{k}\right]}$$

$$= e^{-j\left[\frac{\pi 4v_r}{c}\frac{(f-f_c)^2}{k}-2\pi f_d\frac{f}{k}-\frac{\pi 4v_r}{c}\frac{f_c^2}{k}\right]} . \tag{A.18}$$

Now, for further simplification in Equation (A.25), let us assume that $f_d \approx \frac{f_d}{\alpha}$,

and separating the constant term $\frac{\pi 4v_r}{c}\frac{f_c^2}{k}$, the exponential becomes

$$e^{-j\left[\frac{\pi 4v_r}{c}\frac{(f-f_c)^2}{k}-2\pi\frac{f_d}{\alpha}\frac{f}{k}\right]}e^{j\left(\frac{\pi 4v_r}{c}\frac{f_c^2}{k}\right)} . \tag{A.19}$$

Substituting (A.19) into Equation (A.13) yields

$$y(t) = \frac{A^2}{\alpha}\frac{T}{B}e^{j\left(\frac{\pi 4v_r}{c}\frac{f_c^2}{k}\right)}\int_{-\infty}^{\infty} rect\left(\frac{f/\alpha-f_c}{B}\right)rect\left(\frac{f-f_c}{B}\right)e^{-j\left[\frac{\pi 4v_r}{c}\frac{(f-f_c)^2}{k}-2\pi\frac{f}{\alpha}\left(\frac{f_d}{k}-\tau_o\right)\right]}e^{j2\pi ft}\,df . \tag{A.20}$$

Rearranging the terms and rewriting Equation (A.20), we obtain

$$y(t) = A^2\sqrt{\frac{T}{B}}\,e^{j\left(\frac{\pi 4v_r}{c}\frac{f_c^2}{k}\right)}\mathbb{F}^{-1}\left\{\underbrace{\sqrt{\frac{T}{B}}rect\left(\frac{f-f_c}{B}\right)e^{-j\left[\frac{\pi 4v_r}{c}\frac{(f-f_c)^2}{k}\right]}}_{A(f)}\underbrace{\frac{1}{\alpha}rect\left(\frac{f/\alpha-f_c}{B}\right)e^{j2\pi\frac{f}{\alpha}\left(\frac{f_d}{k}-\tau_o\right)}}_{B(f)}\right\} .$$

$$\tag{A.21}$$

Equation (A.21) may be written as

$$y(t) = A^2\sqrt{\frac{T}{B}}\,e^{j\left(\frac{\pi 4v_r}{c}\frac{f_c^2}{k}\right)}\left[a(t)*b(t)\right], \tag{A.22}$$

where $a(t) = \mathbb{F}^{-1}\left\{A(f)\right\}$ and $b(t) = \mathbb{F}^{-1}\left\{B(f)\right\}$.

Referring to Equations (A.1) and (A.8)

$$rect\left(\frac{t}{T}\right)e^{j\left(2\pi f_c t + D_p t^2\right)} \xleftrightarrow{\ \mathbb{F}\ } \sqrt{\frac{T}{B}}\,e^{j\frac{\pi}{4}}\,rect\left(\frac{f-f_c}{B}\right)e^{-j\left[\frac{\pi}{k}(f-f_c)^2\right]} . \tag{A.23}$$

142

Therefore

$$a(t) = \left(\sqrt{\frac{4v_r}{c}} e^{j\frac{\pi}{4}} \right) rect\left(\frac{t}{T'} \right) e^{j\left(2\pi f_c t + D_p' t^2 \right)}, \tag{A.24}$$

where $T' = \frac{4v_r}{c} T$ and $D_p' = \pi \frac{c}{4v_r T} B$,

and

$$b(t) = \int_{-\infty}^{\infty} rect\left(\frac{f/\alpha - f_c}{B} \right) e^{j2\pi \frac{f}{\alpha}\left(\frac{f_d}{k} - \tau_o \right)} e^{j2\pi ft} \frac{df}{\alpha}. \tag{A.25}$$

Defining the following variables

$$f' = \frac{f}{\alpha} - f_c \Rightarrow f = \alpha\left(f' + f_c \right)$$
$$\frac{df}{\alpha} = df'. \tag{A.26}$$

Substituting (A.26) into (A.25) and rearranging the terms yields

$$b(t) = e^{j2\pi f_c\left(\frac{f_d}{k} - \tau_o + \alpha t \right)} \int_{-\infty}^{\infty} rect\left(\frac{f'}{B} \right) e^{j2\pi\left(\frac{f_d}{k} - \tau_o + \alpha t \right) f'} df'. \tag{A.27}$$

Solving Equation (A.27), using the Euler identity $e^{j\theta} - e^{-j\theta} = 2j\sin\theta$, and using

$$\text{sinc}(x) = \frac{\sin(\pi x)}{\pi x}$$

$$b(t) = B\, e^{j2\pi f_c\left(\frac{f_d}{k} - \tau_o + \alpha t \right)} \text{sinc}\left[B\left(\frac{f_d}{k} - \tau_o + \alpha t \right) \right]. \tag{A.28}$$

Substituting Equations (A.24) and (A.28) into (A.22) yields

$$y(t) = A^2 \sqrt{T'B}\; e^{j\left(\frac{\pi 4 v_r}{c} \frac{f_c^2}{k} \right)} \left\{ e^{j\frac{\pi}{4}} rect\left(\frac{t}{T'} \right) e^{j\left(2\pi f_c t + D_p' t^2 \right)} * e^{j2\pi f_c\left(\frac{f_d}{k} - \tau_o + \alpha t \right)} \text{sinc}\left[B\left(\frac{f_d}{k} - \tau_o + \alpha t \right) \right] \right\}. \tag{A.29}$$

Taking the absolute value of Equation (A.29), we obtain

$$|y(t)| = A^2 \sqrt{T'B}\left| rect\left(\frac{t}{T'} \right) e^{j\left(2\pi f_c t + D_p' t^2 \right)} * e^{j2\pi f_c \alpha t} \text{sinc}\left[B\left(\frac{f_d}{k} - \tau_o + \alpha t \right) \right] \right|. \tag{A.30}$$

Expanding Equation (A.30) in the convolution integral format results in

143

$$\left| y(t) \right| = A^2 \sqrt{T'B} \left| \int_{-\infty}^{\infty} e^{j2\pi f_c \alpha u} \, \text{sinc}\left[B\left(\frac{f_d}{k} - \tau_o + \alpha u \right) \right] rect\left(\frac{t-u}{T'} \right) e^{j\left[2\pi f_c(t-u) + D_p'(t-u)^2 \right]} du \right|. \quad \text{(A.31)}$$

Adding and subtracting αt in the first exponential and rearranging the exponential terms, we obtain

$$\left| y(t) \right| = A^2 \sqrt{T'B} \left| \int_{-\infty}^{\infty} e^{j2\pi f_c(\alpha u + \alpha t - \alpha t)} \, \text{sinc}\left[B\left(\frac{f_d}{k} - \tau_o + \alpha u \right) \right] rect\left(\frac{t-u}{T'} \right) e^{j\left[2\pi f_c(t-u) + D_p'(t-u)^2 \right]} du \right|$$

$$= A^2 \sqrt{T'B} \left| e^{j2\pi f_c t} \right| \left| \int_{-\infty}^{\infty} e^{\overset{\displaystyle j2\pi f_c (1-\alpha)(t-u)}{\underset{2v_r/c}{}}} \, \text{sinc}\left[B\left(\frac{f_d}{k} - \tau_o + \alpha u \right) \right] rect\left(\frac{t-u}{T'} \right) e^{jD_p'(t-u)^2} du \right|$$

$$= A^2 \sqrt{T'B} \left| \int_{-\infty}^{\infty} \text{sinc}\left[B\left(\frac{f_d}{k} - \tau_o + \alpha u \right) \right] rect\left(\frac{t-u}{T'} \right) e^{j\left[2\pi f_d(t-u) + D_p'(t-u)^2 \right]} du \right|.$$

(A.32)

Rewriting Equation (A.32) using the convolution representation, we arrive at

$$\left| y(t) \right| = A^2 \sqrt{T'B} \left| \text{sinc}\left[B\left(\frac{f_d}{k} - \tau_o + \alpha t \right) \right] * rect\left(\frac{t}{T'} \right) e^{j\left[2\pi f_d t + D_p' t^2 \right]} \right|. \quad \text{(A.33)}$$

Recognizing that the exponential in Equation (A.33) will vary little over time T' $\left(T' \ll T, \, f_d \ll f_c, \, and \, D_p' \ll D_p \right)$, we can write

$$\left| y(t) \right| \approx A^2 \sqrt{T'B} \left| \text{sinc}\left[B\left(\frac{f_d}{k} - \tau_o + \alpha t \right) \right] * rect\left(\frac{t}{T'} \right) \right|. \quad \text{(A.34)}$$

It is commonly accepted that the width of the convolution of two functions is nominally the sum of the widths of the two functions. Defining the width of the *rect* function as Δ_R, the width of the *sinc* function as Δ_S, and the width of matched filter output as Δ_T:

$$\Delta_T \approx \Delta_R + \Delta_S. \quad \text{(A.35)}$$

Since the first zero in the *sinc* function occurs when its argument goes to unity

$$B\left(\frac{f_d}{k} - \tau_o + \alpha \Delta_s \right) = \pm 1 \quad \text{(A.36)}$$

and

$$\Delta_s = \frac{1}{\alpha B} + \frac{\tau_o}{\alpha} - \frac{f_d}{k\alpha}. \quad \text{(A.37)}$$

144

The term $\dfrac{\tau_o}{\alpha} - \dfrac{f_d}{k\alpha}$ represents a partial temporal offset of the main lobe in the matched filter output. Therefore, the width due to the *sinc* function is $1/\alpha B$.

The width of the *rect* function is T', using Equation (A.24) yields

$$\Delta_R = \frac{4v_r}{c}T. \tag{A.38}$$

Substituting Equation (A.37) and (A.38) into Equation (A.35), we obtain

$$\begin{aligned}\Delta_T &\approx \frac{1}{\alpha B} + \frac{4v_r}{c}T = \frac{1}{B}\left[\frac{1}{\alpha} + \frac{4v_r}{c}TB\right] \\ &\approx \frac{1}{B}\left(1 + \frac{4v_r}{c}TB\right).\end{aligned} \tag{A.39}$$

From Equation (A.39) it can be seen that in a stationary source and target scenario, the nominal half-width of the main lobe in the matched filter output is $1/B$. Due to the Doppler effect, there is a widening in the main lobe that will be accompanied by a reduction in amplitude (due to conservation of energy), as can be seen in Chapter III, Figure 9. Additionally, there is a temporal offset in the matched filter output's peak that, for some applications, must be taken into account.

Depending on how severe the widening effect is, it may be necessary to use a "bank" of filters matched to different target speeds to permit target detection. According to Equation (A.39) the widening in the matched filter output is given by the factor $1 + (4v_r/c)TB$, and the range resolution is degraded by the same factor. Thus, if $(4v_r/c)TB \ll 1$ the widening and, consequently, the amplitude reduction in the matched filter output will not be extensive. Therefore, it may be written as

$$TB \ll \frac{c}{4v_r}. \tag{A.40}$$

Equation (A.40) states that if the signal's time bandwidth product is small in comparison with the ratio of medium sound speed over the maximum source-target radial speed, the widening effect in the matched filter output can be neglected.

At this point we may go back and revisit Equation (A.20):

$$y(t) = \frac{A^2}{\alpha} \frac{T}{B} \int_{-\infty}^{\infty} rect\left(\frac{f/\alpha - f_c}{B}\right) rect\left(\frac{f - f_c}{B}\right) e^{-j\left[\frac{\pi 4 v_r}{c}\frac{(f-f_c)^2}{k} - 2\pi\frac{f}{\alpha}\left(\frac{f_d}{k} - \tau_o\right)\right]} e^{j2\pi ft} \, df .$$

Based on the previous derivation and analyzing the exponential term, we may conclude that:

   a) The first term (quadratic), also called the dispersive term, is responsible for the widening in the matched filter output;

   b) The second term is responsible for the temporal offset in the matched filter output.

If we use a waveform such that the dispersive term is not present in the matched filter output, the widening effect as seen in the LFM pulse is not expected. With this in mind, next section presents the analysis for the rectangular-envelope HFM pulse.

B. HFM PULSES

Let us start with the evaluation of the Fourier transform of the rectangular-envelope HFM pulse.

1. Fourier Transform

The rectangular-envelope HFM pulse may be represented as [21]

$$x(t) = rect\left(\frac{t}{T}\right) \cos\left[\frac{2\pi}{\kappa} \ln\left(1 + \kappa f_o t\right)\right], \quad \kappa = \frac{f_o - f_{end}}{T f_o f_{end}} , \tag{A.41}$$

where $rect\left(\dfrac{t}{T}\right) = 1$ for $|t| \le T/2$; f_o and f_{end} are, respectively, the starting and the ending frequency; and T is the duration of the pulse.

In complex notation Equation (3.22) becomes

$$x(t) = A \, rect\left(\frac{t}{T}\right) e^{j\frac{2\pi}{\kappa}\ln(1+\kappa f_o t)} . \tag{A.42}$$

The Fourier transform of $x(t)$ is

$$X(f) = \int_{-\infty}^{\infty} A \, rect\left(\frac{t}{T}\right) e^{j\frac{2\pi}{\kappa}\ln(1+\kappa f_o t)} e^{-j2\pi ft} \, dt . \tag{A.43}$$

Rearranging the terms in Equation (A.43), we obtain

$$X(f) = \int_{-\infty}^{\infty} \underbrace{Arect\left(\frac{t}{T}\right)}_{A(t)} e^{j\underbrace{\left[\frac{2\pi}{\kappa}\ln(1+\kappa f_o t)-2\pi ft\right]}_{\phi(t)}} dt. \tag{A.44}$$

Applying the method of stationary phase gives us

$$X(f) \approx \sqrt{\frac{-2\pi}{\phi''(t_o)}}\, e^{-j\frac{\pi}{4}} A(t_o)\, e^{j\phi(t_o)}. \tag{A.45}$$

The integrand phase and its derivatives are

$$\phi(t) = \frac{2\pi}{\kappa}\ln(1+\kappa f_o t) - 2\pi ft$$

$$\phi'(t) = \frac{2\pi f_o}{1+\kappa f_o t} - 2\pi f \tag{A.46}$$

$$\phi''(t) = -\frac{2\pi \kappa f_o^2}{(1+\kappa f_o t)^2}.$$

The stationary phase point is

$$\frac{2\pi}{\kappa}\ln(1+\kappa f_o t_o) - 2\pi ft = 0$$

$$t_o = \frac{1}{\kappa}\left(\frac{1}{f} - \frac{1}{f_o}\right). \tag{A.47}$$

Using the definitions of $A(t)$ and $\phi(t)$ from Equation (A.44) and substituting Equation (A.47) into Equation (A.45), we obtain

$$X(f) = \frac{Ae^{-j\left(\frac{2\pi}{\kappa}+\frac{\pi}{4}\right)}}{\sqrt{\kappa}}\, rect\left[\frac{1/f-1/f_o}{B/f_o f_{end}}\right]\frac{1}{f}\, e^{j\frac{2\pi}{\kappa}\left[\ln(f_o/f)+f/f_o\right]}. \tag{A.48}$$

Equation (A.48) is the approximate Fourier transform of the rectangular-envelope HFM pulse by means of the stationary phase method. This result will be used next, in the evaluation of the matched filter output.

147

2. Matched Filter Output in the Presence of Doppler Effect

The following development is based on the methodology described by Minkoff [17]. Using Equations (A.48) and (A.12), the matched filter output for the rectangular-envelope HFM pulse is

$$y(t) = \frac{A^2}{\kappa} \int_{-\infty}^{\infty} rect\left[\frac{1/f - 1/f_o}{B/f_o f_{end}}\right] rect\left[\frac{\alpha/f - 1/f_o}{B/f_o f_{end}}\right] \frac{1}{f^2} e^{j\frac{2\pi}{\kappa}\left[\ln\alpha + \frac{f}{f_o}\left(\frac{1-\alpha}{\alpha}\right) - \kappa f\left(\frac{\tau_o}{\alpha} - t\right)\right]} df. \quad (A.49)$$

Making the following approximations yields

$$\ln\alpha = \ln\left(1 - \frac{2v_r}{c}\right), \quad for \; c \gg v_r \quad \ln\alpha \approx 0$$

$$rect\left[\frac{\alpha/f - 1/f_o}{B/f_o f_{end}}\right] \approx rect\left[\frac{1/f - 1/f_o}{B/f_o f_{end}}\right]. \quad (A.50)$$

Using (A.50) and rearranging the terms, Equation (A.49) becomes

$$y(t) = \frac{A^2}{\kappa} \int_{-\infty}^{\infty} \left\{ rect\left[\frac{1/f - 1/f_o}{B/f_o f_{end}}\right] \right\}^2 \frac{1}{f^2} e^{j2\pi f\left\{t - \frac{1}{\alpha}\left[\tau_o - \frac{(1-\alpha)}{\kappa f_o}\right]\right\}} df. \quad (A.51)$$

Because the phase of the exponential in (A.51) is linear in f, the dispersive term is not present. Therefore, the widening effect in the matched filter output is not expected.

The function $rect\left[\frac{1/f - 1/f_o}{B/f_o f_{end}}\right]^2$ has amplitude one and width defined as follows

$$-\frac{B}{2f_o f_{end}} + \frac{1}{f_o} \le \frac{1}{f} \le \frac{B}{2f_o f_{end}} + \frac{1}{f_o}$$

$$\frac{1}{\frac{1}{f_o} + \frac{B}{2f_o f_{end}}} \le f \le \frac{1}{\frac{1}{f_o} - \frac{B}{2f_o f_{end}}} \quad (A.52)$$

$$\frac{f_o}{1 + \frac{B}{2f_{end}}} \le f \le \frac{f_o}{1 - \frac{B}{2f_{end}}}.$$

Applying the limits of the integral in Equation (A.51) yields

$$y(t) = \frac{A^2}{\kappa} \int_{\frac{f_o}{1 + B/2f_{end}}}^{\frac{f_o}{1 - B/2f_{end}}} \frac{1}{f^2} e^{j2\pi f\left\{t - \frac{1}{\alpha}\left[\tau_o - \frac{(1-\alpha)}{\kappa f_o}\right]\right\}} df. \quad (A.53)$$

148

From Equation (A.53) we want to determine:

    a) The time instant when the peak in the matched filter output occurs;

    b) The width of the main lobe assuming that it has a form of *sinc (x)*.

Following [17], it is not necessary to evaluate explicitly Equation (A.53) to answer (a) and (b).

For (a), considering that the maximum in Equation (A.53) occurs when the exponential goes to unity (which can be thought of as the stationary phase argument), it may be written as

$$t_p = \frac{\tau_o}{\alpha} - \frac{(1-\alpha)}{\alpha}\frac{1}{\kappa f_o}. \tag{A.54}$$

Note that (A.54) is constant depending only on the relative radial speed between source and target (factor α).

Assuming that $1/f^2$ is slowly varying, for (b) the zeros in the *sinc (x)* function will be, in an approximation, considered occurring at an integral number of cycles, leading to

$$e^{j2\pi f\left\{t-\frac{1}{\alpha}\left[\tau_o-\frac{(1-\alpha)}{\kappa f_o}\right]\right\}} \tag{A.55}$$

$$\overbrace{\phantom{j2\pi f\left\{t-\frac{1}{\alpha}\left[\tau_o-\frac{(1-\alpha)}{\kappa f_o}\right]\right\}}}^{\theta(t)}$$

$$f\theta(t) = n,$$

where $n = \pm 1, 2, 3\ldots$

The limits of the integral in Equation (A.53) (to replace *f*) are

$$\frac{f_o}{1-B/2f_{end}} - \frac{f_o}{1+B/2f_{end}} = \frac{B\left(f_o/f_{end}\right)}{1-\left(B/2f_{end}\right)^2}. \tag{A.56}$$

Equation (A.56) may be approximated as

$$\frac{B}{1-\left(B/2f_{end}\right)^2}. \tag{A.57}$$

Substituting (A.57) into Equation (A.55) yields

$$\frac{B}{1-\left(B/2f_{end}\right)^2}\left\{t-\frac{1}{\alpha}\left[\tau_o-\frac{(1-\alpha)}{\kappa f_o}\right]\right\} = \pm n. \tag{A.58}$$

149

For $n = 1$ and rearranging the terms in Equation (A.58), we can write

$$t = \frac{1}{\alpha}\left[\tau_o - \frac{(1-\alpha)}{\kappa f_o}\right] + \frac{1}{B}\left[1 - \frac{1}{4}\left(\frac{B}{f_{end}}\right)^2\right].$$

(A.59)

The first term in Equation (A.59) represents the center of the main lobe in the matched filter output and the second represents the half-width. Since $B/f_{end} < 1$ always, the width of the main lobe in the matched filter output is slightly different from $1/B$ and independent of $(4v_r/c)TB$. Thus, the widening and, consequently, the reduction in amplitude in the matched filter output will not be as severe as in the LFM case (see Chapter III, Figure 10).

From Chapter III, Figure 10, it can be seen that with the use of an HFM pulse the filter is "always" matched to the target speeds, as evidenced by the small decrease in amplitude as Doppler errors increase, avoiding the use of a "bank" of filters. From Chapter III, Figure 9, for an LFM pulse there is a large decrease in amplitude as Doppler errors increase. In both cases there is a temporal offset in the matched filter output's peak due to the relative motion between source and target.

In cases where the relative radial speed (or Doppler shift) is known, with the use of HFM pulses, the time of arrival may be predicted using Equation (A.54) as in the following

$$\tau_o \approx \frac{(1-\alpha)}{\alpha}\frac{1}{\kappa f_o} + t_p,$$

(A.60)

where $\alpha \approx 1 - 2v_r/c$, and t_p is the matched filter output peak time. The temporal offset in the matched filter output is

$$t_d = \tau_o - t_p \approx \frac{(1-\alpha)}{\alpha}\frac{1}{\kappa f_o}.$$

(A.61)

Therefore, when the Doppler shift is known, Equation (A.61) permits a direct compensation for the time offset in the matched filter. Unfortunately there is no closed form expression for LFM pulses. Continuing this discussion, let us analyze a simplified argument regarding the widening in the matched filter output due to Doppler effect.

150

C.   DOPPLER-INVARIANT WAVEFORMS

Some authors, as in [21], [59], [60], and [61], make the argument (directly or indirectly) that if the instantaneous frequency of the transmitted signal is merely a time delayed version of the instantaneous frequency of the Doppler transformed received signal, the widening and the amplitude reduction in the matched filter output will not be present, and they label a waveform with such characteristics a "Doppler–invariant" waveform. Therefore, for a "Doppler-invariant" waveform the following equation shall be satisfied

$$f_i(t) = f_{i\,rec}(t - t_d),$$
(A.62)

where t_d is a constant, f_i is the instantaneous frequency of the transmitted signal, and $f_{i\,rec}$ is the instantaneous frequency of the Doppler transformed received signal. The basis of the preceding argument is that if Equation (A.62) is satisfied, the quadratic term in the matched filter output will not be present. Thus, it does not lead to the widening effects as previously demonstrated.

Let us start with the LFM pulse. From Equations (A.10) and (3.19), the Doppler transformed received signal is

$$x'(t) = a(\alpha t)\cos\left[2\pi f_c \alpha t + D_p(\alpha t)^2 - \tau_o\right],$$
(A.63)

for which the instantaneous frequency is

$$f_{i\,rec}(t) = \frac{1}{2\pi}\frac{d}{dt}\left[2\pi f_c \alpha t + D_p(\alpha t)^2 - \tau_o\right]$$
(A.64)

$$= f_c \alpha + \frac{\alpha^2 D_p}{\pi}t.$$

According to Equation (3.20), the instantaneous frequency of the transmitted signal is

$$f_i(t) = f_c + \frac{1}{\pi}D_p t .$$
(A.65)

Substituting Equations (A.64) and (A.65) into Equation (A.62), we obtain

$$t_d = \frac{\pi f_c}{\alpha^2 D_p}(\alpha - 1) + \left(1 - \frac{1}{\alpha^2}\right)t .$$
(A.66)

151

Because t_d is a function of time, the LFM pulse does not satisfy Equation (A.62). Thus, the widening effect in the matched filter output may be expected. Note that there is no closed form expression to calculate the time offset in the matched filter output's peak for an LFM signal.

Moving to the HFM pulse, from Equations (A.10) and (3.22), the Doppler transformed received signal is

$$x(t) = a(\alpha t)\cos\left[\frac{2\pi}{\kappa}\ln(1+\kappa f_o \alpha t) - \tau_o\right],$$

(A.67)

for which the instantaneous frequency is

$$f_{i\,rec}(t) = \frac{1}{2\pi}\frac{d}{dt}\left[\frac{2\pi}{\kappa}\ln(1+\kappa f_o \alpha t) - \tau_o\right]$$

(A.68)

$$= \frac{f_o \alpha}{1+\kappa f_o \alpha t}.$$

According to Equation (3.23) the instantaneous frequency of the transmitted signal is

$$f_i(t) = \frac{f_o}{1+\kappa f_o t}.$$

(A.69)

Substituting Equations (A.68) and (A.69) into Equation (A.62) yields

$$t_d = \frac{(1-\alpha)}{\alpha}\frac{1}{\kappa f_o}.$$

(A.70)

In Equation (A.70) t_d is constant satisfying the criteria for a "Doppler-invariant" waveform. Therefore, the widening effect in the matched filter output is not expected. It is worth noting that Equation (A.70) agrees with Equation (A.61).

APPENDIX B. OBSERVABILITY OF THE DYNAMIC MODEL

In this appendix we address the issue of observability of the overall system. In particular we want to make sure that the dynamic system defined in Equation (2.17) with the observations, Equation (2.25), has suffient information so that both position and current can be estimated.

Although the system is clearly nonlinear, it can be framed as a linear time invariant system with nonlinear memoryless observations. As a consequence we can use the standard observability test using the observability matrix.

Basic Fact:

It is well known that given the state space representation of a dynamic system

$$\left| \begin{matrix} \dot{\mathbf{x}} = \mathbf{A}\mathbf{x} + \mathbf{B}\mathbf{u} \\ \mathbf{y} = \mathbf{C}\mathbf{x} \end{matrix} \right. \quad \text{where } \mathbf{x} \in \mathbb{R}^{N \times 1}, \tag{B.1}$$

the system is "observable", i.e., the state $\mathbf{x}(t)$ can be estimated from $\mathbf{u}(t)$ and $\mathbf{y}(t)$, provided that the following matrix (observability matrix)

$$\Xi = \begin{bmatrix} \mathbf{C} \\ \mathbf{CA} \\ \mathbf{CA}^2 \\ \vdots \\ \mathbf{CA}^{N-1} \end{bmatrix} \text{ is full rank.} \tag{B.2}$$

In our case we have the following:

- $\mathbf{x}$ represents the position of the UUV, where $\mathbf{x} \in \mathbb{R}^{2 \times 1}$;
- $\mathbf{c}$ represents the velocity of the sea current, where $\mathbf{c} \in \mathbb{R}^{2 \times 1}$.

Then we can write

$$\begin{bmatrix} \dot{\mathbf{x}} \\ \dot{\mathbf{c}} \end{bmatrix} = \begin{bmatrix} \mathbf{0} & \mathbf{I} \\ \mathbf{0} & \mathbf{0} \end{bmatrix} \begin{bmatrix} \mathbf{x} \\ \mathbf{c} \end{bmatrix} + \mathbf{\nu}. \tag{B.3}$$

a) UUV and three reference points:

Suppose we have three reference points $\mathbf{P_A}$, $\mathbf{P_B}$, and $\mathbf{P_C}$, as depicted in Figure 80, we may write

$$\mathbf{r_A} = |\mathbf{x} - \mathbf{P_A}|,$$
$$\mathbf{r_B} = |\mathbf{x} - \mathbf{P_B}|, \tag{B.4}$$
$$\mathbf{r_C} = |\mathbf{x} - \mathbf{P_C}|.$$

Then notice that

$$r_A^2 - r_B^2 = |\mathbf{x} - \mathbf{P_A}|^2 - |\mathbf{x} - \mathbf{P_B}|^2, \tag{B.5}$$

as $|\mathbf{a}|^2 - |\mathbf{b}|^2 = (\mathbf{a} + \mathbf{b})^T (\mathbf{a} - \mathbf{b})$, Equation (B.5) becomes

$$r_A^2 - r_B^2 = (2\mathbf{x} - \mathbf{P_A} - \mathbf{P_B})^T (\mathbf{P_B} - \mathbf{P_A}). \tag{B.6}$$

Similarly

$$r_A^2 - r_C^2 = (2\mathbf{x} - \mathbf{P_A} - \mathbf{P_C})^T (\mathbf{P_C} - \mathbf{P_A}). \tag{B.7}$$

We can write (B.6) as

$$\frac{1}{2}(r_A^2 - r_B^2) = (\mathbf{P_B} - \mathbf{P_A})^T \mathbf{x} - \frac{1}{2}(\mathbf{P_A} + \mathbf{P_B})^T (\mathbf{P_B} - \mathbf{P_A}). \tag{B.8}$$

Rearranging Equation (B.8) we obtain

$$\mathbf{y_{AB}} = \frac{1}{2}(r_A^2 - r_B^2) + \frac{1}{2}\left(|\mathbf{P_B}|^2 - |\mathbf{P_A}|^2\right)^T = (\mathbf{P_B} - \mathbf{P_A})^T \mathbf{x}, \tag{B.9}$$

similarly

$$\mathbf{y_{AC}} = \frac{1}{2}(r_A^2 - r_C^2) + \frac{1}{2}\left(|\mathbf{P_C}|^2 - |\mathbf{P_A}|^2\right)^T = (\mathbf{P_C} - \mathbf{P_A})^T \mathbf{x}. \tag{B.10}$$

Then the overall state space representation becomes

$$\begin{bmatrix} \dot{\mathbf{x}} \\ \dot{\mathbf{c}} \end{bmatrix} = \begin{bmatrix} \mathbf{0} & \mathbf{I} \\ \mathbf{0} & \mathbf{0} \end{bmatrix} \begin{bmatrix} \mathbf{x} \\ \mathbf{c} \end{bmatrix} + \mathbf{v}$$
$$\begin{bmatrix} \mathbf{y_{AB}} \\ \mathbf{y_{AC}} \end{bmatrix} = \begin{bmatrix} (\mathbf{P_B} - \mathbf{P_A})^T & \mathbf{0} \\ (\mathbf{P_C} - \mathbf{P_A})^T & \mathbf{0} \end{bmatrix} \begin{bmatrix} \mathbf{x} \\ \mathbf{c} \end{bmatrix}. \tag{B.11}$$

To construct the observability matrix, the matrix $\mathbf{A}$ in Equation (B.2) may be written as

$$\mathbf{A} = \begin{bmatrix} \mathbf{0} & \mathbf{I} \\ \mathbf{0} & \mathbf{0} \end{bmatrix} \tag{B.12}$$

and the matrix $\mathbf{C}$ as

$$\mathbf{C} = \begin{bmatrix} (\mathbf{P_B} - \mathbf{P_A})^T & \mathbf{0} \\ (\mathbf{P_C} - \mathbf{P_A})^T & \mathbf{0} \end{bmatrix}. \tag{B.13}$$

Using Equations (B.2), (B.12), and (B.13) the observability matrix may be written as

$$\Xi = \begin{bmatrix} \mathbf{C} \\ \mathbf{CA} \end{bmatrix} = \begin{bmatrix} \left(\mathbf{P_B} - \mathbf{P_A}\right)^T & \mathbf{0} \\ \left(\mathbf{P_C} - \mathbf{P_A}\right)^T & \mathbf{0} \\ \mathbf{0} & \left(\mathbf{P_B} - \mathbf{P_A}\right)^T \\ \mathbf{0} & \left(\mathbf{P_C} - \mathbf{P_A}\right)^T \end{bmatrix}. \tag{B.14}$$

As long $\mathbf{P_B} - \mathbf{P_A}$ and $\mathbf{P_C} - \mathbf{P_A}$ are linearly independent, i.e., $\det\left(\Xi\right) \neq 0$, the system is observable.
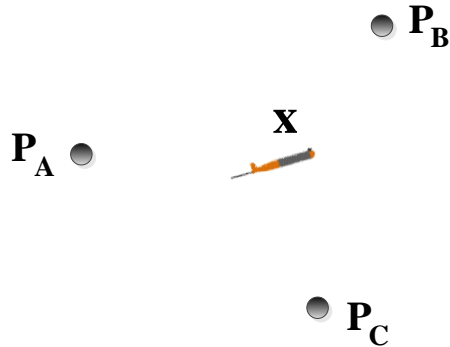

Figure 80.   UUV and Three Reference Points

b) UUV and two reference points:

As observability is independent on the reference frame, let us consider a scenario where the origin of our coordinate system is the reference point $\mathbf{P_A}$ and the line between $\mathbf{P_A}$ and the reference point $\mathbf{P_B}$ represents the x axis as depicted in Figure 81.

155
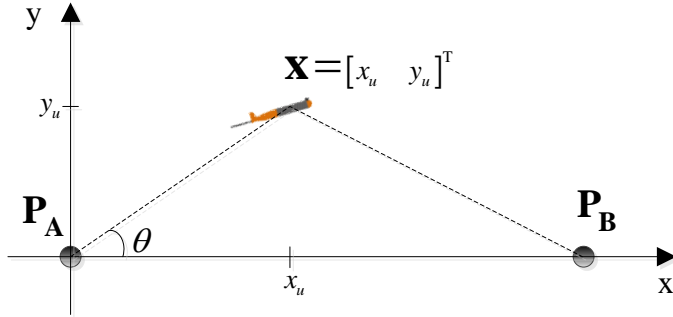
Figure 81.   UUV and Two Reference Points

In this case we can write

$$P_A = \begin{bmatrix} 0 & 0 \end{bmatrix}^T$$
$$P_B = \begin{bmatrix} x_B & 0 \end{bmatrix}^T.$$

(B.15)

From Figure 82 we can write

$$r_A^2 = x_u^2 + y_u^2,$$

(B.16)

and

$$r_B^2 = (x_u - x_B)^2 + y_u^2$$
$$= x_u^2 - 2x_u x_B + x_B^2 + y_u^2.$$

(B.17)

From (B.16) and (B.17)

$$r_A^2 - r_B^2 + x_B^2 = 2x_u x_B .$$

(B.18)

From Figure 81 we can write

$$\cos\theta = \frac{x_u}{r_A},$$

(B.19)

substituting (B.18) into (B.19) we may write

$$\cos\theta = \frac{r_A^2 - r_B^2 + x_B^2}{2r_A x_B} \Rightarrow \theta = \mathrm{acos}\left(\frac{r_A^2 - r_B^2 + x_B^2}{2r_A x_B} \right).$$

(B.20)

From Figure 81 we may write

$$y_u = \mathrm{tg}(\theta) x_u \Rightarrow 0 = \mathrm{tg}(\theta) x_u - y_u .$$

(B.21)

From Equations (B.18), (B.20), and (B.21) the two observations may be written as

$$\overbrace{\frac{r_A^2 - r_B^2 + x_B^2}{2x_B}}^{\delta_{AB}} = x_u$$

(B.22)

$$0 \qquad\qquad = \mathrm{tg}(\theta) x_u - y_u.$$

156

Then the overall state space representation becomes

$$
\begin{bmatrix} \dot{\mathbf{x}} \\ \dot{\mathbf{c}} \end{bmatrix} = \begin{bmatrix} \mathbf{0} & \mathbf{I} \\ \mathbf{0} & \mathbf{0} \end{bmatrix} \begin{bmatrix} \mathbf{x} \\ \mathbf{c} \end{bmatrix} + \mathbf{v}
$$

$$
\begin{bmatrix} \delta_{AB} \\ 0 \end{bmatrix} = \begin{bmatrix} 1 & 0 & 0 & 0 \\ \mathrm{tg}\theta & -1 & 0 & 0 \end{bmatrix} \begin{bmatrix} x_u \\ y_u \\ c_x \\ c_y \end{bmatrix}.
$$

(B.23)

From (B.2) and (B.23) the observability matrix may be written as

$$
\Xi = \begin{bmatrix} \mathbf{C} \\ \mathbf{CA} \end{bmatrix} = \begin{bmatrix} 1 & 0 & 0 & 0 \\ \mathrm{tg}\theta & -1 & 0 & 0 \\ 0 & 0 & 1 & 0 \\ 0 & 0 & \mathrm{tg}\theta & -1 \end{bmatrix}
$$

(B.24)

As $\det(\Xi) \neq 0$, the system is observable.

THIS PAGE INTENTIONALLY LEFT BLANK

LIST OF REFERENCES

[1]   R. P. Vio, R. Cristi, and K. B. Smith, "Near real-time improved UUV positioning through channel estimation-the unscented Kalman filter approach," in *OCEANS MTS/IEEE*, Monterey, CA, 2016. Available: http://ieeexplore.ieee.org/document/7761087/

[2]   A. P. Miguens, *Navegação: A Ciência e a Arte [Navigation: The Science and the Art]*. Rio de Janeiro: Marinha do Brasil, 2002.

[3]   W. Nelson, "Use of circular error probability in target detection," The Mitre Corp. for the United States Air Force, Bedford, MA, Project No. 4110, May 1998.

[4]   A. Bahr, J. J. Leonard, and M. F. Fallon, "Cooperative localization for autonomous underwater vehicles," *Int. J. of Robotics Res.*, vol. 28, no. 6, pp. 714–728, May 2009.

[5]   P. H. Milne, *Underwater Acoustic Positioning Systems*. Houston, TX: Gulf Publishing Company, 1983.

[6]   J. Vaganay, J. J. Leonard, J. A. Curcio, and J. S. Willcox, "Experimental validation of the moving long base-line navigation concept," in *Autonomous Underwater Vehicles*, *IEEE-OES*, Sebasco, ME, 2004, pp. 59–65.

[7]   A. Alcocer, P. Oliveira, and A. Pascoal, "Underwater acoustic positioning system based on buoys with GPS," in *Eighth European Conference on Underwater Acoustics*, Carvoeiro, PT, 2006.

[8]   M. Corless, *Introduction to Dynamic Systems*. Lafayette, IN: Purdue University, School of Aeronautics & Astronautics, 2011.

[9]   A. Gelb, *Applied Optimal Estimation*. Cambridge, MA: The M.I.T. Press, 1974.

[10]   P. M. Woodward, *Probability and Information Theory, with Applications to Radar*. Oxford, UK: Pergamon Press Ltd., 1964.

[11]   L. J. Ziomek, "Signals and Noise," class notes for EO3402, Dept. Elec. and Comp. Engineering, Naval Postgraduate School, Monterey, CA, fall 2014.

[12]   H. Knapp and G. C. Carter, "The generalized correlation method for estimation of time delay," *IEEE Trans. Acoust., Speech, Signal Process.*, vol. 24 , no. 4, pp. 320–327, Aug. 1976.

[13]   P. Z. Peebler, Jr., *Probability, Random Variables and Random Signals Principles*. New York, NY: MacGraw-Hill, 2001.

[14]   M. A. Richards, *Fundamentals of Radar Signal Processing*. New York, NY: MacGraw-Hill, 2014.

[15]   N. Levanon and E. Mozeson, *Radar Signals*. Hoboken, NJ: John Wiley & Sons, Inc., 2004.

[16]   A. W. Rihaczek, *Principles of High Resolution Radar*. Boston, MA: Artech House Inc., 1996.

[17]   J. Minkoff, *Signal Processing Fundamentals and Applications for Communications and Sensing Systems*. Boston, MA: Artech House Inc., 2002.

[18]   J. Rice and D. Green, "Underwater acoustic communications and networks for the U.S. Navy's seaweb program," in *The Second International Conference on Sensor Technologies and Applications*, Cap Estrel, FR, 2008, pp. 715–722.

[19]   B. R. Mahafza, *Radar Systems Analysis and Design using Matlab*. Boca Raton, FL: CRC Press, 2013.

[20]   L. J. Ziomek, *Fundamentals of Acoustic Field Theory and Space-Time Signal Processing*. Boca Raton, FL: CRC Press, 1995.

[21]   J. J. Kroszczynsky, "Pulse compression by means of linear-period modulation," *Proc. IEEE*, vol. 57, no. 7, pp. 1260–1266, July 1969.

[22]   M. J. Hahn, "Undersea navigation via distributed acoustic communications network," M.S. thesis, Dept. Elec. and Comp. Engineering, Naval Postgraduate School, Monterey, CA, 2005.

[23]   D. Green, Teledyne-Benthos chief scientist, private phone conference, Apr. 2015.

[24]   M. Porter. (2011, Jan.). The BELLHOP manual and user's guide: preliminary draft. Heat, Light, and Sound Research Inc. La Jolla, CA. [Online]. Available: http://oalib.hlsresearch.com/Rays/HLS-2010-1.pdf

[25]   P. C. Etter, *Underwater Acoustic Modeling and Simulation*. Boca Raton, FL: CRC Press, 2013.

[26]   F. B. Jensen, W. A. Kuperman, M. B. Porter, and H. Schmidt, *Computational Ocean Acoustics*. New York, NY: Springer, 2011.

[27]   J. B. Keller, "Rays, waves and asymptotics," *Bull. Amer. Math. Soc.*, vol. 84, no. 5, pp. 727–750, Sept. 1978.

[28]   L. E. Kinsler, A. R. Frey, A. B. Coppens, and J. V. Sanders, *Fundamentals of Acoustics*. New York, NY: John Wiley & Sons, Inc., 2000.

[29]   N. Bleistein, *Mathematical Methods for Wave Phenomena*. Orlando, FL: Academic Press, Inc., 1984.

[30]   K. B. Smith, "Sound Propagation in the Ocean," class notes for PH4455, Dept. Physics, Naval Postgraduate School, Monterey, CA, spring 2014.

[31]   A. D. Pierce, *Acoustics, An Introduction to Its Physical Principles and Applications*. New York, NY: McGraw-Hill, 1981.

[32]   M. B. Porter and Y.-C. Liu, "Finite-element ray tracing," in *Theoretical and Computational Acoustics*, vol. 2, D. Lee and M. H. Schultz, Eds. River Edge, NJ: World Scientific, 1994, pp. 947–956.

[33]   O. C. Rodrigues. (2011, Oct.). The TRACEO ray tracing program. Algarve University, Algarve, PT. [Online]. Available: http://www.siplab.fct.ualg.pt/models/traceo/manual.pdf

[34]   M. Porter and H. Bucker, "Gaussian beam tracing for computing ocean acoustic fields," *J. Acoust. Soc. Am.*, vol. 4, no. 82, pp. 1349–1359, June 1987.

[35]   A. Tolstoy, *Matched Field Processing for Underwater Acoustics*. River Edge, NJ: World Scientific, 1998.

[36]   Z. H. Michalopoulou, "Matched-impulse processing for shallow-water localization and geoacoustic inversion," *J. Acoust. Soc. Am.*, vol. 108, no. 5, pp. 2082–2090, June 2000.

[37]   E. L. Hamilton, "Geoacoustic modeling of the sea floor," *J. Acoust. Soc. Am.*, vol. 68, no. 5, pp. 1313–1340, Aug. 1980.

[38]   Y. Bar-Shalom, X. Rong Li, and T. Kirubarajan, *Estimation with Applications to Tracking and Navigation*. New York, NY: John Wiley & Sons, Inc., 2001.

[39]   R. E. Kalman, "A new approach to linear filtering and prediction problems," *J. Basic Eng.*, vol. 82 no. 1, pp. 35–45, Mar. 1960.

[40]   S. J. Julier, J. K. Uhlmann, and H. F. Durrant-Whyte, "A new approach for filtering nonlinear systems," in *Proceedings of the American Control Conference*, Seattle, WA, 1995, pp. 1628–1632.

[41]   E. A. Wan and R. van der Merwe, "The unscented Kalman filter," in *Kalman Filtering and Neural Networks*, S. Hayken, Ed. New York, NY: John Wiley & Sons, Inc., 2001, pp. 221–280.

[42]   S. J. Julier and J. K. Uhlmann, "Unscented filtering and nonlinear estimation," *Proc. IEEE*, vol. 92, no. 3, pp. 401–422, Mar. 2004.

[43] S. Julier and K. J. Uhlmann, "A general method for approximating nonlinear transformations of probability distributions," University of Oxford, Oxford, UK, Tech. Rept. Robotics Research Group, Nov. 1995.

[44] S. J. Julier and J. K. Uhlmann, "A new extension of the Kalman filter to nonlinear systems," in *The 11th International Symposion on Aerospace/Defense Sensing, Simulation and Controls*, Orlando, FL, 1997, pp. 182–193.

[45] S. Särkkä, *Bayesian Filtering and Smoothing*. New York, NY: Cambridge University Press, 2013.

[46] R. Turner and C. E. Rasmussen, "Model based learning of sigma points in uscented Kalman filtering," in *IEEE International Workshop on Machine Learning for Signal Processing*, Kittilä, FI, 2010, pp. 178–183.

[47] A. Sakai and Y. Kuroda, "Discriminative parameter training of unscented Kalman filter," in *5th IFAC Symposium on Mechatronic Systems*, Cambridge, MA, 2010, pp. 677–682.

[48] L. A. Scardua and J. J. da Cruz, "Automatic tuning of the unscented Kalman filter and the blind tricyclist problem," *IEEE Control Syst. Mag.*, pp. 70–85, June 2016.

[49] C. E. Rasmussen and C. K. I. Williams, *Gaussian Process for Machine Learning*. Cambridge, MA: The MIT Press, 2006.

[50] R. Olfati-Saber and R. M. Murray, "Consensus problems in networks of agents with switching topology and time-delays," *IEEE Trans. Autom. Control*, vol. 49, no. 9, pp. 1520–1533, Sept. 2004.

[51] W. Ren, R. W. Beard, and D. B. Kingston, "Multi-agent Kalman consensus with relative uncertainty," in *American Control Conference*, Portland, OR, 2005, pp. 1865–1870.

[52] R. Bellman, *Introduction to Matrix Analysis*. New York, NY: McGraw-Hill, Inc., 1960.

[53] O. Hegrenaes and O. Hallingstad, "Model-aided INS with sea current estimation for robust underwater navigation," *IEEE J. Ocean. Eng.*, vol. 36, no. 2, pp. 316–337, Apr. 2011.

[54] R. Costanzi, F. Fanelli, A. Ridolfi, and B. Allotta, "Simultaneous navigation state and sea current estimation through augmented state unscented Kalman filter," in *OCEANS MTS/IEEE*, Monterey, CA, 2016.

[55] E. Wolbrecht, J. Osborn, S. Qualls, R. Ross, J. Canning, M. Anderson, and D. Edwards, "Estimating and compensating for water currents: field testing," in *OCEANS MTS/IEEE*, Monterey, CA, 2016.

[56]   N. Bowditch, "Tides and tidal currents," in *The American Practical Navigator*, Bethesda, MD: National Imagery and Mapping Agency, 2002, pp. 129–150.

[57]   M. Born and E. Wolf, *Principle of Optics*. New York, NY: Cambridge University Press, 1999.

[58]   R. K. Raney, "A new and fundamental Fourier transform pair," in *International Geoscience and Remote Sensing Symposium*, Huston, TX, 1992, pp. 106–107.

[59]   A. W. Rihaczek, "Doppler-tolerant signal waveform," *Proc. IEEE*, vol. 54, no. 6, pp. 849–857, June 1966.

[60]   J. Yang and T. K. Sarkar, "Doppler-invariant property of hiperbolic frequency modulated waveforms," *Microw. Opt. Technol. Lett.*, vol. 48, no. 6, pp. 1174–1179, June 2006.

[61]   K. Wang, S. Chen, C. Liu, Y. Liu, and Y. Xu, "Doppler estimation and timing synchronnization of underwater acoustic communication based on hyperbolic frequency modulation signal," in *IEEE 12th International Conference on Networking, Sensing and Control*, Taipei, TW, 2015, pp. 75–80.

THIS PAGE INTENTIONALLY LEFT BLANK

INITIAL DISTRIBUTION LIST

1.   Defense Technical Information Center
        Ft. Belvoir, Virginia

2.   Dudley Knox Library
        Naval Postgraduate School
        Monterey, California